MSc. Geomatics Graduation Thesis

Seabed classification using Sub-bottom profiler

Mohamed Saleh

Acoustic Remote Sensing
Faculity of Aerospace Engineering,
Delft University of Technology
The Netherlands

Graduation Professor:	prof. dr. D.G. Simons
Delft Supervisor:	dr. ir. M.Snellen
Innomar Supervisor:	dr.ir.J.Wunderlich
Co-reader:	prof. dr. M.Menenti

Abstract

Sub bottom profilers are commonly used as mapping tool for the seafloor and sub-bottom structure in the upper few meters of the seafloor. Their recent enhanced performance in terms of resolution adds the potential to classify the sediment layers as well. In this research, the seabed surface and sub layers classification are investigated using model based techniques.

The remote sediment classification technique of the seabed surface is achieved by matching the back scatter measurements to the predicted backscatter intensity of the model. The model simulates the returned signals of a monostatic sub bottom profiler operating at 100 kHz. The back scattering strength in the angle domain is estimated using the APL-UW backscattering model. The matching procedure was applied on averaged echo envelopes performed by Hilbert transform. The averaging process is essential to reduce the stochastic variability of the acquired data.

The sub layers data was obtained by operating frequencies of (5, 10 and 15 kHz). The layer classification was achieved by estimating the geoacoustic parameters such as reflectivity and impedance contrast. Two techniques were investigated based on a reflectivity model. The first technique is an extension work of D.Simons [11] which aims to estimate the reflection coefficients via the received and transmitted energy ratio. The second technique is an implementation of a similar approach but applies the attenuation on the received frequency components in place of the nominal components. Both models accounted for energy propagation and its corresponding geometrical and sediment attenuation losses.

The classification techniques were carried out to a dataset that was acquired in the Baltic Sea near Rostock in 2004. The acquired dataset is characterized by various bottom types such as mud, sand and coarse sediments. The general description of the acquired areas was used as a reference for the final results.

Due to the lack of core samples, the classification was evaluated by comparing the results of the backscatter to the energy model. The results were consistent with the general description of the dataset. However, the matching process of the backscatter model is a cumbersome and very sensible to the envelope averaging technique. Averaging the reflected signals from the soft sediments has to ensure to preserve the surficial and volume back scatter information. On the other hand, at rough surfaces, the late arrivals are likely to be irregular reflections or noise that has to be averaged to avoid ambiguous results.

The initial results of sub layers reflection models were consistent with the data description. However, due to the high resolution of the sub bottom profile, the computation procedure can easily fail by missing sub layers. In order to reduce the probability of missing layers, an overlapping window concept was implemented, where the reflection coefficients are estimated at shorter intervals. The methods investigated here leaves room for further optimization through model adjustment such as signal interference, backscatters and error propagation.

Acknowledgement

I wish to acknowledge and thank all the individuals who contributed to my MSc thesis work. Without their support, this document would not have been written.

First of all I would like to thank and express my sincere appreciation to my supervisors, Dr.Mirjam Snellen and Dr.Jens Wunderlich for their continuous support and genuine interest during my graduate studies. They were always there helping, sharing responsibilities and opportunities with me.

Beside my advisors, I would like to thank Prof.Dick Simons for giving me the opportunity to start this project in first place, and his valuable comments in the final stages, making this thesis better readable.

My sincere thanks go to Prof.Volker Boeder from HCU Haven City University of Hamburg, for offering me the Hydrographic summer campaign and inspiring me for this work. I also thank him for his effort and arrangements in order to start this project.

I owe my deepest gratitude to Dimitiros Eleftherakis for his guidance, discussions, proof readings, and his continuous support.

Finally I would like to thank every person helped and encouraged me to continue and complete this thesis. Special thanks go to my family and friends for their support, encouragement and patience.

Mohamed Saleh
Delft, December 2010

Table of Contents

List of figures

List of tables

List of symbols

D (θ)	Directivity index
k	Wave number
a	Transducer radius
c	Sound speed in water
f	Frequency
α_r	Angle of reflection
α_i	Angle of incidence
α_R	Angle of refraction
R	Reflection coefficient
ρ	Density
Z	Impedance
E	Energy
S	Backscattering strength
I	Intensity
μ	Proportionality constant
Mz	Mean grain size
α_w	Water absorption coefficient
α_s	Sediment absorption coefficient
SL	Source level
λ	Wavelength
β	Transducer opening angle
$\sigma_r(\theta)$	Roughness dimensionless backscattering cross section
σ_{lr}	Large scale roughness approximation
σ_v	Sediment volume scattering cross section
$\sigma_{cr}(\theta)$	Composite roughness
$\sigma_{kr}(\theta)$	Kirchoff approximation
r	Slant range
H	Water depth
t	Two way travel time
A	Area
SNR	Signal to noise ratio
E_{TX}	Transmitted energy
E_{RX}	Received energy

d_t	Sample window
F	Fourier function
W	Spectrum component
D_n	Sublayer depth
B	Dimensional constant velocity
P_a	Amplitude pressure
r_e	External radius active area footprint
r_i	Internal radius active radius footprint
σ_b	Total backscatter cross section
T	Pulse length
w_2	Surface roughness power spectrum
W_2	Isotropic roughness
E/S	Error to signal ratio
j_m	Alignment index
T_{ij}	Transmission coefficient
C	Calibration scale factor
d_l	Layer thickness
$N_{specorr}$	Geometrical loss
d	Mean grain diameter
d_0	Reference grain size diameter
$\triangle r$	Range resolution

Chapter 1

Introduction

1.1 Motivation

The increased human marine activities in the oceanic environment, such as building offshore wind farms, dredging operations, oil and gas exploration and the studies of marine geology, morphology and oceanography have led to an imperative demand for accurate seafloor maps. These applications require knowledge of the seafloor topography and detailed information about the seafloor composition, both at the sediment surface and in deeper layers. The conventional approach of obtaining information about the seafloor composition is to take physical sediment samples. This procedure is extremely expensive and time consuming. A much more attractive technique, which provides high spatial coverage at limited costs within short time, is acoustic remote sensing. Remote sensing is defined as the *'measurement of a property or a phenomenon by instrumentation that is situated at a distance and not in direct physical contact with the object of study'* [29]

Acoustic remote sensing techniques are still being developed and refined, trying to balance between robustness and accuracy. One of the most promising techniques for acoustic classification of sediments is a physics-based model. This approach makes use of a model to predict the received signal or part of it. The unknown sediment parameters are input into this model. The received signal is then estimated by minimizing the mismatch between measured and modeled signals. This method has been successfully used with single beam and multibeam echo sounders [8, 9].

The emphasis of this project is to obtain information about the sub layer sediment composition by employing a physics based approach. This project was cooperation between the German Innomar Sub-Bottom Profiler Manufacture Company, which provided the data sets and the acoustic remote sensing group of TUDelft.

`

1.2 Background

The ease of acoustic wave propagation in water was discovered a long time ago, but real practical realization came into light at the beginning of the 20^{th} century after significant world events such as the sinking of the Titanic and World War I. Since then the area of underwater acoustics has been studied in great detail, which has led to the development of echolocation, and underwater communication. With some degree of simplification, acoustic remote sensing today has the same importance in underwater exploration as the radar and radio waves have in the exploration of space. The use of sound for underwater sensing is commonly termed sonar, which is an acronym for SOund NAvigation and Ranging.

Seafloor mapping is almost entirely performed using acoustic systems. Optical systems are limited by the fact that electromagnetic waves do not propagate underwater further than 10-50 meters due to water absorption [30]. On the contrary, acoustic waves are more practical, as they are based on the mechanical vibration of their propagation medium. Since the bond *'elastic modulus'* between water molecules are stiffer than those of air which in turn makes the water more difficult to compress than gasses, acoustic waves in water have better transmission characteristics than in air. Their propagation speed in water is four to five times higher than in air and even higher in solids (e.g. sediments), the sound undergoes less attenuation resulting to travel longer distances. For example under the same signal conditions *(i.e. equal frequency and power)*, sound propagation in air hardly reaches few kilometers air, while the sound propagation in ocean can exceed up to thousands of kilometers.

Typical frequencies associated with underwater acoustics are between 10 Hz and 10 MHz. The propagation of sound in the ocean at frequencies lower than 10 Hz is usually not possible without penetrating deep into the seabed, whereas frequencies range for underwater applications is rarely higher than 1MHz due to the rapid absorption within the water column.

Most systems used today for seabed mapping make use of a single acoustic frequency [31, 32] because different frequencies interact with the seabed or objects in different ways, which requires more sophisticated sensor to capture the desired information. For example, high frequency sonar can measure accurately the water seabed depths, whereas sub-bottom layers are better observed by lower frequencies. This is due to the decreasing sediment sound absorption with decreasing frequency.

Classical Sub-bottom profilers SBPs are single frequency sonars that aim to explore the first layers of sediments below the seafloor over a thickness commonly reaching several tens of meters. It has been for many years a fundamental tool for oceanography and offshore engineering due to the ability of this system to determine physical properties of the seafloor and to identify geological layers below the seafloor [33]. Sediment structure is directly observed by measuring the elapsed time of the received reflections of the acoustic energy when it encounters boundaries between layers of different properties.

Many studies [8, 11, 12, and 17] have been published concerning classification techniques of seabed surfaces using single beam, multibeam, and side scan sonars, while few paid attention to classify sub-bottom layers using a sub bottom profiler. For the latter, the challenge was to develop algorithms that automatically characterize the layered sediment types as a contribution step towards "what lies where in 3D?"

1.3 Research objectives and methodology

Underwater acoustic system have for many years been a fundamental tool for oceanography and marine geology [32]. Their design and configurations can be set to cover various applications. From the geological perspective, underwater acoustics can explore three distinctive zones; surficial, near-surficial and deep sedimentary layers. Figure (1) shows a seabed cross section that represents the relation between the three zones and their exploration ranges or so called penetration depths.

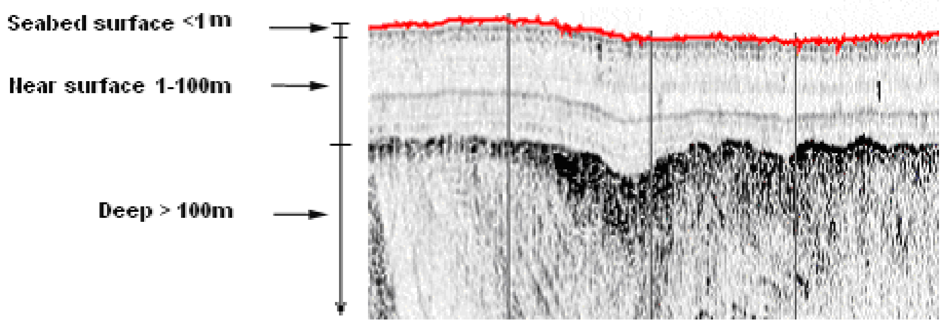

Figure 1: Observation zones

Acquiring information of the illustrated zones requires diversification of the instrumental design to emit an acoustical signal with a specific physical parameter such as output power, signal frequency and length. For example single beam echo sounders (SBES) are designed to acquire surficial data to provide accurate water depth. Typical frequencies range from 10 to 200 kHz.

To allow greater penetration into the substrate, low frequency signal with high energy has to be used. Low frequency systems give great substrate penetration due to low attenuation rate, whereas high frequency is attenuated faster in propagation medium. The transmitted energy depends mainly on the signal amplitude (i.e. power) and signal duration. Since the transmitted power is limited, the transmitted energy can be increased by distributing the power over a longer time (i.e. pulse width). Such signal characteristics (i.e. low frequency, power and pulse duration) are beyond the SBES capabilities and alternative instruments have to be used instead such as marine seismic.

Marine seismic systems explore the deep structure of the seafloor using seismic waves as in land-based geophysics [34] by using large energy. There are a number of different marine seismic systems which operate at various frequencies such as sparkers that operate between 50Hz to 1000 Hz and boomers which operate between 500 Hz to 5 kHz.

Classical SBP works with one low frequency only which is sufficient to map the seabed layers to certain depth. Nowadays most SBP use a second (higher) frequency to add the functionality of SBESs (i.e. accurate water depth and possibly seabed material) such as SES-2000 system which has been used in this project. The system is based on an interesting hybrid concept between sonar (e.g. SBES) and marine seismic systems. The system emits two or more signals with different frequencies depending on the application and environmental conditions. For the simplest case the instrument transmits a high frequency signal 100 kHz to provide accurate water depth and a low frequency signal to provide information about the substrates operating at frequencies between (1-20 kHz). SBPs that operate within low kHz range are useful for high resolution assessment of the top 100 m of sedimentary material below the sea floor. Figure (2) illustrates the operational frequency band of various underwater acoustic instruments with their corresponding penetration depth and vertical resolution (R) [35].

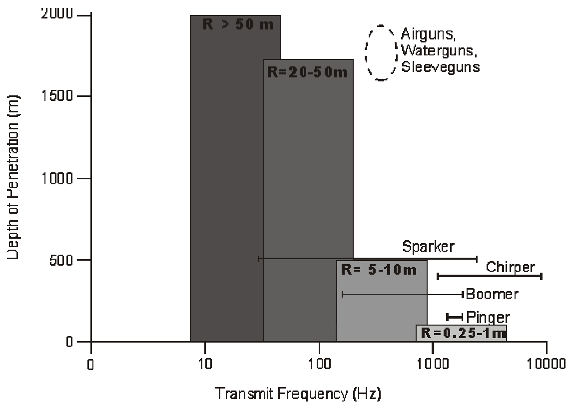

Figure 2: Pingers and Chirpers are considered SBP systems,
Remaining sensors are considered Marine seismic systems

This project is characterized by an interdisciplinary approach. Developing a method for sub layer classification requires combined knowledge from various fields like oceanography, signal processing, physics and remote sensing. It is possible to subdivide the entire work into three major steps. First of all, signal processing and data preparation was applied to the entire dataset in order to reduce the noise and measurement artifacts. Second, the enhanced high frequency dataset was used to infer the sediment characteristics at the water-seabed surface. In the third step, the subsurface composites were inferred from the low frequency signal.

Signal processing: The data used in this project was acquired by 'Innomar' in January 2007 in the Baltic Sea near Rostock. An SES-2000 standard SBP system was used for acquiring the data with filters set to a maximum bandwidth. The filter settings were experimental to ensure that the received signal was almost unchanged which consequently caused high noise level. Therefore a filtering procedure was necessary to remove the presence of noise to increase the level of confidence within the analysis procedure. Other techniques such as alignments and averaging were also necessary to treat the stochastic behavior of the acquired dataset.

Surficial Characterization: For surficial characterization, the high frequency data was used as input for a theoretical (model based) algorithm. This model was initially developed by the TUDelft acoustic remote sensing group for the processing of the SBES signals. The model was modified to simulate the SBP transmitted signal in order to predict echo envelopes that can be compared to the observed ones. The basic working principle of the model is based on producing echo envelopes for a range of seabed types that then can be correlated to the actual measured signal.

Sub-bottom Characterization: The received echo envelopes near the surficial area are a product of complex physical interactions within the stratigraphic layers. These interactions can no longer be predicted by the SBES model. Fortunately, these complex behaviors are dominated by reflections at layering boundaries which simplifies the task of sediment identification. Consequently this task required alternative models to assess the characteristics of the sediment layers, by relating the mean grain sizes of the sediments to the acoustic impedance. This is achieved by precisely determining the reflection coefficient at each sediment layer.

The aim of this project is to investigate the feasibility of the proposed classification methods in order to discern between seabed types at surficial and near surficial areas.

1.4 Outline

The first section of Chapter 2 describes the technical aspects of the used SBP by comparing it to common used SBES systems. The second section gives a short introduction to some of the physical processes that are encountered during underwater acoustic propagation. The last section gives a comprehensive introduction to the field of sediment classification methods. A more detailed acoustic background and modeling aspects are discussed in chapter 3. The discussion is entirely devoted to the acoustics theory and the numerical implementation of the model for predicting the received echoes. Chapter 4 focuses on the signal processing of the high frequency data, the algorithm for matching the acquired data to the prediction of the model and the classification results. Chapter 5 is devoted to the sub layer classification. Two physics based models were implemented to infer and compare the predicted mean grain size of the sub bottom layers. The chapter ends by comparing the results of both methods. Chapter 6 completes the thesis by a number of conclusions and recommendations for future work.

Chapter 2

Classification and sensor aspects

Introduction

The first section of this chapter describes the working principle of the sub bottom profiler. Major differences between SBP and SBES will be illustrated in order to give to the reader insight in the advantages and limitations of the used SBP system. The second section illustrates the basics of seafloor interactions undergone by a transmitted SBP signal. The third section of this chapter is devoted to a comparison between the two known (phenomenological, and physics based) underwater classification approaches.

2.1 Sub-bottom profiler

The function of a sediment profiler is to record echoes from interfaces between sedimentary layers that correspond to differences in acoustic impedance. The movement of the support platform will allow reconstruction of a vertical cross-section of the sedimentary environment obtained as an image of boundaries between layers such as show in figure (1). Good horizontal resolution requires a directivity pattern with a very narrow opening angle. The directivity pattern is the transducer directional sensitivity of transmission and/or receiving as illustrated in figure (3). The directivity pattern of an antenna depends on the transducer geometry, and frequency. For the same transducer geometry, higher frequencies give narrow opening angles and lower frequencies gives wider opening angles.

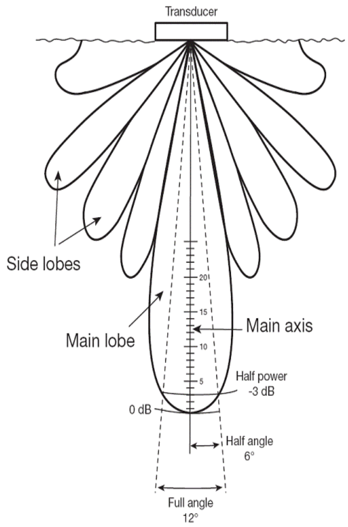

Figure3: Schematic image of transducer beam pattern scaled in dB reproduced from Johannesson and Mitson (1983).

The transducer dimension design is based on the desired beam pattern. The beam pattern is a dimensionless and a relative parameter of the transducer. It is a function of the operational frequency, aperture angle, and size and shape characteristics of the vibrating surface. The mathematical expression '*sinc function*' for the normalized directivity pattern that gives the transducer sensitivity of the plane circular piston transducer is [7]:

$$D(\theta)=\left[\frac{2J(ka\sin\theta)}{ka\sin\theta}\right]^2 \quad (1)$$

Where J is the Bessel function of first order, k the wave number, a is the radius of the transducer, and θ is the aperture angle. The variation of the sensitivity width with look direction is illustrated in figure (4) where y-axis represents the directivity response and x-axis $=ka\sin\theta$.

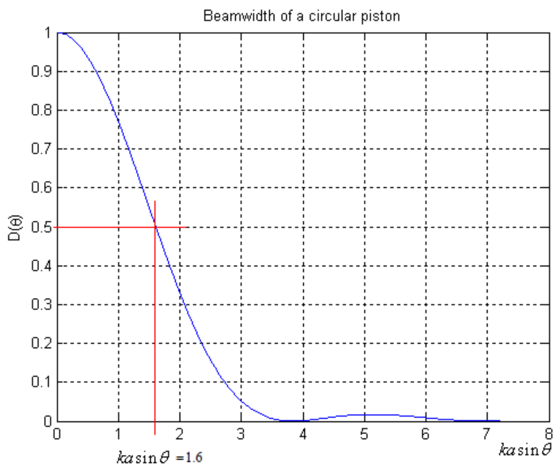

Figure 4: Beam width variation of a circular transducer

The half power beam width D = 0.5 (-3dB) is a well known criteria that is commonly used between manufactures so that transducers can be compared quantitatively. Thus, the relation between the transducer radius and frequency is obtained by [36, 10]:

$$a = \frac{1.6}{k \sin(\theta_{3dB})} \qquad (2)$$

Where

$k = \frac{f}{c}$,

c Propagation speed,

f Transmitted frequency

To compare between the required transducer dimension for a low and a high frequency, consider two linear systems. The first system is required to emit a signal of f = 100 kHz and the second is required to emit a signal of f =5 kHz. Both systems have a half power beam opening angle θ of 3.6º. Such frequencies would require a transducer diameter approximately 2.5m for the first system and 30cm for the second system as shown in figure (5).

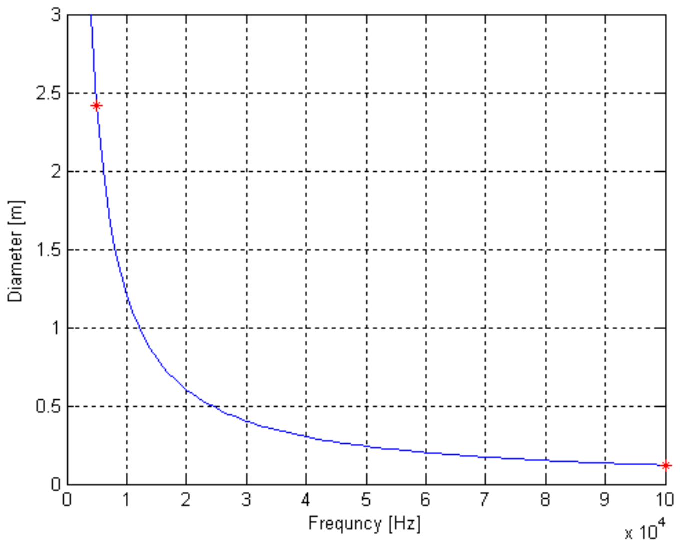

Figure 5: Required radius dimension of linear transducer and the corresponding frequency. Red dots shows transducer diameter for opening angle of f = 100 kHz, f =5 kHz, c =1500m/s.

The previous calculations are based on the linear concept where only a single signal is emitted. With this concept, a large transducer is needed to emit a low frequency with such narrow opening angle which is not practical. To eliminate the need for large transducers, parameter sensors have been developed. This type of sensors are based on the non-linear concept where two or more signals are emitted and synchronized in time

Linear and Non-Linear concept

If two transmitters emit two signals with the same frequency, where the crest of two waves are in step, the linear process of the secondary wave is a result of the superposition of the two signals known as 'spatial interference' which is a function of the distance between the two transmitters. In this case, two types of waves will be produced as a result of 'constructive' and 'destructive' interaction as shown in figure (6). Constructive interaction means combining two or more waves to get a new 'third wave' that has the same wavelength and frequency but higher amplitude 'more intensity'. Destructive interaction means that waves are subtracted and cancelled out. The peak in one wave is cancelled by the troughs in the other.

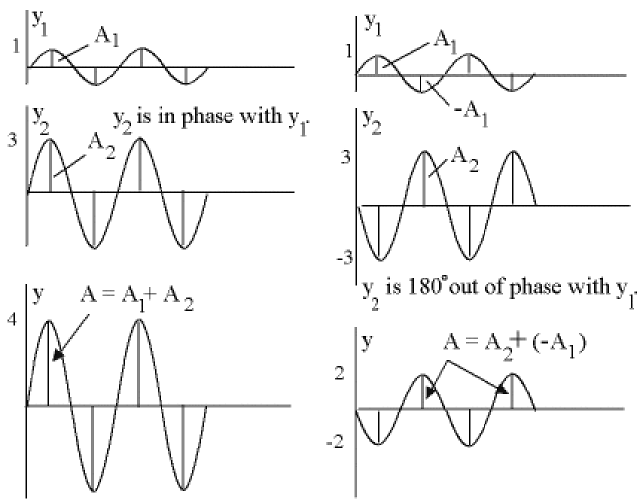

Figure 6: principle of spatial interference

In a more complex case, such as with nonlinear SBP's, the echo sounder transmit two signals of slightly different high frequencies (primary frequencies f1 and f2) at high sound pressure simultaneously. Due to the high pressure, the sound propagation will be non-linear; water sound velocity is a function of water pressure, temperature, salinity, and density. At very high pressures, the density of water changes. Thus, the sound velocity changes non-linearly [41].The higher sound amplitudes will move faster than lower sound amplitudes. As a consequence, a number of secondary frequencies are produced such as harmonics, sums of the primaries, and the desired primary difference F = |f1-f2|. Figure (7) gives a schematic view of the signals and the corresponding spectrum.

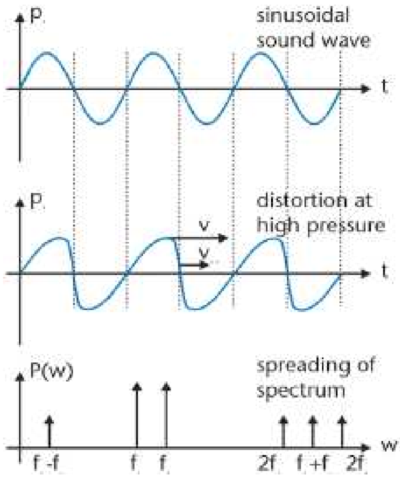

Figure 7: Principle of nonlinear acoustics [25]

Interestingly, the secondary low frequency has now the same narrow directivity as the primary frequencies. Thus, the directivity pattern of the low frequency does not depend on transducers dimension, but depends on the non-linear phenomena occurring in the medium.

The difference between the linear and nonlinear directivity pattern is illustrated in figure (8). The left plot shows the directivity of a linear system computed by the traditional sinc function. The right plot shows the measured directivity obtained using a hydrophone in front of a real parametric transducer. By comparison, the directivity pattern of parametric transducer has no side lobes, which are typical for linear transducer. The reason for this is that the energy of primary waves is transferred to the secondary wave only in high intensity in the nominal direction. While In the other directions it is too low to cause nonlinear effects.

The figure also shows the beam width of the main lobes. By comparison the beam pattern of the parametric transducer (all frequencies) have the same narrow beam width, while for the linear system, the beam width is inversely related to the transmitted frequency.

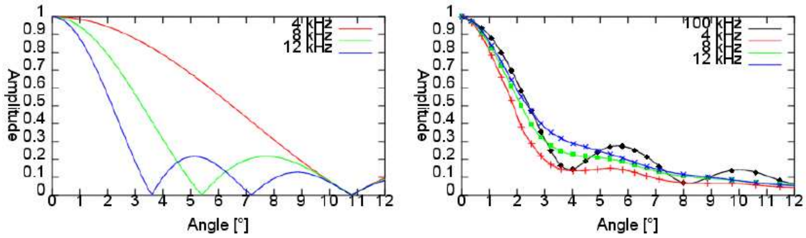

Figure 8: Directivity pattern for linear (left) *computed* and parametric transducer (right) *observed* [25].

Resolution

The main objective from a SBP is to obtain the deepest penetration depth with highest vertical resolution also known as range resolution. Vertical resolution is the ability of sonar system to distinguish between two or more objects on same bearing but at different ranges [2]. In principle, vertical resolution depends mainly on the transmitted pulse duration of the CW. The range resolution can easily be estimated by:

$$\Delta r = \frac{ct}{2} \quad (3)$$

Where:

c = sound velocity,

t = pulse duration

This means that in order to obtain high range resolution (i.e. short Δr) very short pulses are needed. However, in order to obtain deeper penetration, the transmitted signal has to have enough energy to such that the pulse can be detected from the noise. Since the power is limited due to cavitations, the only option is emit a long pulse. For this reasons many sub bottom profilers uses chirp signals to obtain high resolution. A chirp is a frequency modulated signal, where the pulse is emitted with a modulated frequency. The frequency modulation is processed at the receiver to focus the pulse to a much shorter value and hence obtain the desired resolution [36].

However, these signals will have advantages in deep water while in shallow such as this experiment the long sound pulses i.e. high energy will cause more signal to be reflected back off the seafloor leading to multiple reflections and high reverberation without any advantage compared to short CW-pulses. Reverberation is the persistence of sound in an enclosure or partially enclosed space after the source of sound has stopped; the persistence is a result of repeated reflection and/or scattering [40]. Therefore in this experiment the sensor was adapted to emit short 'CW', and the resolution issue is improved by tapering the amplitude (Gaussian shape for instance) to give better spectral properties that lead to less ambiguities in range. More details about the properties of Gaussian shaped signal will be given in chapter (3).

In summary, low frequency can now be transmitted by a sensor with a reasonable dimension. The beam width of the low frequency is the same as the primary frequencies without side lobes that has high horizontal and vertical resolution [5, 6]. The data has a high signal to noise ratio due to the small footprint and low reverberation level.

2.2 Seafloor Interaction

The acoustic wave interaction with the seabed depends partly on the impedance contrast between two layers. Impedance is a medium characteristic equal to the product of the density and propagating sound speed. Large impedance contrast between water and rocky seabed with a considerable smooth surface means that the seabed surface behaves as an almost perfect reflector. On the other hand, at softer sediments, the acoustic impedance mismatch is much less which means that larger energy will be able to penetrate this boundary. Each time the signal encounters a different material, a portion of the energy is reflected and recorded by the system. The percentage of the acoustic energy reflected at each layer surface is a function of the relative densities, sound speeds and angle of incidence at the two layers.

Reflection of seabed surface

Consider the case of a plane acoustic wave incident upon a water-sediment interface. If the water-seabed interface is completely flat the sound can be reflected in a manner similar to a light beam striking a mirror. This phenomenon can be described using the classical optical reflection expression known as Snell's law which is illustrated in figure (9).

Snell's Law describes the relationship between the angles and the velocities of waves in two different mediums (ε_1, ε_2). In the first medium ε_1 the angle of the incoming ray α_i is equal to the reflected ray angle α_r. The law also equates the ratio of material velocities C_1 and C_2 to the ratio of the sines of incident α_i and refracted α_r angles.

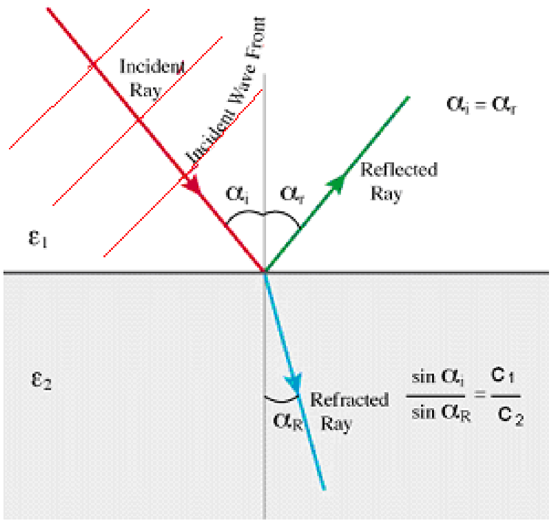

Figure 9: Reflection process

The amplitude of the reflected wave is a function of the reflection coefficient R expressed by equation (4), where (ρ_1, c_1) and (ρ_2, c_2) are the density and sound velocity respectively of the two media. Therefore the reflected amplitude is a function of the sediment type:

$$R(\theta) = \frac{\rho_2 c_2 \sin(\alpha_1) - \rho_1 c_1 \sin(\alpha_2)}{\rho_2 c_2 \sin(\alpha_1) + \rho_1 c_1 \sin(\alpha_2)} \qquad (4)$$

Reflection of a layered medium

As mentioned earlier, the reflection coefficient depends on the impedance contrast between two mediums. For the high frequency signal, a portion of the signal energy will be reflected at the first layer. The remaining energy will be highly absorbed, and the wave transmitted into the layer progressively becomes unable to reach the substratum. On the contrary, the low frequency signal is subjected to lower sediment attenuations and the remaining energy can easily penetrate into deeper layers until it is totally absorbed, or meets other sediment layer with high impedance contrast such as clay-rock interface. The percentage of acoustic energy reflected at each interface surface is a function of the relative density and sound speed of the two layers known by the impedance contrast. An equation for the acoustic reflectivity of an underwater surface is given in Figure (10). This equation is valid only for the simplified case in which the change in material composition from one layer to another occurs in a short vertical length compared to the wavelength of the incident signal. A more rigorous analysis would require that the density gradient from one layer to the other be known. Such analysis is beyond the scope of this thesis.

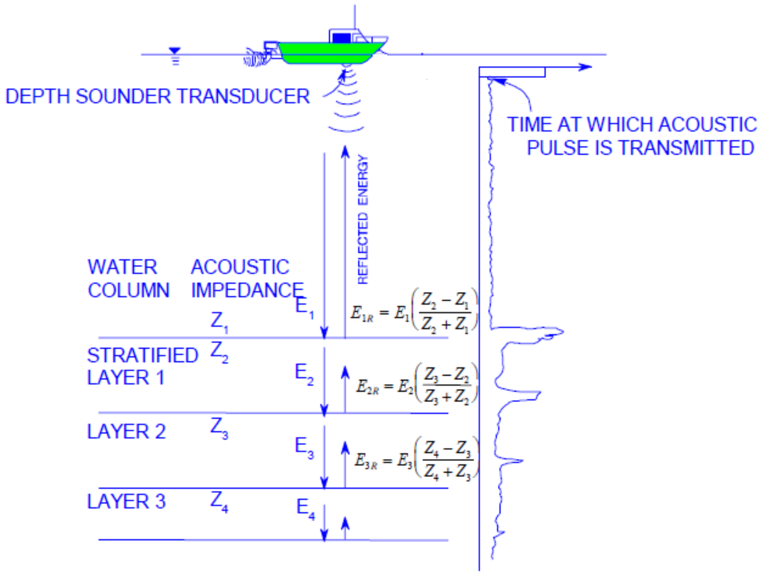

Figure 10: Acoustic impedance changes in different sediment densities; Z is the acoustic impedance where $Z_1 = (\rho_1, c_1), Z_2 = (\rho_2, c_2), Z_3 = (\rho_3, c_3), Z_4 = (\rho_4, c_4)$ [23]

Backscatter

In the reflection section it was mentioned that the returned echoes are reflected from a local plane water-sediment interface that is completely flat. In reality such interface is far from an ideal plane which makes the acoustic process much more complex than described earlier in the reflection section. Figure (11) illustrates the phenomenon of scattering caused by an irregular seabed surface and its influence on the received echo.

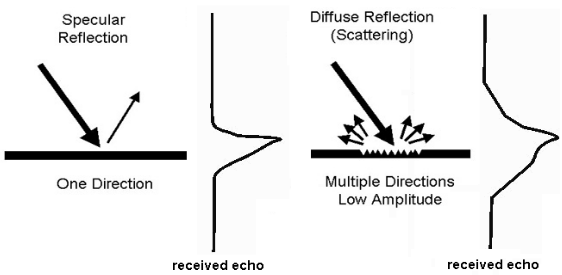

Figure 11: Reflection versus general surface scatter

In order to model such phenomena, the water-sediment interface can be considered as a local plane with microscale roughness. Part of the incident wave will be reflected with no deformation other than amplitude loss in the specular direction (coherent part). The reminder of the energy is scattered in the entire space, including backwards to the source. This process is depicted with more details in figure (12).

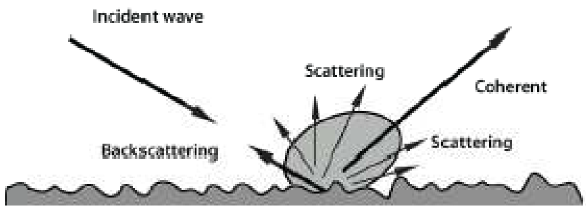

Figure 12: scattering phenomena

The effect of the relief on the incident acoustic wave depends on the frequency, the angle of incidence and the sediment type. Sediment roughness values can have a wide scale of amplitudes ranging between millimeters to few meters and spatial wavelength. It is also possible that several roughness scales exist on the same surface. For example, a sandy seafloor with a centimeter – scale roughness, can be superimposed on its existing topography

The relative importance of specular and scattered components depends on the surface roughness in terms of acoustic wavelength. For short wavelengths a particular seafloor may seem rough, while for longer wavelengths the same seafloor seems smooth.

A measure for scattering is the scattering strength, which is defined as the intensity ratio of sound scattered at a unit area at a distance 1m from this unit to the impinging plane wave intensity. Equation (5) expresses the scattering strength in dB as follows:

$$S = 10\log_{10}\frac{I_s}{I_i} \quad (5)$$

Two types of targets exist; targets with dimensions small enough to be completely ionisfied by the sonar beam and signal (e.g., a fish, or small object) and targets too large to be ionisfied completely at once by the same beam. The first type of targets behave as ‘points’: their strength is an intrinsic strength, independent of the distance to the sonar or its characteristics, whereas for the second type targets (e.g., large fish school, seabed or sea surface) target strengths are no longer a point value, but an ionisfied space (surface or volume) is used. The expression now is the amount of energy scattered by a ‘unit scattering element’. It is therefore expressed in dB re m^2 or dB re m^3. Consequently, the spatial distribution of the scattered energy can now be described using the scattering function that depends on the incident and scattered angle $S(\theta_i, \theta_s)$.

Acoustic scatter is very important because the scattered part of the signal shows very different orders of magnitude that depend on the target characteristics. Exploiting this behavior makes the backscatter field a very attractive phenomenon that can be used in many sonar applications. However, [23] showed that the scatter mechanism is very complicated and not only is limited by surface roughness, but also by the inhomogeneities within the sediment volume, and other mechanisms that can be coupled.

Various models have been developed that range from relative simple to complex. The simplest model is the Lamberts rule expressed in equation (6) which is a function of frequency and sediment type described by the parameter μ and the incidence angle of the transmitted signal.

$$S(\theta_s) = 10log_{10}\mu + 10log_{10}(sin^2\theta_i) \qquad (6)$$

Despite the simplicity of the model, Lambert’s law is a good first approximation and shows an acceptable agreement with the physical observations. For backscattering by soft sediments its approximation is restricted for grazing angles between 5 and 40 degrees. Grazing angles >40 degrees are too low near specular direction. On very rough surface like rocks it may be employed over the entire angular domain. In [23] a number of solutions were proposed to remedy these limitations.

Mackenzie [24], showed that a value of $10\log_{10}\mu = -27dB$ is a good start for all bottom types. Several later studies have determined μ for different sediment types, see e.g. Garlan [3], from which table (1) is obtained. If the incidence acoustic energy is fully scattered into the upper medium without sediment inner transmission, it can be shown that $\mu_{\max} = 1/\pi, 10\log_{10} = -5dB$ as illustrated figure (13).

Table 1: μ value for different sediment types

Sediment type	$\mu(dB)$
Rock	-18
Sand	-31
silt	-37

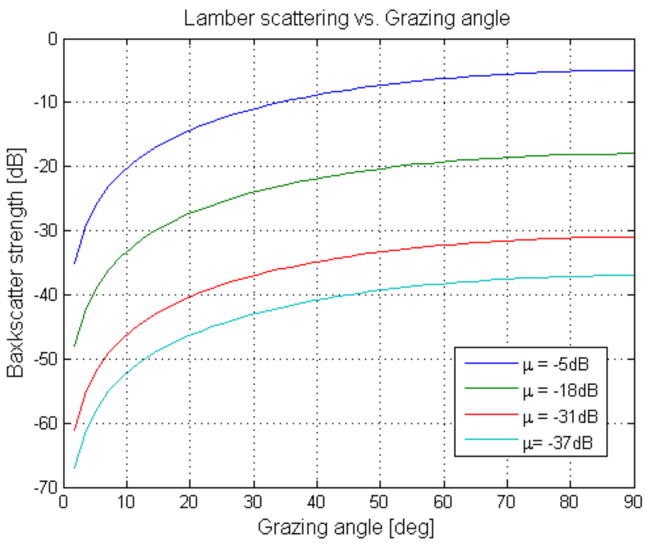

Figure 13: Backscatter of various sediment types following Lambert rule

Since SBPs have a limited beam width, Lambert's law is not capable to capture the process accurately, especially at near specular direction. Therefore a more sophisticated backscatter model is needed.

2.3 Classification methods

Classification methods are numerous but can fall under two general categories: *phenomenological* and *model based* approaches. Phenomenological approaches are based on grouping echo like features together and labeling each group using ground truth. The selection of grouping can be based on the similarity of amplitudes, skewness, energies, etc. In other words, high-quality phenomenological classes are derived from features, of the echo. The *model based* approach models physic processes in order to calculate the received echo and its features. The classification result is based on tuning the geoacoustic parameters that influence the modeled signal in order to achieve the maximum match between the modeled and the real received echoes.

Phenomenological approach

Phenomenological methods are the most used approach. The aim is to extract some properties from the measured seabed echo that will allow the bottom to be classified into relatively homogeneous categories. Classifying the data in this way allows areas with similar seabed properties to be grouped together.

The number of features or signal properties can start from the simple case where only two attributes are available and segmented in the 2d space to large number of features. The large number of features can then be simplified by principal component analysis PCA to summarize the information into a few orthogonal components [37], each explaining a decreasing proportion of the dataset total variance. The number of principal components (PC) to keep for the classification is open to debate, but altogether they must represent the major part of the variance observed in the signal features [38]. A short list of the features that have been extracted from seabed echoes is given in Table 2.

The next step is to link the classified groups to in situ data. Recording the exact location from which the ground-truth data is collected allows it to be linked to the acoustic data from the same geographical location. In this way, the two datasets can be linked, providing the required verification and the in situ classes can be extrapolated to all the regions that fall within the same acoustic class.

Table 2: Classification features list

Signature feature	Author
Square root of the ratio of the total significant energy of the second bottom echo to that of the first bottom echo, averaged over a number of pings	**SBES** Orlowski, 1984
Sum of the energy from the tail of the first bottom echo (E1), used as an index representing the seabed roughness	**SBES** Chivers et al., 1990; Heald and Pace, 1996; Siwabessy et al., 2000
Normalized cumulative function of the echo envelope	**SBES** Lurton and Pouliquen, 1994
Mean, standard deviation, and higher order moments, amplitude quintiles and histogram, power spectral ratio features, grey-level co-occurrence features, fractal dimension	**MBES, SSS** Preston et al. 2004
Seabed backscatter strength shape as function of the incident angle, described by a set of parameters	**MBES, SSS** Hughes-Clarke et al., 1997

The general phenomenological processing procedures can be summarized as follow:

1 – Compensate the echoes for depth effect.

2 - Extract features from the corrected echoes.

3 - PCA (combination of all extracted features).

4 - Clustering the sets of principle components corresponds to number of sediments types.

Physics Based approach

In the physics based approach, use is made of a mathematical model. We seek quantitative estimates of parameters of the model by comparing measured data with modeled data. Knowledge of transmitted pulse shape, duration, and power is needed. The unknown seafloor geo-acoustic parameters are input into this model and estimated by minimizing the mismatch between the measured and modeled acoustic signals. The advantage of this approach is that, in principle no independent measurements ‘ground-truth’ of the actual seabed is required. However, the ground truth can still be very helpful to assess the classification results.

This approach is more complicated than the phenomenological approach since it requires full understanding of the physical process that the signal encounters. In addition some optimization is needed to find those unknown parameters that provide an optimal match between model predictions and measurements.

In this research the physics based approach is used. For the high frequency signals, a physics based model that was implemented for SBES by TUDelft acoustic remote sensing group was modified in order to be used for the SBP sensor. For the low frequency two methods were implemented based on the energy interaction with stratified layers.

During the survey core samples were taken which indicated the general sediment classification within the surveyed area. However the detailed sediment characterization was not available for the author. Therefore it was decided to implement different models and compare additional features in order to strengthen the classification results. Moreover calibration parameters were not available which is essential in the model based approach. To overcome this problem the subset of the dataset were chosen and assumed to be linked with the general description of the surveying area.

The main stages of the model based approach can be described as follows:

1 – Remove noise from measured signals

2 – For each ping, a signal is modeled

3 – Input parameters (signal characteristics, environmental parameters)

4 – Search for the sediment geoacoustic parameters that maximize the match between modeled and observed echo.

Chapter 3

Implementation the high frequency model

Introduction

This chapter introduces the building blocks of the SBES physics based model. The SBES model is a time domain simulation that predicts the received echo envelope as received by the transducer. The SBES model exploits a sophisticated back scatter model that was published by the Applied Physics Laboratory of the University of Washington (APL-UW) [4]. The model accounts for the signal propagation in the water column, the signal geometrical interaction, and the corresponding backscatter process at water-sediment interface. As mentioned earlier in chapter 2, an emitted signal with high frequency has different seabed interaction than a low frequency signal in the aspect of sediment penetration and absorptions. Thus, this simulation is only valid for the high frequency signal [100 kHz]. The remaining low frequencies (5.10, and 15 kHz) will have to be modeled by a different approach in chapter 5.

3.1 SONAR equation

Transducers provide data on: 1) the time delay between transmission and reception of the echo, which corresponds to the water depth, and 2) the echo signal intensity of the returning echo (echo level). To calculate the echo level, consider an acoustic system with transmitting sensitivity $b(\theta)$ and receiving sensitivity $b^{'}(\theta)$. The sensor emits a short pulse with pulse duration (τ) and average source intensity I_s. The pulse propagates through an unbounded medium spherically. At a range R, the pulse strikes the seabed and insonifies an area A of random homogeneous distribution. A part of the signal is backscattered towards the source with backscatter intensity $S_b(\theta)$. The time-dependent intensity measured at the transducer interface is modeled as sum of a sediment interface and volume backscatter by following the work of Jackson et al [5]. The received signal intensity $I_r(\theta)$ is estimated via the sum of elemental areas by the following equation:

$$I_r(\theta) = \frac{I_s}{R^4 e^{4\alpha_w R}} \int_A S_b(\theta) b(\theta) b^{'}(\theta) dA \qquad (7)$$

3.1.1 Sounder considerations

The first parameter I_s in equation (7) is devoted to the source level. Source level is one of the signal characteristics that are controlled by the SBP acoustic system. Configurations of the acoustic pulse characteristics such as frequency, duration, shape, and level influence the information that is carried from the seabed. Practically, their values are tuned to optimize the desired accuracy and resolution within the survey project. The tuning values are a function of the environmental parameters such as water depth, temperature, salinity, seabed type, etc. In this section the signal considerations will be investigated to demonstrate their influence on the model prediction.

Source level

The source level for a non-directional source is defined as the intensity (in dB) of the radiated sound at 1m distance of the source relative to the intensity of a plane wave with $1\mu Pa$ rms pressure. Choosing an appropriate power setting to maximize the capabilities of the sounder and the acoustic classification system requires advance planning and considerations of the surveying area. The signal strength has to be strong enough to prevent the loss due to water depth ranges, and soft substrate attenuations. On the contrary, too high power over shallow and rough substrates returns high reflections that are limited by signal clipping.

To reach the optimal source level, the raw returning signal needs to be monitored so the gain can be set. This can be set using oscilloscope or a raw waveform viewer. Most echo sounders have an Automatic Gain Control (AGC) mode which controls the signal power while transmitting and/or receiving the signal. However, technically it is much easier to apply it in the receiver, while transmitter AGC has some restrictions.

Frequency

The absorption rate of a specific frequency depends strongly on the propagation medium. For sea water, the absorption comes from viscosity of pure water and relaxation process expressed by (Francis–Garrison) equation [6], illustrated Figure (14, a). The second plot Figure (14, b) shows the water absorption influence on the predicted signals by the SBES model at the same water depth and without the effect of seabed interaction. From the plot, one can observe that the absorption rate of the high frequency is larger than the low frequency.

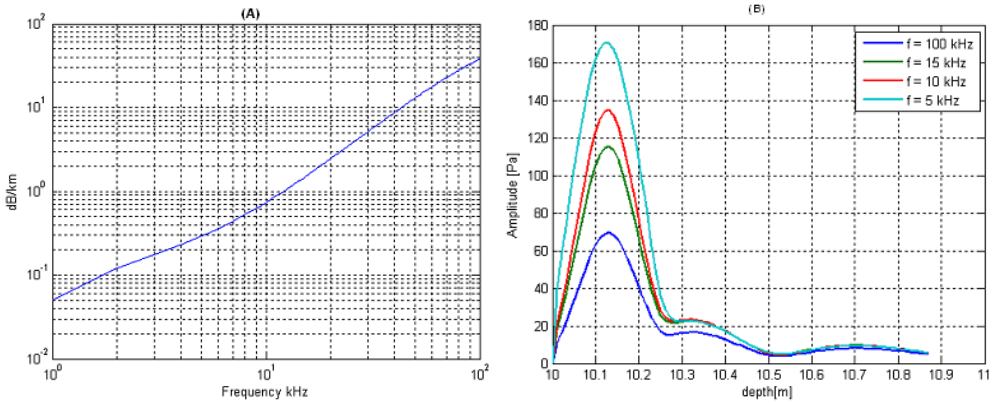

Figure 14: (A) Francis and Garrison attenuation coefficient at (depth10m, salinity 35 p.s.u, and temperature $20^{\circ}C$. (B) Influence of water absorption coefficient on the predicted signals with: Source level 250 dB, signal duration 200us, depth = 10m, Mz = 7phi.

Pulse Shape

The used SBP ‘SES-2000' System transmits a CW pulse with a relatively short duration of 200 μs . The main interest of CW pulses is their simplicity of transmission and processing. The simplest CW pulse would be a rectangular signal with constant source level. However, such signal has some performance defects due to its characteristics. The major defect is their poor spectral content which requires transmission with high instantaneous level to increase the SNR.

Fortunately, the CW pulse characteristics can be enhanced using a Gaussian-shaped pulse also known as ‘bell-shaped’. Figure (15) shows the rectangular and bell shaped pulse and their corresponding power spectrum. The rectangular shape has a poor spectral content. On the contrary the bell-shaped pulse will give a more compact frequency spectrum with fewer side lobes for the same transmission duration. It is generally desirable to minimize the side lobe level, as it is easier to be detected at low signal to noise ratio.

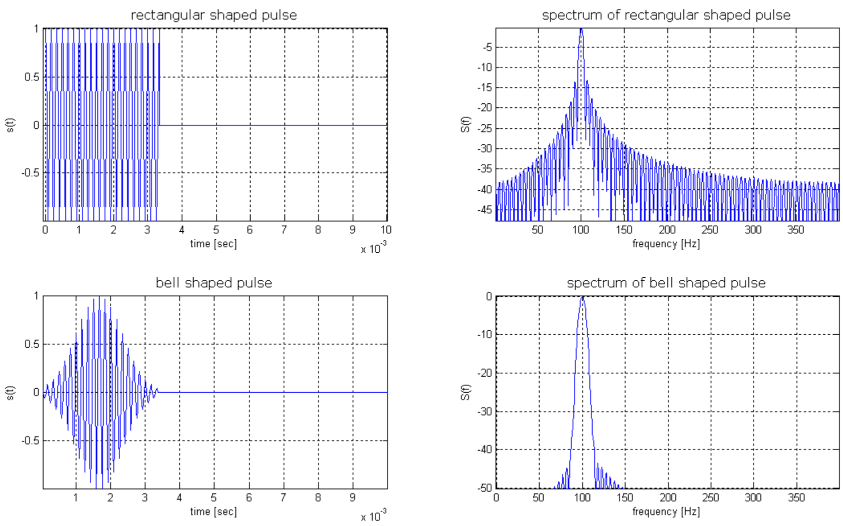

Figure 15: effect of a bell shaped amplitude modulation (bottom) on a CW pulse (top): for a given duration (at -3dB in the second case), the frequency spectrum is improved, with a strong decrease in the level of side lobes.

The bell shaped pulse enhances also another important defect caused by rectangular pulse, which is the range resolution. Range resolution is the ability of the transducer to distinguish two targets along the same radial but at different ranges. This means that the range resolution is a function of the transmitted pulse. To illustrate this, consider two targets separated by the time resolution of the signal T. The delay of the two way propagation at distances H_1 and H_2 will be separated in time by:

$$\delta t = t_2 - t_1 = \frac{2(H_2 - H_1)}{c} = \frac{2\delta H}{c} \quad (8)$$

The receiver can separate them only if $\delta t > T$. This would be the case for a rectangular shaped pulse. While with the bell-shaped pulse, it is admitted that on average signals are separable if the time difference between the signals equals the duration of -3dB (i.e. half maximum energy). Figure (16) illustrates the discussed scenario for a transducer (S) emitting a rectangular and bell shaped pulse. In the left, the time resolution is sufficient $\delta t > T$ for both cases. In the right plot, when the distance is too close between the two objects, the time resolution is too low for the rectangular–shaped pulse. While, the time resolution is still separable for the bell-shaped pulse.

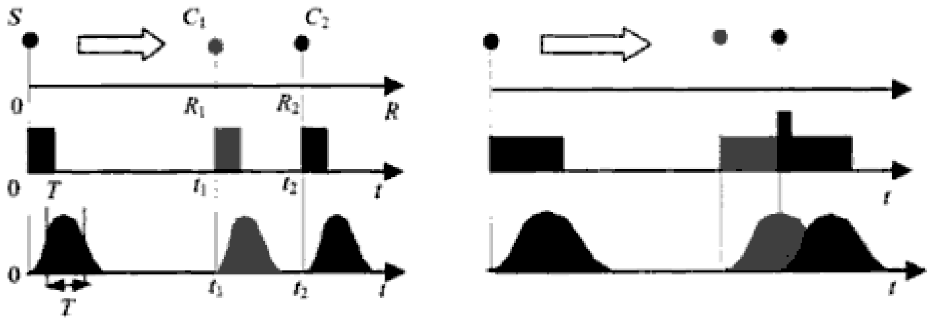

Figure 16: Time resolution and the echoes form two targets C1 and C2 (left) the time resolution of transmitted signal (in black) is sufficient to detect and separate the two targets (grey). (Right) The time resolution is too low to separate the rectangle signal, and separable for the bell shaped signal. Source [6]

To account for a Gaussian-shaped pulse in the SBES model, the source level SL is no more constant with time. Basically, one has to account for the corresponding magnitude that influences the ionisfied area. This can be applied by distributing the signal in the time domain model. Figures (17 and 18) show a modeled echo using a rectangular-shaped pulse (left), and Gaussian shaped pulse (right).

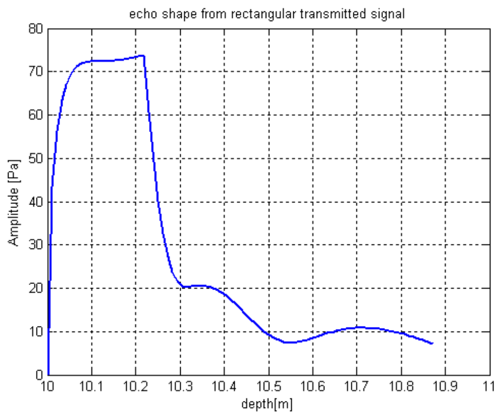

Figure 18: received echo shape from a transmitted rectangular pulse SL = 250 dB, Mz = 7 phi, Depth = 10m, f=100m

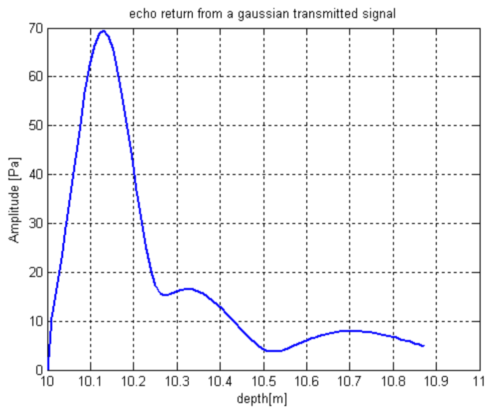

Figure 17: received echo shape from a transmitted bell shaped pulse SL = 250 dB, Mz = 7 phi, Depth = 10m, f =100 kHz

Directivity index (DI)

The transmitting $b(\varphi)$ and receiving sensitivity $b^{'}(\varphi)$ in equation (7) presents the directivity index of the transducer. It is described as the sound level difference between a directional and omni directional (same source power radiated equally in all directions) sound intensity as shown in equation (9):

$$DI = 10\log_{10}\left(\frac{I_{directional}}{I_{non-directional}}\right) \qquad (9)$$

Another expression for the directivity of a circular piston transducer and widely used between different manufactures is the ratio of the wavelength to the radiated surface diameter. Where, the aperture angle at -3dB beam width is equal to 65λ/d [36]. The larger the diameter of the transducer as compared with a wavelength sound, the narrower the sound beam can be obtained.

With SBP it is desirable to have a relatively narrow beam width to avoid unwanted reflections. Figure (19) shows the SBP beam pattern obtained from the sinc function for a primary frequency 100 kHz and transducer diameter of d=25cm plotted in solid red. Using the approximate ratio equation it gives an aperture angle of 3.9 ° which is very close to the operational SBP opening angle≈ 3.6°, plotted in dashed blue. For the secondary frequencies the beam pattern will be similar and without side lobes [25].

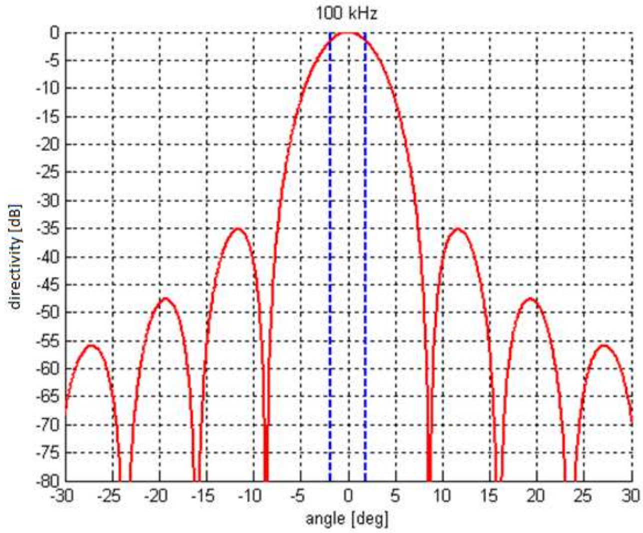

Figure 19: Transducer's beam pattern

3.1.2 Transmission loss

The factors that influence transmission loss can be grouped into two major categories: spreading and absorption losses. Spreading losses occur due to the distribution of the fixed amount of transmitted energy over a larger surface area as the signal propagates away from the source. At relatively short ranges, the increasing surface area is represented by the surface of a sphere so signal energy decay due to spreading loss at a rate of $1/R^4$,where R is the slant range from the source, figure (27).

The second mechanism of signal loss results from the propagation signal energy into heat. The two mechanisms are combined and referred to absorption loss described through:

$$e^{-4\alpha r} \quad (10)$$

Where

α is the attenuation coefficient, presented in [6],

r is the slant range, equal to R in figure (27).

In order to compare between the discussed transmissions losses, Figure (20) shows the absorption losses at 4 frequencies *(100, 15, 10, and 5kHz*) that span the acoustic frequency bands typically used for this project. From the figure it can be observed that at short ranges the spherical spreading loss dominates the absorption loss for all the frequency bands. While at longer ranges the absorption loss has greater influence on the high frequency band.

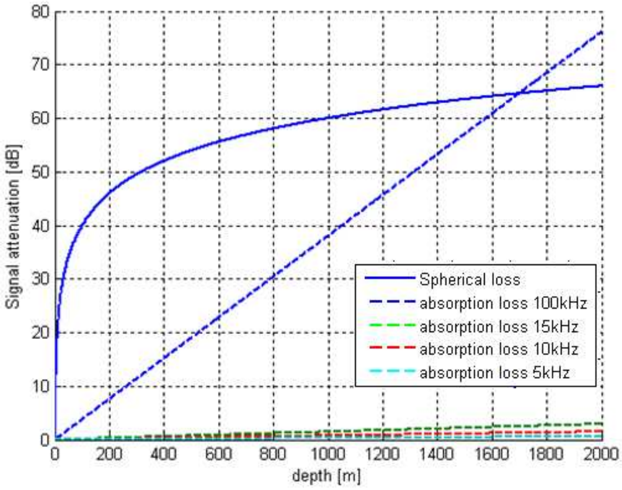

Figure 20: Acoustic signal attenuation as a function of range in sea water expressed in dB relative to the attenuation at a distance of 1 meter from the source.

In many phenomenological classification approaches, transmission loss has to be compensated and echo forms have to be normalized. Since we are using a physics-based approach such compensation is not needed. Instead we incorporate the transmission loss in the model as illustrated in figure (21).

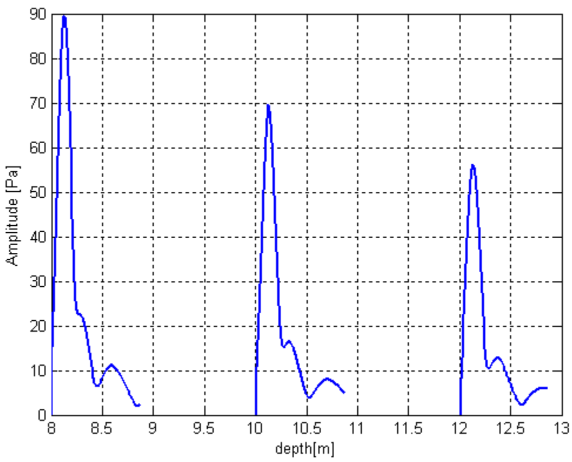

Figure 21: Effect of attenuation on amplitude echo level at depths (8, 10 and 12 m), for 100 kHz signal, Mz =8ϕ.

3.1.3 Backscatter

In this section the variation of the scattered energy $S_b(\theta)$ in equation (7) is described by the APL model [4]. Few decades ago when there was no general agreement on the physics of the scattering process, a lot of models existed based on several different hypothetical scattering mechanisms. For example Clay and Medwin based their model on sediment surface scatter, while Ivakin and Lysanov modeled it as volume scatter. By applying these models to several sites, it showed that both backscatter processes are important. The APL model by Jackson et al considered those two factors by modeling them independently, and then summed to estimate the overall intensity. The bottom back scattering strength in dB unit, can be written as:

$$S_b(\theta) = 10\log_{10}[\sigma_r(\theta) + \sigma_v(\theta)] \qquad (11)$$

Where

$\sigma_r(\theta)$ = dimensionless backscattering cross section per unit solid angle per unit area due to surface roughness.

$\sigma_v(\theta)$ = dimensionless backscattering cross section per unit solid angle per unit area due to volume scattering from below the sediment surface.

One of the main advantages of the APL model is that it is related to the sediment geoacoustic parameters. 'Mourad and Jackson' [5] Stated that there are six parameters shown in table (3) that control backscatter from the water–sediment interface and from volume inhomogeneities. These parameters are used as input data for the model. However, these parameters are often not all available. A useful sediment descriptor is then grain size M_z, which is more often available, measured in logarithmic units:

$$M_Z = 3.23\log_{10}\frac{d_g}{d_0} \qquad (12)$$

where d_g is the mean grain size or "diameter" in millimeter (mm), d_0 is the reference length (1mm) and the units of Mz are denoted by φ. Empirical parameterizations of the geoacoustic parameters are available in terms of the bulk grain size Mz [8].

Table 3: Model input (Bottom parameters)

Symbol	Definition	Short name
ρ	Ratio of sediment mass density to water mass density	Density ratio
υ	Ratio of sediment sound speed to water sound speed	Sound speed ratio
δ	Ratio of imaginary wave number to real wave number for the sediment	Loss tangent
σ_2	Ratio of sediment volume scattering cross section to sediment attenuation coefficient	Volume parameter
γ	Exponent of bottom relief spectrum	spectral exponent
w_2	Strength of bottom relief spectrum cm^4 at wave number $2\pi / \lambda = 1cm^{-1}$	Spectral strength

Roughness scattering cross section $\sigma_r(\theta)$:

. Three different approximations are used for the roughness scattering cross section in the APL model. For smooth and moderately rough surfaces (e.g. clay, silt and sand) the Kirchhoff approximation is used for grazing angles near 90° and composite roughness approximation for all other angles. Finally, for rough bottoms such as gravel and rocks, an empirical expression is used. The final surface scatter is an interpolation expression that shifts from one approximation to another. In this part we just describe the general concept of the APL model, for full details and intermediate equations the reader is referred to the documentation of applied physics laboratory [4].

Figure (22) shows the modeled surface backscatter energy distribution for fine clay and sandy gravel in the angular domain with the default parameter values of the Applied Physics Laboratory (1994) for incidence angle $(0^o - 80^o)$. The colored solid lines illustrate the margins of three approximations (Total surface backscatter, $\sigma_{kr}(\theta)$ Kirchhoff, $\sigma_{cr}(\theta)$ Composite roughness, and $\sigma_{lr}(\theta)$ large roughness). As one can see, the three approximations contribute differently to the total backscatter value depending on the sediment type and the corresponding coherency zone.

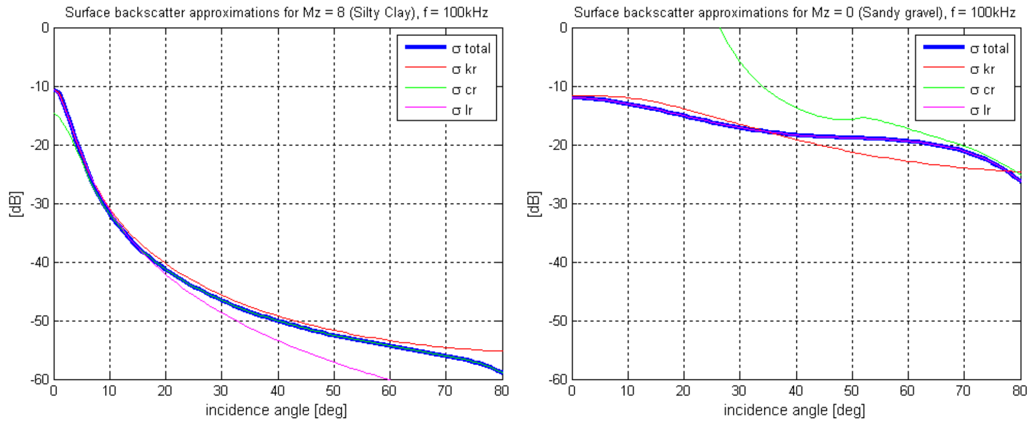

Figure 22: scatter approximations (Total surface backscatter $\sigma_r(\theta)$, Kirchhoff approximation $\sigma_{kr}(\theta)$, Composite roughness approximation $\sigma_{cr}(\theta)$, large roughness approximation $\sigma_{lr}(\theta)$).

By comparing both figures, the backscatter value of the silty clay sediment is more peaked near the 0^o than the backscatter values of the sandy gravel. Also, the backscatter value of the sandy gravel is less dependent on incidence angle. This is a consequence of the surface roughness since the surface roughness generally increases with the sediment grain size. The roughness indicator can also be observed by the approximation model that dominates the total surficial backscatter value. For example for silty clay, the surface backscatter near 0^o is best described by Kirchhoff approximation, while at greater angles, it is best described by composite roughness. On the other hand, the backscatter value of sandy gravel at the entire incidence angles is best described by large roughness approximation.

Volume backscatter $\sigma_v(\theta)$:

In many cases the scattering by sub seafloor structure contributes significantly, and may even dominate the backscattering depending on the sediment type and incidence angle. The second term in equation (11) is devoted to the volume backscatter. It accounts for refraction and transmission loss at the sediment-water interface published by Stockhausen (1963) [42] in equation (13). The expression is generalized to allow for the effect of absorption on the transmission coefficient of sediment-water interface and incorporates shadowing and slope correction in analogy with composite roughness expression.

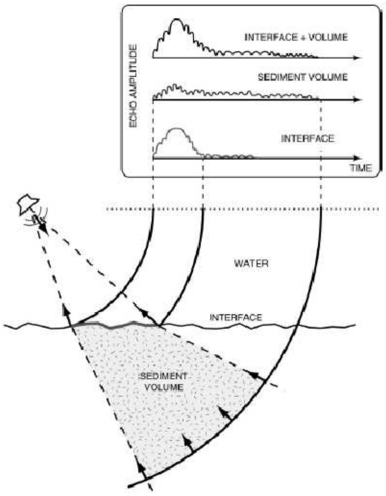

Figure 23: Illustration of volume backscatter [8]

$$\sigma_{pv}(\theta) = \frac{5\delta\sigma_2 \,|1 - R^2(\theta)|^2 \sin^2(\theta)}{\mu \ln 10 \,|P(\theta)|^2 \,\Im\{P(\theta)\}} \qquad (13)$$

Where

$R(\theta) = \dfrac{y-1}{y+1}$ is the complex reflection coefficient, with $y = \dfrac{\rho \sin\theta}{P(\theta)}$,

$P(\theta) = \sqrt{\kappa^2 + \cos^2\theta}$, with $\kappa = \dfrac{1}{\mu}(1 + i\delta)$.

The relationship depends on the grazing angle (θ), the loss parameter (δ), density ratio (ρ), sound speed ratio (μ), and volume parameter (σ_2) can be obtained from the empirical parameterization in [4].

Figures 24 and 25 show the different backscatter curves for silty clay and sandy gravel sediments at 100 and 15 kHz respectively. The blue line shows the sum surface and volume backscatter versus the incidence angle. The red and green line shows the surface and volume back scatter respectively.

From the silty clay figure(24,25), it is clear that surface scattering dominates at incidence angles less than 20°, but volume scattering dominates for incidence angles greater than 20°. One can conclude that for clay, the volume scatter approximation is perfectly adequate for modeling the surface scattering but, except near 0°, surface scattering is the dominant contributor. On the other hand, the sandy gravel figure shows that the influence of volume scatter is negligible. The whole model in this case is best presented by the surface back scatter.

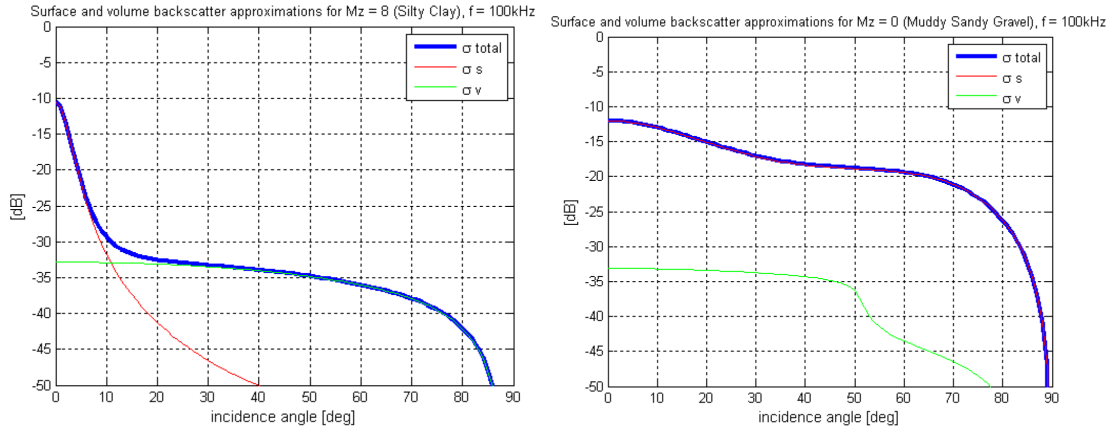

Figure 24: backscatter model approximation from left to right (silty clay Mz =8 and sandy gravel Mz = 0) at 100 kHz.

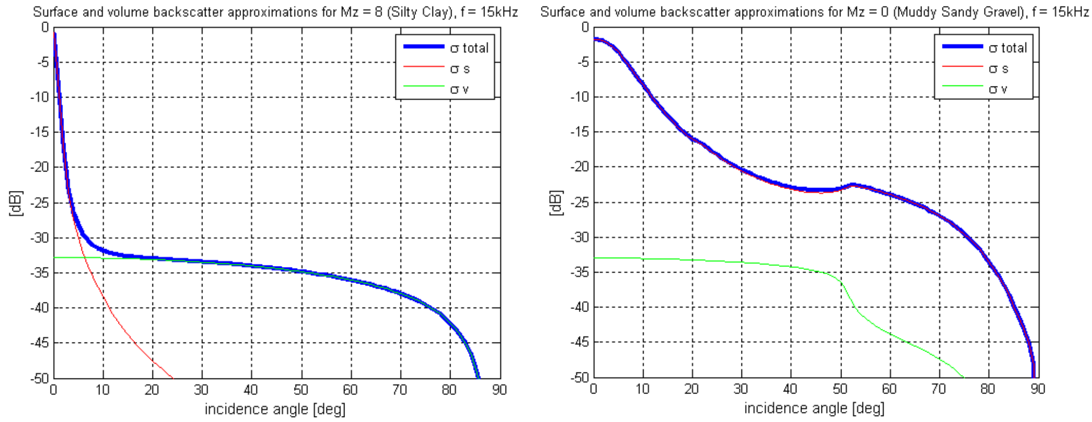

Figure 25: Backscatter model approximation from left to right (silty clay Mz = 8, sandy gravel Mz = 0) at 15 kHz.

3.2 Echo shape implementation in time domain

In order to model the signal in the time frame, we need to study the signal impact evolution with the seabed surface. The acoustic signal incident on the seafloor intercepts an active area that changes with time. The evolution of this area with time can be described by assuming that the seabed is flat, the sounder beam has a conical directivity pattern, and the seabed is the only source of reflection (i.e. multiples are ignored). The seabed ionisfied area is evolved in three distinct phases as shown in figure (26), where:

- Phase 1 - Attack – at initial instant $t_0 = 2H / c$ the impact point increases linearly till it becomes a disc with radius $S(t) = \pi H c \tau$ where $\tau = t - t_0$.

- Phase 2 - Decay - from the end of the attack phase, the ionisfied area is at maximum where t>T until the signal footprint becomes a conical pyramid of internal and external radius equal to the active area $= \pi HcT$

- Phase 3 - Release - lasting until the time when the pulse completely enters the bottom and the area decreases with time in $\pi(\theta^2 H^2 - HcT)$.

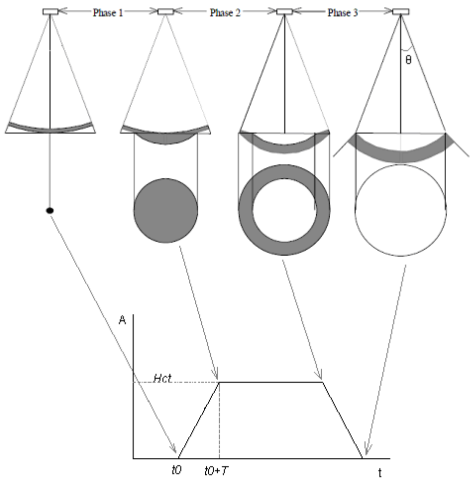

Figure 26: evolution of ionisfied area

This scenario occurs when the beam aperture is sufficiently wide for the footprint of the time signal to reach its full extend known by (short pulse or pulse limited). If the pulse is long enough *beam limited* the internal radius starts to grow only after the external radius reaches its maximum value, i.e. the whole beam footprint maybe then simultaneously insonified. The maximum backscatter area becomes ψH^2 where H water depth, ψ the equivalent solid angle of directivity pattern [36, 6].

3.3 Numerical implementation

So far equation (7) computes the received echoes as a function of incidence angle. In order to model the echo shape in time domain as seen by the transducer, we need to compute the angular dependent interaction within an elementary time at intervals of fractional pulse duration τ_p and the corresponding intensity time dependent $I(\tau_p)$. This interaction is referred as the evolution of the signal footprint or insonified area.

The discrete computation of equation (7) can be numerically computed at the discrete time intervals of (τ) indexed by (n) as integer in such that the intensity is computed at $n \times \tau$. For simplicity, the source is assumed to be a point source as shown in figure (27) at a certain height above the seabed. The source emits a spherical wave, the intersection of this wave with the bottom initially take a shape of a disk changing to that of an annulus, as illustrated in section (3.2). The discrete time interval represent the evolution of the disk and annulus as series of concentric annuli, with indices [j] i.e. the integral step can be computed by partitioning the angle$[\theta_{ij}]$ or the horizontal distance$[r_{ij}]$ into equal increments. The area of A[j] of each annulus as illustrated in figure (27 and 28) with internal and external radii calculated by:

$$A[j] = \pi(r_2^2[j] - r_1^2[j]) \qquad (14)$$

The area is then partitioned into equal increment of the ring radius to provide finer angular resolution close to normal incidence. Equation (15) is the discrete representation of equation (7) in the time domain. The transmitted waveform is Gaussian shape as described earlier in section (3.1.1). As consequence the ionisfied area at sample sequence $I(n\tau)$ is influenced by inconstant pressure level, therefore it is important to determine the correct intensity level at sample $I(n\tau - [(2R[j]/c_w)])$ by interpolating the constructive nyquist sample rate to the desired sample rate.

$$I_i[n] = \sum_{j=j_1[n]}^{j_2[n]} I_x\left(n\tau - \frac{2R[j]}{c_w}\right)\frac{S_i[j]A[j]}{a_{tt}[j]} D_M[j] \qquad (15)$$

Where:

$a_{tt}[j]$ Transmission loss in water column, through $a_{tt} = \dfrac{e^{-4\alpha r}}{r^4}$,

$S_i[j]$ Backscatter coefficient,

$R\,[j]$ Range between source and perimeter of ionisfied area,

C_w Water sound speed,

$D_M[j]$ Directivity function.

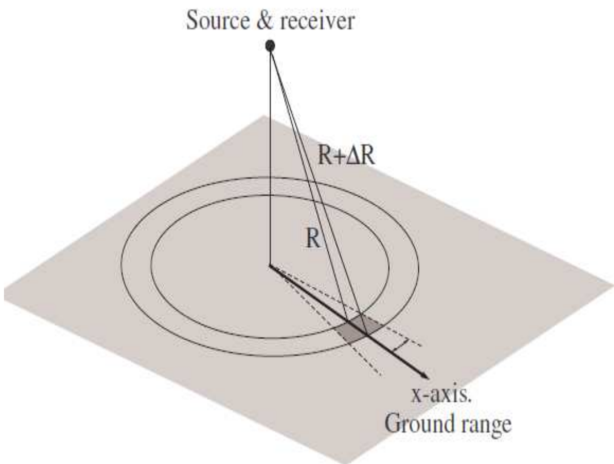

Figure 27: Imaginary sketch of transducer and seabed geometry

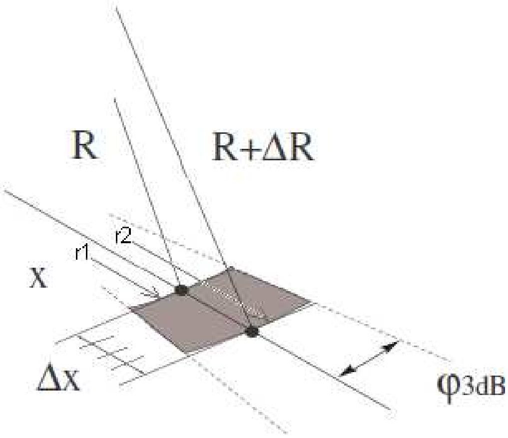

Figure 28: Elementary dimension

Chapter 4

Analysis of the High frequency echoes

This chapter is devoted to employ the model based approach 'SBES model' to the seafloor classification using the high frequency dataset. The model relies on various input parameters starting from the sensor settings to the seabed specific parameters. Some preprocessing and signal analyses are also included to optimize the matching procedure.

4.1. Data description and sensor settings

The data consists of four sets of measurements that cover four areas; each area is acquired by four frequencies, the primary high frequency (+/-100 kHz) is stated as 'HF', and three secondary low frequencies +/-(5, 10, 15 kHz) stated as LF. Figure (29) illustrates the echo prints of the four areas observed by the low and the high frequency signals. The data was acquired in the Baltic Sea near Rostock realized in 2007.

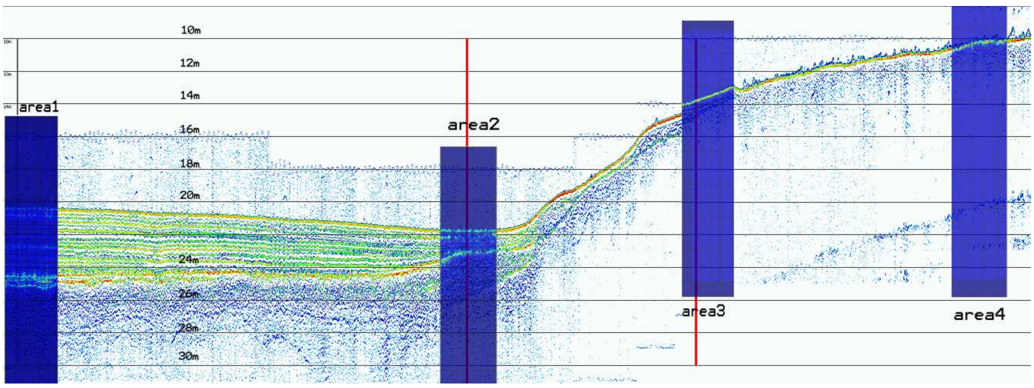

Figure 29: Echo print of sample profiler. The blue layers indicate the positions of the dataset.

Figure (30) shows a typical high and low frequency trace and their corresponding raster plot. The high frequency signal is useful to determine the accurate water depth as shown in figure (30-left). From the figure one can observe that a large component of the transmitted energy is reflected at the seabed interface and the reminding are highly attenuated in the sediment medium. On the other hand, the low frequency signal encounters less attenuation. Thus, a larger energy component will have the ability to penetrate into the sediment layers.

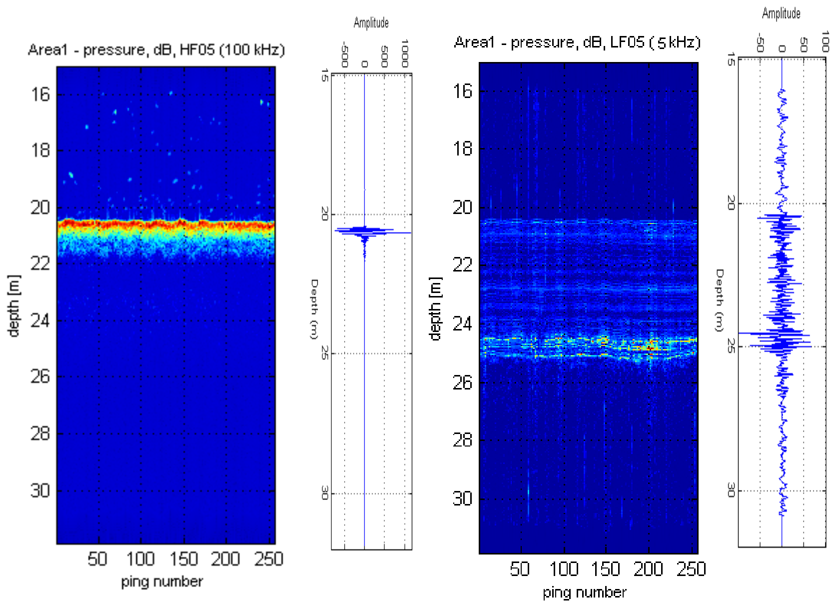

Figure 30: Data example of area 1 at 100 kHz (left), and 5 kHz (right).

The high frequency dataset of the four areas are separated and illustrated in figure (31). The first and second dataset, known as area1 and area2 have a survey length of 112m and 128.5m respectively with an average water depth of 20.5m. The third survey line 'area'3 is approximately 118m, with a starting water depth of 14m that gradually increases to 15.5m. Finally, area4 was acquired over a survey length of 105.5m and average water depth of 13m. The acoustic survey for each site was carried out at approximate speed of 10 km/h with ping rate of 6 pings/sec.

A number of grab samples were taken, and indicated that area 1 and 2 are dominated by fine grain sizes 'e.g. mud or clay', area3 by coarse sediments 'e.g. sand' and area 4 as pebble or rock. The analysis of this research will exploit the prior knowledge of sediment description as a guiding reference for the consistency of the classification results.

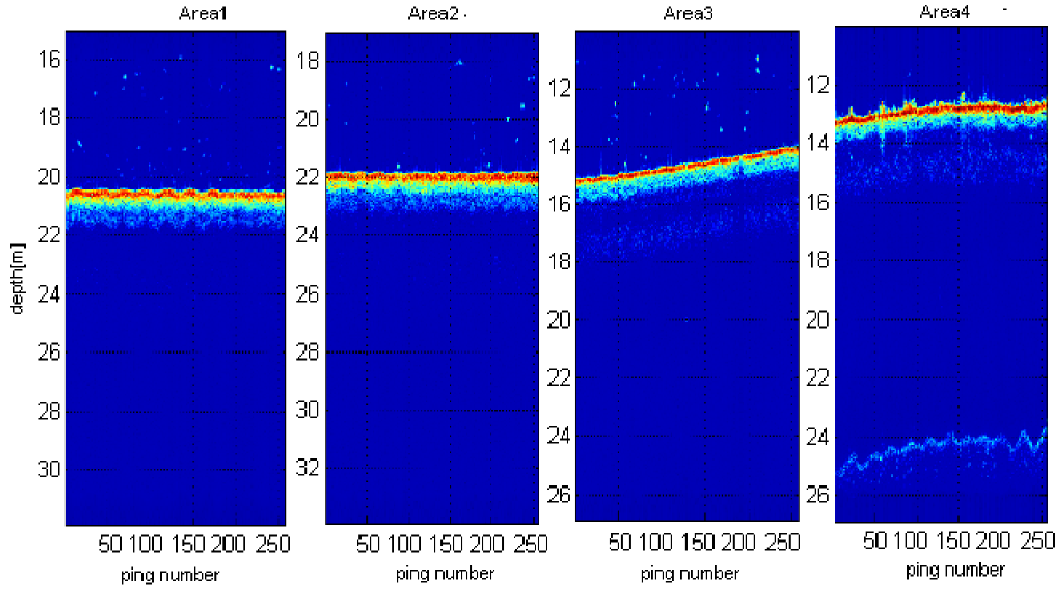

Figure 31: Raster plot of four areas, acquired at 100 kHz

The data of area 1 and 2 shows a penetration depth of approximately (1.5-2 m) which are late arrivals that might be the product of volume backscatter. On the contrary, area 3 and 4 the late arrivals are much shorter with an average penetration depth penetration of (0.75-1m) due to large absorption. The raster plot of area 4 shows high energy and topographical fluctuations, which could be due to flora, fauna or even the pebble itself. The early returns evident in the four plots are most likely caused by fish individuals near the bottom. Therefore, this data set requires scrutiny to identify artifacts that can unfairly bias the shapes and amplitudes of the backscattered echoes that will have mismatch or ambiguous sediment characterization consequences.

Further, the transducer characteristic during the acquisition process of the four areas was as follow:

The transmitted pulse is a bell shaped CW. The source level is about 240dB, and 200dB for the high and low frequency respectively with a 200 μs transmission length. The transducer is normally oriented with a transmitted half power beam width ± 1.8 degrees for the high frequency, and receiving (+/-1.8, +/-38, +/-18, +/-12.5) degrees for (100, 5, 10, 15 kHz) respectively. The data was corrected for heave and gain. The sample frequency is 96 kHz for LF data. For the high frequency, the data was shifted down from 100 kHz to below 20 kHz to fit within the nyquist range of the sample rate.

4.2. Filtering noise

Model based characterization is based on simulating the main physical processes that influence the transmitted signal. In order to improve the matching process between the modeled and the measured signal we have to eliminate or filter the presence of noise of the measured signal.

Since signals can be represented with a sum of sinusoids, we can view a signal in terms of the frequencies that compose it using the Fourier analysis. Fourier analysis gives insight on the frequencies that build up the received echo signal and consequently one can define the threshold limits of the filter in frequency domain in order to omit the presence of undesired frequencies.

Band pass filters are filters that allow frequencies within a certain band (or range) pass through the filter, while frequencies outside that range are attenuated. For bandpass filter we basically have two parameters that influence the emitted signal: the filter length (number of taps) and the pass band limits. The number of taps controls the width of so-called transition zone (gain and attenuation ripples). The band width of the bandpass filter is chosen by approximating the spectrum intersection limits of the original signal (signal + noise) and the noise.

Figure (32) shows the normalized spectrum of the original signal and the noise in decibel units. Their intersection limits is about 18 kHz and 5 kHz for the upper and lower cutoff bandwidth respectively. The center frequency is about 11.300 kHz. In this case, the cutoff band width is approximated to 13 kHz. The influence of the filtering process can be seen in figure (33-34), by enhancing the error to signal ratio E/S from -69 dB to -72 dB for area1, and from -69dB to -85dB for area4. This shows that the influence of the filtering process was not very significant for area1 but important for area4.

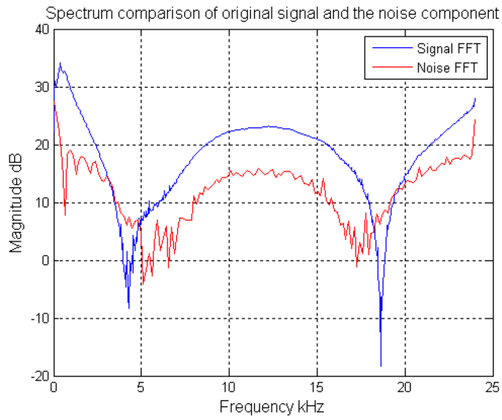

Figure 32: Normalized spectrum of original signal and noise component

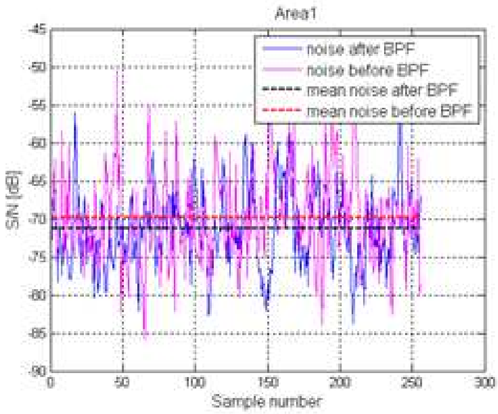

Figure 33: Error to signal ratio for area1

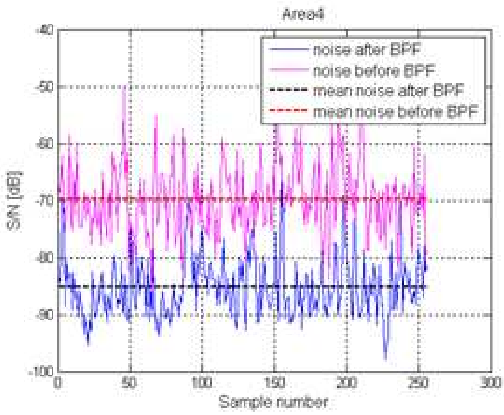

Figure 34: Error to signal ratio for area4

The final product of the filtered dataset of area1 is presented in figure (35) and their corresponding power spectrums along with their averaged values in figure (36). The average power spectrum of the raw data set shows a large spread of frequency components among the central frequency 11.300 kHz. By comparing the averaged power spectrum showed in figure (36) before (left) and after filtering (right) it can be observed that the power spectrum is now more focused around the central frequency 11.300 kHz accompanied with reduced side lobes; the difference between the main and the first side lobe is more than 50dB.

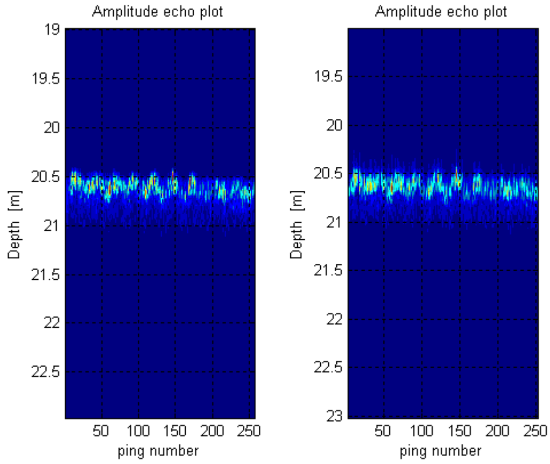

Figure 35: Raw data set (left), filtered dataset (right)

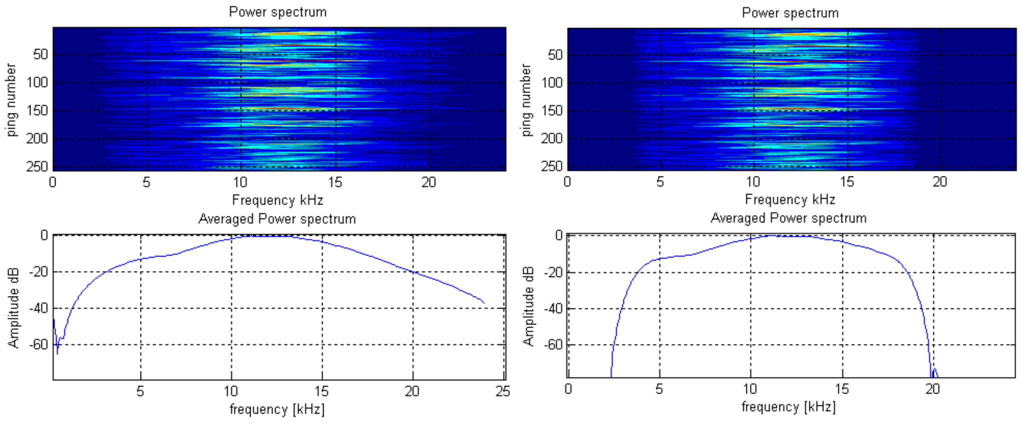

Figure 36: Spectrum of raw dataset at area1 f =100 kHz (first plot from left), spectrum of filtered dataset band pass filtered with center frequency 11300Hz with a filter bandwidth of 10 kHz (third plot from left). The 2nd and 4th plot illustrate the average power spectrum of the entire dataset.

4.3 Alignment and stacking

The waterfall plots of figure (37) show 256 traces of area1 before and after filtering. As one can see, the data still remains varying in amplitude and shape during the acquisition process. Although the data was heave compensated according to the values recorded online from the heave sensor, there is still some heave visible over consecutive pings, see figures (39-42 [a, b]). This variability influences the temporal model matching estimations, thus it has to be treated by averaging a number of signal envelopes. For the comparison process, an ensemble of *M* contiguous returns is selected and characterized by average echo sequence and mean depth to represent the transducer-bottom distance. With notice that prior to the averaging process, the echoes have to be aligned first.

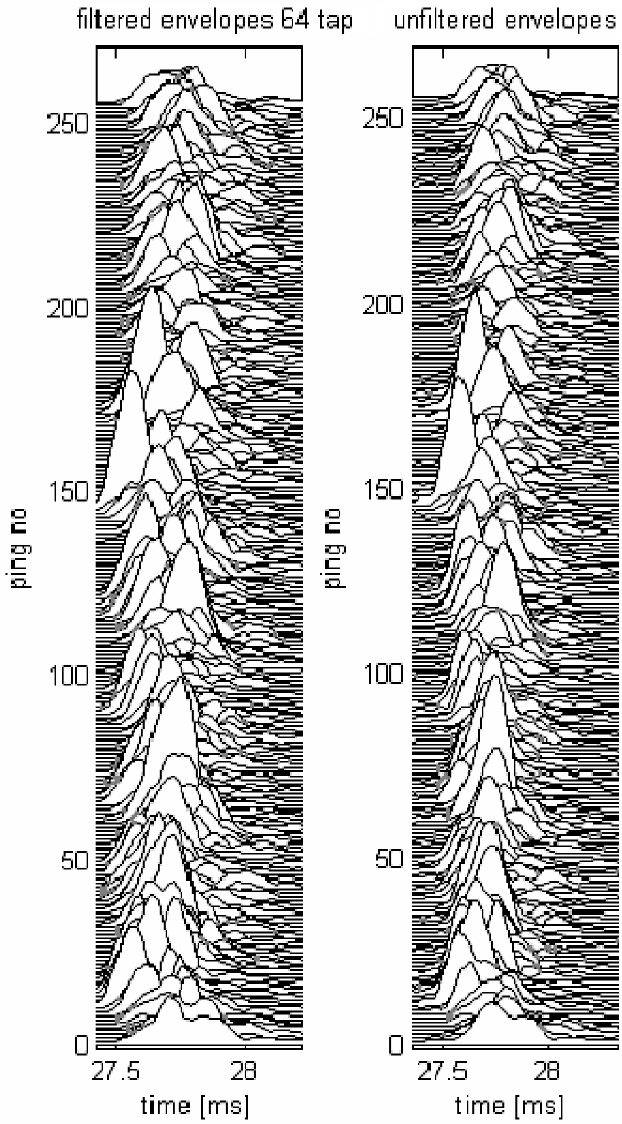

Figure 37: Waterfall envelopes

To isolate the effects of seabed type, one has to remove the effect of depth variation by envelope-stacking processes that are aligned in time. In order to compare the effectiveness of the alignment two alignment values was tested: (1) the peak amplitude, and (2) the minimum threshold.

The echo-envelope can be described by an initial rise, maximum amplitude and ending with a slow decay. Peak alignment is based on tracking and indexing the maximum amplitude value of the signal, while the minimum threshold alignment tracks and indexes the initial rise. A number of echoes within a chosen ensemble size are then shifted in time to line up with averaged ensemble peak or rising time.

A comparison between peak and minimum threshold alignment value is shown in figure (38). The figure shows a modeled signal of Mz = 8 phi in blue, and an average of 15 samples that are aligned with the two threshold values. Figure (38-left) shows threshold alignment at 10% of the maximum peak. The main property of minimum alignment is that it preserves the integrity of the echo's rising edge, which is more suitable for bottom echoes that have low stochastic variability and is less suitable for noisy signals or bottom echoes from rough sediments.

On the other hand, peak alignment is more suitable for bottom echoes that have high stochastic variability such as high noise or echoes from rough sediments. Peak alignment yields more symmetric distribution of signal energy about the alignment index as shown in figure (38-right)

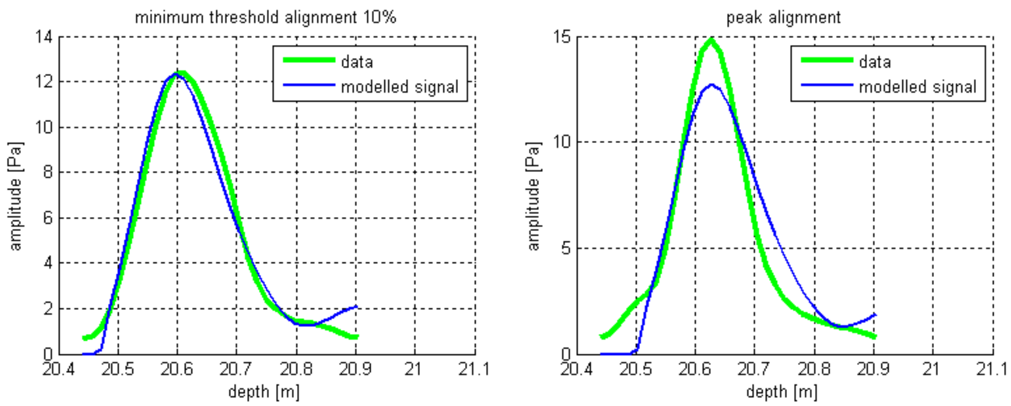

Figure 38: Minimum and maximum alignment results

The numerical implementation of the alignment process starts by selecting a temporal feature, in our case threshold of (10 %, 50% and 100%) was chosen. Once the selected feature index is determined the echoes are shifted in time to line up with the averaged signals feature.

For each return signal the alignment index is determined through:

$$j_i = j(p \geq p_{T_t}, 1),$$

Where 1 is the first index, and $1 \leq i \leq I$, the mean alignment index can be then calculated by:

$$j_m = \frac{1}{I}\sum_{i=1}^{I} j_i$$

Where I is the number of pings used, which leads to a delay of $d_m = j_i - j_m$ for each individual i pings. Finally the averaged echo signal of ensemble n is computed as follows:

$$p_a[n] = \frac{1}{M}\sum_{m=1}^{M} p[m, (n - d_m)] ....n = 1, 2, ...N \quad (16)$$

The outcome of this procedure results in a reduced data set that is smoothed and has less stochastic variability. The averaged $p_a[n]$ signals represent the approximated seabed type for a small area, which then can be compared to the modeled signals.

A number of analyses were applied on the modified dataset illustrated in figures (39-42). Each figure contains four plots, (a) are the raw dataset which could not be used due to their stochastic behavior and their irregular shaped envelopes. Plots (b) are the filtered dataset which had a smooth shaped envelopes but their variability was not stable which consequently resulted in various classification results. Plots (c) are the aligned raw dataset with a stack size of 15 signals, which had a low ping-to-ping variance, but their envelopes had irregular shapes which was not practical for the model-matching process. Plots (d) are the aligned filtered envelopes, which were more practical for the comparison process.

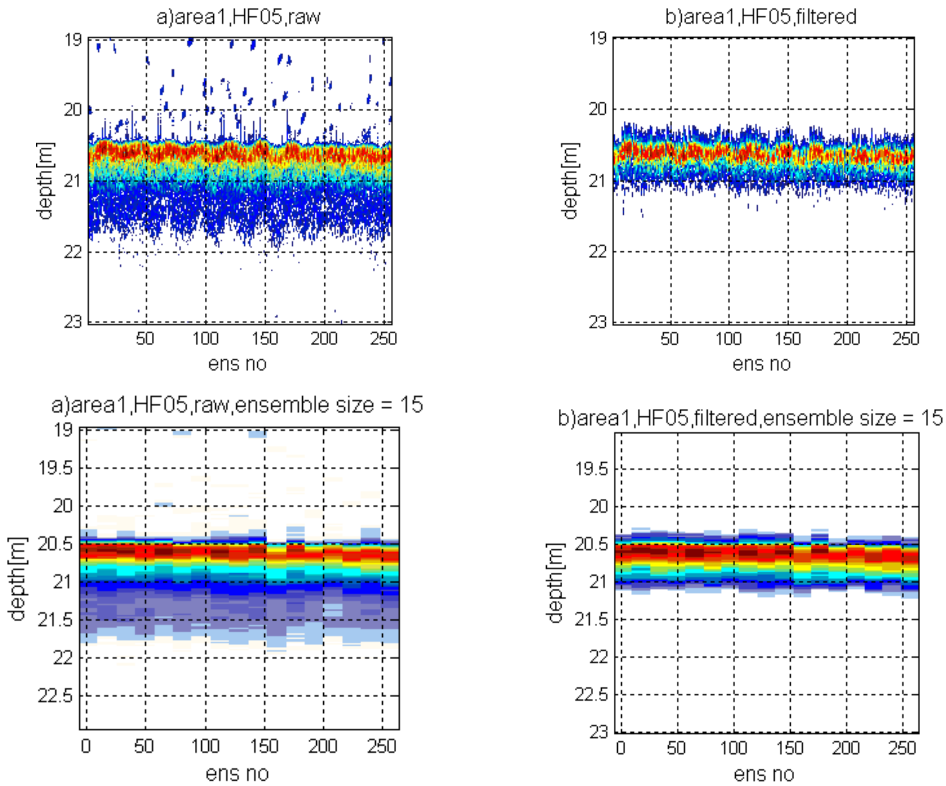

Figure 39: Raw dataset (a), filtered data (b), stacked raw data (c), stacked filtered data (d) for area1.

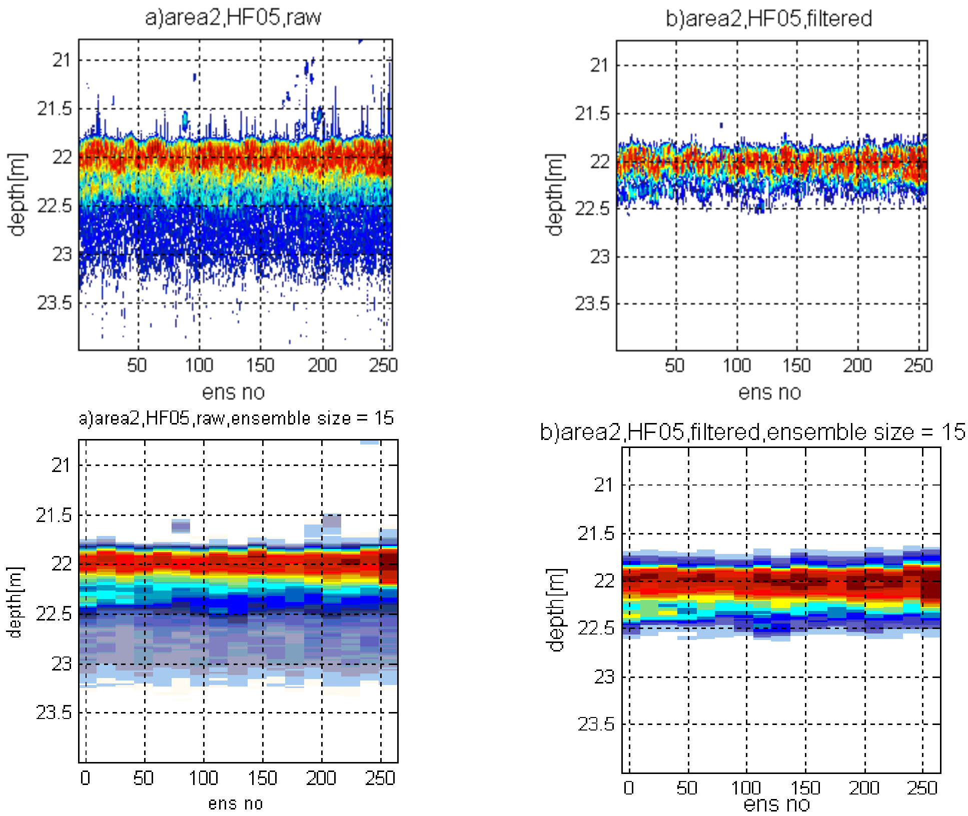

Figure 40: Raw dataset (a), filtered data (b), stacked raw data (c), stacked filtered data (d) for area2.

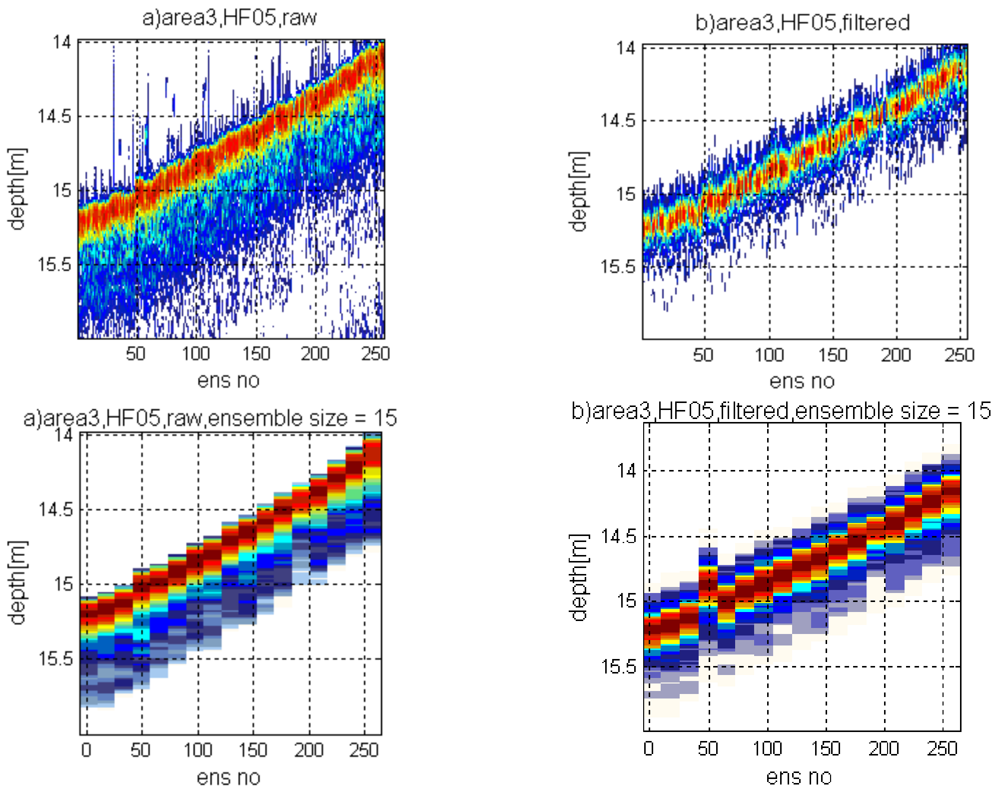

Figure 41: Raw dataset (a), filtered data (b), stacked raw data (c), stacked filtered data (d) for area3.

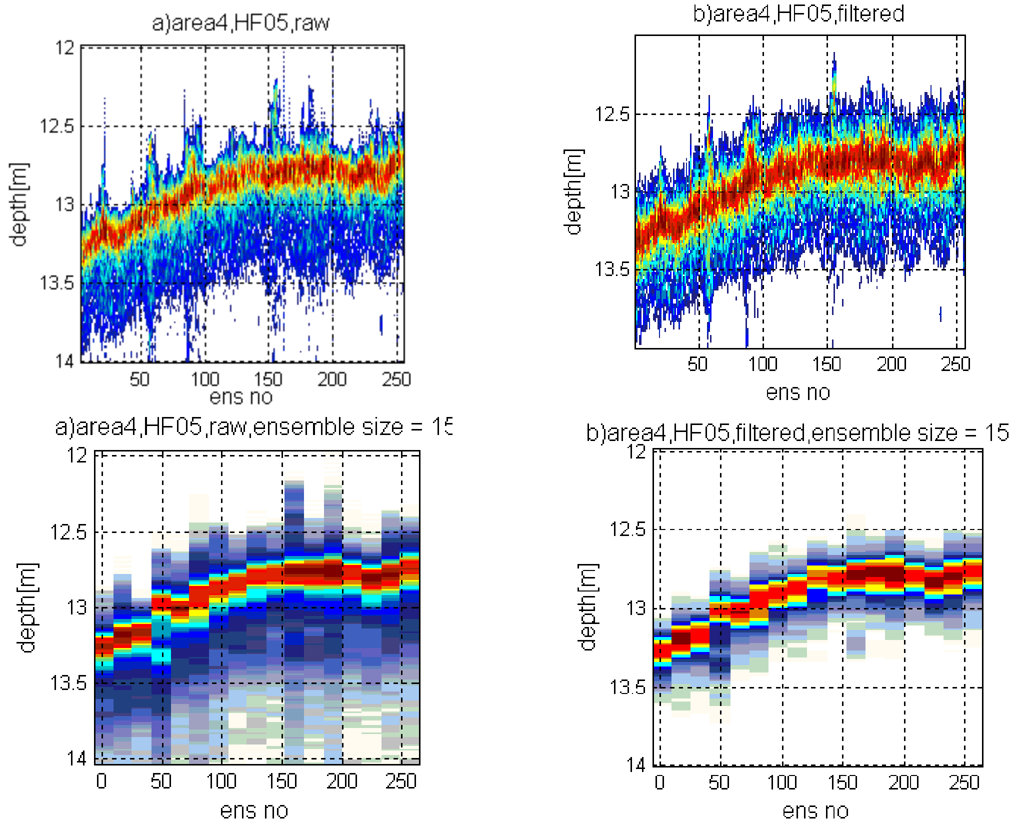

Figure 42: Raw dataset (a), filtered data (b), stacked raw data (c), stacked filtered data (d) for area4

4.4. Ensemble size

For proper averaging, an adequate ensemble size has to be chosen. The size selection is based on the tradeoff between spatial resolution and ensemble variance. Suppressing ping-to-ping variability by stacking more consecutive echoes together allows the sediment information in the echo shape and spectral nature to express itself in spite of noise-like variability. This tends from that the clusters are better separated from their neighbors by distributing the residuals which reduces the ping-to-ping variability. However, one should account that averaging over a large number of signals will change the actual echo signals which will lead to ambiguous classification

The cluster size can be governed by two factors, the geometrical artifacts such as apparent periodical patterns in figures (39-42, a) and the degree of similarity between echo shapes. Nonlinear parametric sources provide a very narrow directivity which is essential for sub bottom horizontal resolution requirements. With the relatively small water-sediment foot print size (approximately 1.5m at 20m depth) and vessel speed of (10-15km/h) the footprint will have overlap percentage of (15%-30%) depending on the ping rate.

In order to check the degree of similarity between the filtered received echoes, a correlation coefficient matrix was computed. The $n \times n$ correlation matrix of figure (43) shows some interesting features per area that can be used as guidance for the stacking size.

For example, area1 and area2 signals are highly correlated on large spatial scale, which indicates that both areas are dominated by single sediment type. Area1 shows also some tiled patterns which indicate the influence of the periodical pattern as observed earlier in figure (39, a). However, this pattern is not of great influence since the correlation coefficients remains high. Thus, any stack size can safely be used in these two areas without influencing the signal properties.

Contrary to the first two areas, area3 and area4 in general showed less correlation which indicates higher presence of ping-to-ping fluctuation. Moreover, the highest correlations were also observed diagonally over shorter spatial scale ’15-20 pixels’, which is likely due to the seabed geometrical inclination at area3, and the first 100 traces in area4. Consequently, a stack size of 15 signals was chosen to be aligned and averaged for the entire dataset. This means that the dataset per area will be described by 17 ensembles with an approximate spatial resolution of 6-7 meters.

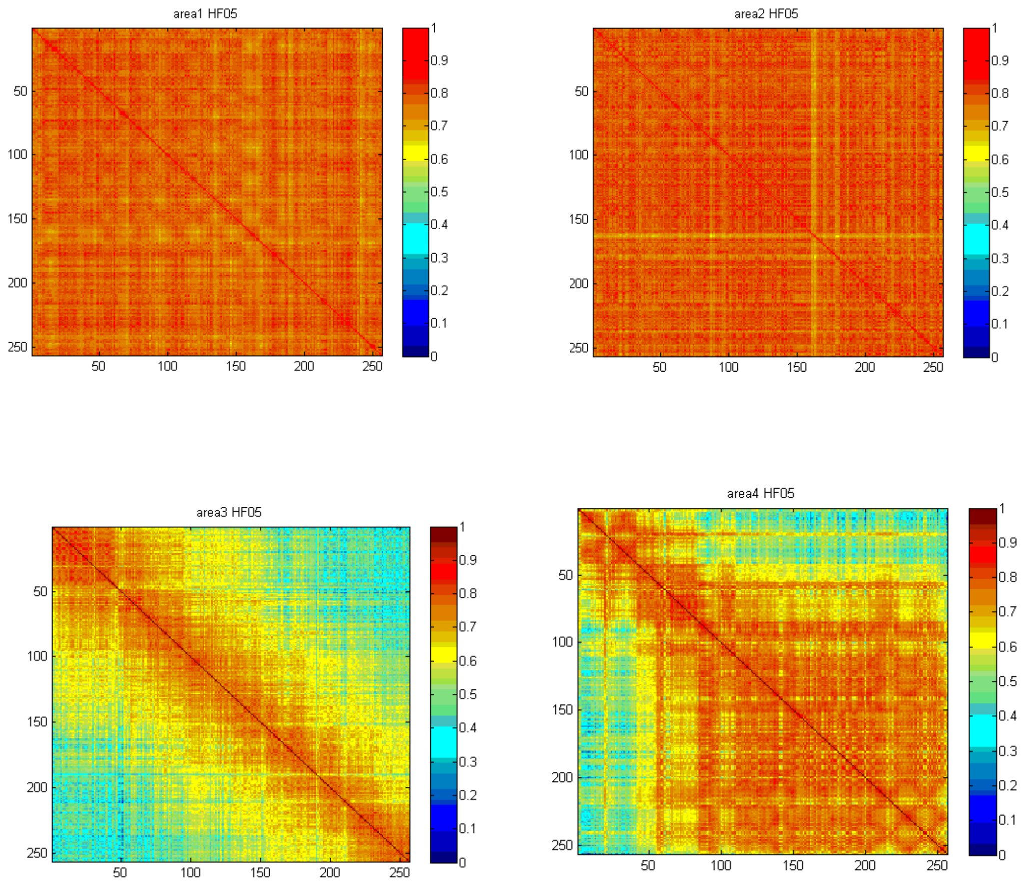

Figure 43: Data correlation coefficient matrix for echo envelopes of the four areas at 100 kHz.

4.5. Data comparison

4.5.1 Comparison process

Within the matching process we match the stacked measured envelopes with envelopes of the model. The measured bottom echoes consist of a pulsed CW signal, whose envelope yields a pressure sequence, expressed in Pascal (Pa), whereas, the model yields intensity. Intensity is the power passing perpendicularly through a unit area of 1m^2. The comparison process is based on rms pressure because the intensity introduced complications in the matching procedure. Therefore, equation (17) is applied so that the intensity can be written in terms of rms pressure alone.

$$\hat{p}_a[n] = \sqrt{\rho v \hat{I}[n]} \qquad (17)$$

Where $\hat{I}[n]$ is the computed discrete intensity and ρ and v correspond to the seawater density and sound speed. To measure the degree of fit between the modeled and measured data, we use a signal to error S/E function equation (18) or E/S which is just the inverse; *a high value of S/E signifies a 'good match'*. This function is easy to implement since it is independent from scale and signal length. However, with the presence of noise, comparison of the whole trace is not convenient. Since the model models the signal at the signal receiving time, we need to truncate the measured signal beneath a given minimum threshold value to remove the remained noise. The rising index of the truncated signal is used as an estimate for the water depth for which the model is run. The signal tail 'i.e. last index' is used as ending time of signal computation.

$$S/E = \frac{\sum_{n=n1}^{n2} p_a^2[n]}{\sum_{n=n1}^{n2} (p_a[n] - \hat{p}_a[n])^2} \qquad (18)$$

One problem remains before the matching process which is that the scale of the stacked envelope and the model is different. This tend from that no information about the true power of the source is available. In principle the source should be calibrated first to know the exact emitted power in the medium to have a direct match between the modeled and measured envelopes. However, with the absence of such calibration, the initial modeled-measured echo shapes comparison still did show an agreement on the signal shape but somehow biased by a scale factor. Intuitively, since the same instrument was used at the four areas, this bias should be constant or nearly constant in all surveyed areas. In order to isolate the scale factor, a linear regression model was applied using equation:

$$y = Ax \quad (19)$$

Where y is the measurement vector, A is the modeled vector and x is the scale factor.

4.5.2 Estimating geoacoustic parameters

The measured echo envelope characteristics i.e. (echo duration, rising slope peak value, decreasing slope, decreasing time, etc) are directly associated with the backscatter values from a specific sediment type. In the physics based model, the sediment type is described by six geoacoustic parameters $(\rho, v, \delta, w_2, \sigma_2, \gamma)$ as illustrated earlier in chapter 3 table (3). These parameters are input in the model to generate a theoretical echo envelope. Within the inversion process, we aim to search for the best set of input parameters that gives the maximum fit between the modeled and the measured ones.

If the six input parameters are unconstrained, the parameter search space will be six-dimensional which yields a complication of large number of good fits that does not necessarily represent the correct solutions [13]. Therefore, instead of searching in all dimensions, we start by 1D search over Mz to establish the general sediment (fines, sand, and rocks). Hamilton and Bachman [31] described a relationship between the density ratio and sound speed ratio and relate both to the mean grain size of the seafloor sediment.

Mean grain size diameter is the most useful descriptor for sediment type characterization which can range from clay (diameter ~ 0.00039mm) to boulders (diameter~ 256mm or greater). A phi value ϕ scale conveniently represents the mean grain size according to $\phi = -log_2 d/d_0$ where d is the mean grain diameter in mm and d_0 is the reference diameter equal to 1mm. The sediment naming conventions are given in table (4) from the classification schemes of Wentworth scale [30]. These values will be used as threshold for the classification results.

Table 4: Boundaries of sediment types

Phi Value ϕ	Mean grain size diameter (mm)	Sediment type
$\phi \leq (-1)$	$2 \leq \phi$	Gravel/rock
$1.0 < \phi \leq 5$	$0.06 < \phi \leq 2.0$	Sand
$5 \leq \phi$	$\phi < 0.004$	Clay

Theoretically, modeled echo returns have different behaviors with respect to sediment type. For example, signals classified as mud are dominated by volume backscatter as it contributes to the total signal energy by a moderate peak rising rate and a long tail due to volume scatter. Sand echoes are characterized by a dominant surface backscatter and low volume scatter elongation, coarse sand and rocky sediments are completely dominated by surface scatter and an absence of volume scatter.

Technically any sensor will have a fraction of noise due to reverberations, boat noise, water surface, etc. These noises were filtered in the observation and the post processing process. For the matching procedure, proper truncation threshold is essential to eliminate the remained noises and to track the rising index of the measured envelope and its echo duration. Low truncation biases the rising index. While, high truncation might cut off important signal features and yields improper classification results.

Bottom echoes from substrates whose relief is small compared to the acoustic wave length exhibit consistent temporal energy distributions, particularly at near normal incidence. In these situations stacking and averaging via minimum threshold preserves the integrity of the echoes rising edge and echo shape. The minimum threshold appears to be ineffectual in high-noise environments where signal shapes are highly variable such as coarse sand and pebble sediments which are extremely rough relative to the acoustic wave length. Under these conditions higher threshold value might be more efficient and may yield average echoes which are more consistent with the theoretical and local classifications.

Figure (44) shows the classification result for the four dataset using the default APL model parameters, with alignment threshold set to the minimum (alignment 10%, truncation 5%). The classifications started by areas where substrates relief is small compared to the acoustic wave length. The matching process showed good E/S and moderate classification consistency for area1 and area2. The dominant mean grain size was classified as fines $5 \le Mz \le 9$, with presence of some outliers classified as coarse sediments. The sandy area had even better E/S than the muddy area, and acceptable classification consistency that varied within the sandy zone $1 \le Mz \le 5$. For the pebble area the classification consistency was very poor as the classification results were highly fluctuating between mud and pebble mean grain sizes.

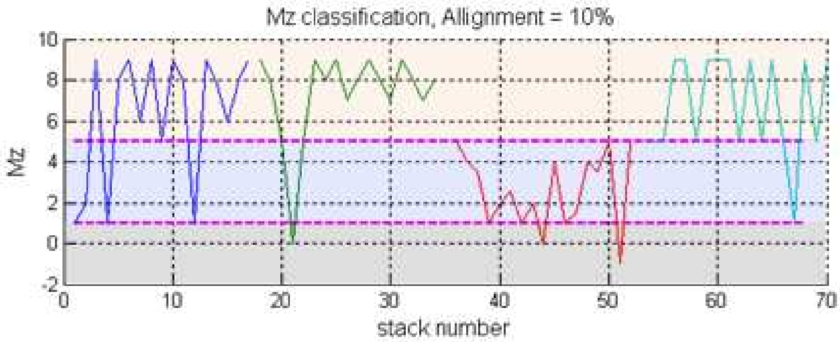

Figure 44: Minimum threshold alignment 10%, 5% cut-off and the corresponding classification result. Predicted mean grain size for the four areas (Bold blue: area1, green: area2, red: area3, cyan: area4). The pink doted lines present the sediments regions fines, moderate, and coarse sediments.

Figures (45) shows the classification results, by applying a threshold alignment 50% of maximum amplitude and truncation limit 5% of observed signal. As one can see now we do observe better consistency for the classification for area 3 and 4 and low consistency for area1 and 2.

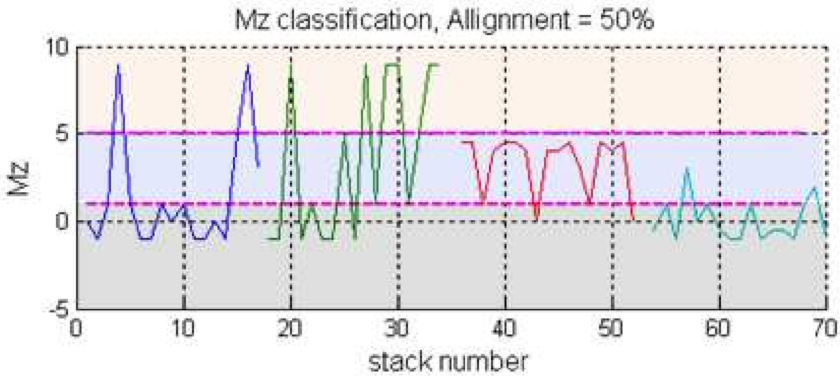

Figure 45: Threshold alignment 50%, 5% cut-off and the corresponding classification result. Predicted mean grain size for the four areas (Bold blue: area1, green: area2, red: area3, cyan: area4). The pink doted lines present the sediments regions fines, moderate, and coarse sediments.

A third iteration was applied with threshold set to (alignment 100%, truncation 5%) illustrated figure (46). The figure shows large variation of sediment type which does not agree with the general description of the four areas.

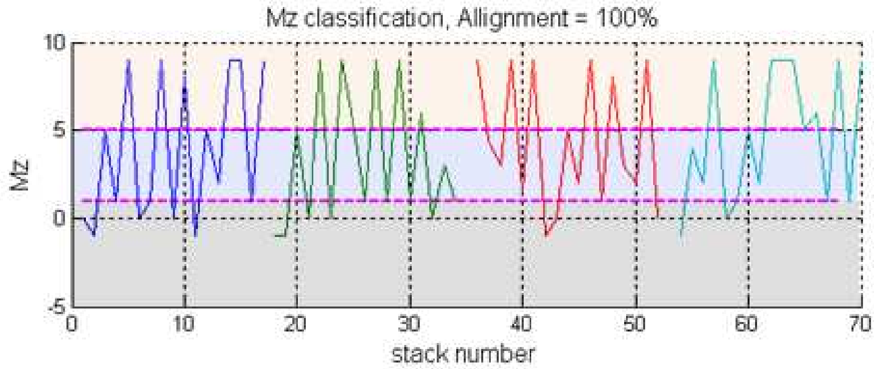

Figure 46: Threshold alignment 100%, 5% cut-off and the corresponding classification result. Predicted mean grain size for the four areas (Bold blue: area1, green: area2, red: area3, cyan: area4). The pink doted lines present the sediments regions fines, moderate, and coarse sediment.

Figure (47) shows the E/S ratio that represents the degree of match of the observed echoes to the modeled echoes for the four areas. Alignment at 10% gave low E/S ratio which means high degree of fit for area1, 2, and 3 while area 4 had low degree of fit. On the contrary, alignment at 50%, the matching degree had good results for area3 and area4. Finally the peak alignment at 100% of the signal had high E/S for all areas.

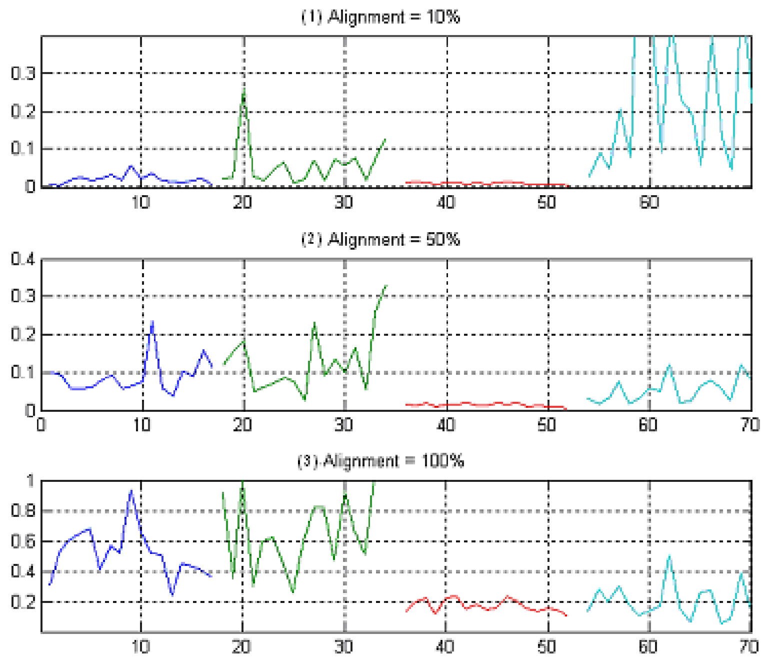

Figure 47: Error to signal ratio (E/S) for area1 (blue), area2 (green), area3 (red), and area4 (cyan).

Conclusion

Contrary to SBES sensors, SBP has a very narrow beam width which makes it very difficult to capture the full backscatter process, and might not be the most effective sensor for surface classification. Based on the SBP limitations, and the previous results, alignment and truncation techniques are of great importance to distinguish the slight difference of backscatter behavior of different sediment types.

By comparing the alignment thresholds, the minimum threshold was more suitable for relatively smooth surfaces such as area1, area2, and area3. For areas with high fluctuations such as area4, alignment with higher threshold (50%) is more suitable since it yields a more symmetrical distribution of signal energy about the alignment index.

Interestingly, this issue was also discussed in [8]. It was concluded that group delay alignment 'basically a method that aligns the echoes based on their energy' of highly fluctuated echoes due to reflections from rough surface, yields average echoes that are more consistent with their theoretical predications. The following plots in figure (48) show three randomly selected matching results from the four areas. The y-axis is placed at the start of the received signal 'i.e. the seabed depth' so the signal features from different areas can be easily compared such as elongation, peaks, and shape.

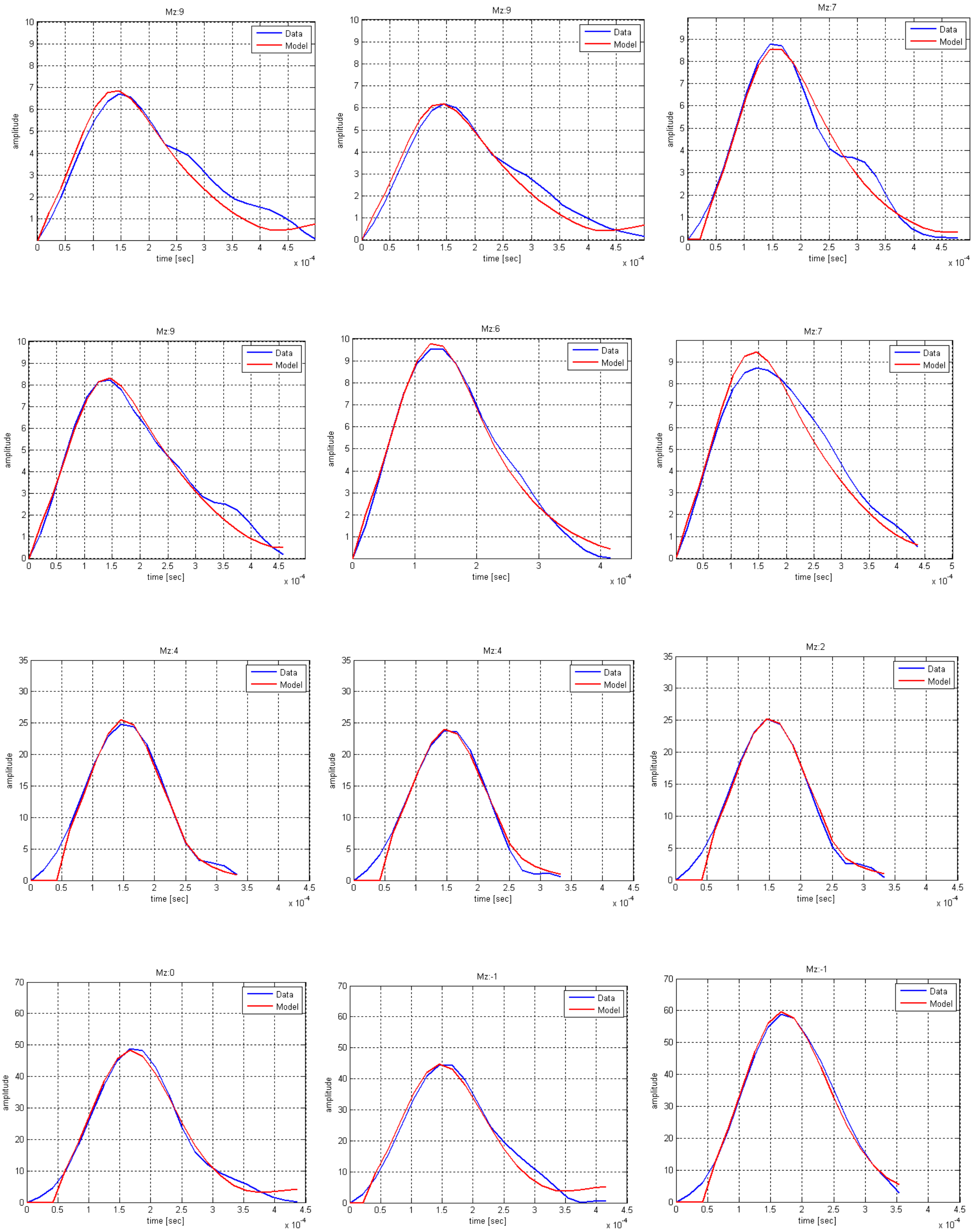

Figure 48: The first three rows show the observed and modeled signal for area1, area2, and area3 with minimum threshold (10%) and cut off (10%). The fourth row shows the observed-modeled matching for area4 with alignment of 50% and 10% cut off.

The following table summarizes the classification conclusions. From the table, it can be seen that the E/S ratio is not enough to conclude the final classification, since matching process is sensitive to the alignment threshold values, and scaling technique. Therefore the best way is actually to find the best process that gives the same result as the ground truth values. Therefore in this research the conclusion is based on general description of the area together with the minimum E/S ratio.

Table 5: classification result

	Alignment		
	10%	**50%**	**100%**
Area1	Good E/S, classification were within fine sediment margins	Low E/S , classification were not consistent	Low E/S , classification were not consistent
Area2	Good E/S, classification are consistent within the fine sediments	Low E/S ratio	Low E/S , classification were not consistent
Area3	Good E/S, classification are distributed within sand margins	Good E/S Classification are shifted more to fine sand	Low E/S , classification were not consistent
Area4	Low E/S ratio, with inconsistent results	Good E/S ratio Stable Mz classification within the coarse sand/rocky boundaries	Low E/S , classification were not consistent

The geoacoustic parameter estimation process can be achieved by the following procedure:

1- Obtain the acquired data set with feasible sampling frequency to capture the proper echo envelope; sampling frequency has to be at least twice as nyquist sampling rate to prevent sample aliasing. The Nyquist theorem states that a signal must be sampled at least twice as fast as the bandwidth of the signal to accurately reconstruct the waveform [10].
2- Apply filtering techniques to reduce unwished frequency components that might affect the Hilbert transform.
3- Signal incoherency, heave effects, and seabed depth deviation of the mean have to be stacked and aligned. We start by minimum threshold alignment with the objective of finding areas that are dominated by fines.
4- The averaged ensemble envelope time stamps are used to generate the equivalent modeled signal.
5- The model-data matching degree is quantified by error to signal ratio, and the low value of E/S signifies ‘good’ match.
6- With the goal of deriving unambiguous matches between the temporal model and data, 1D search technique is used by iterating over all sediment mean grain sizes where the six geoacoustic sediment parameters are related to Mz.
7- The successive Mz are then checked by the classification consistency function. If classification presents high fluctuation within the chosen Mz per trace or area, the alignment technique has to be changed by increasing the threshold value.
8- The solution produced with the 1D search defines a seed vector (Mz, w_2, σ_2) appropriate for second stage (3D) optimization over roughness spectral strength, volume scatter, and the mean grain size associated with impedance contrast and sediment attenuation coefficient.

The following flow chart illustrates the used classification paradigm for sediment classification using the high frequency dataset.

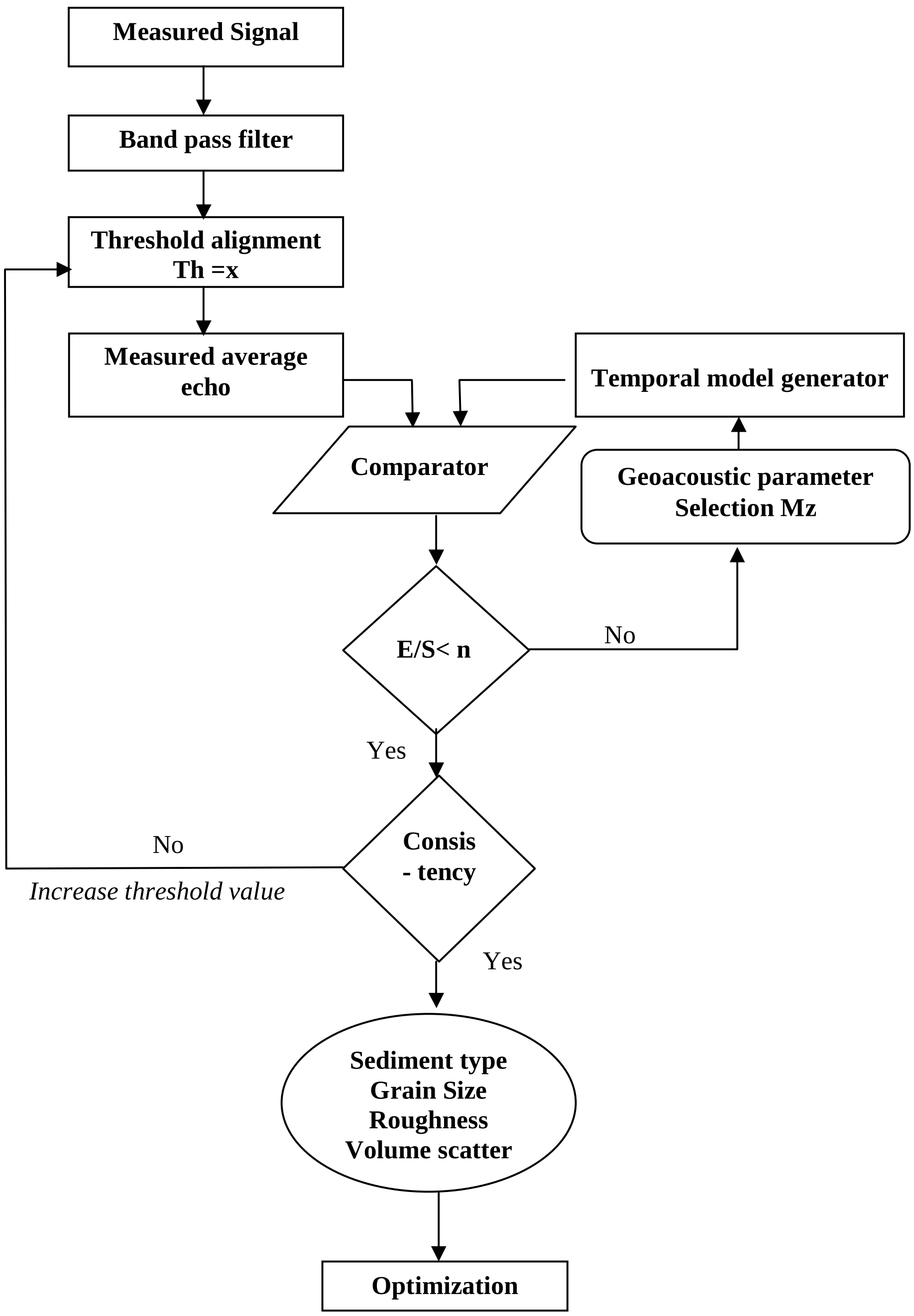

4.5.3. Sensitivity of geoacoustic parameters

The results of 1D search using Mz showed a feasible model-data fit. This fit can be enhanced by searching into a second layer 'set of new variables' (ρv , w_2 , σ_2). These three parameters were stated as the three geoacoustic parameters that affect the backscatter value at near normal incidence [9, 4] and express:

1) The ratio of sediment to water acoustic impedance by ρv

2) The size of surface roughness, specified by w_2 , and

3) The volume backscatter by σ_2 .

a) Impedance contrast

Reference [31] showed that the grain size is correlated to the water-sediment impedance contrast and the sediment attenuation coefficient through linear regression equations. As a general rule, an increase in grain size parameter Mz is inversely correlated to the impedance contrast and attenuation coefficient, which lower the overall level of backscatter and elongates the receiving time due to volume scatters. On the other hand, coarse sediments and rocks cause higher peaks that are distributed over shorter time.

b) Surface roughness and scatter

Topographical roughness can be described through statistical parameters such as the root mean square (RMS) of the elevation distribution [10]. This is simply the standard deviation of the relative height measurements and it has applicability to scattering models [14]. However, the rms does not provide any information on the size and spacing of seafloor roughness features that can be superimposed with ripples or dunes. Therefore, the APL model represents the surface roughness as isotropic two dimensional relief spectrums and by a power law for wave numbers comparable to the acoustic wave number:

$$W_2(k) = w_2 k^{-\gamma} \quad (20)$$

In the used APL model, we account for seafloor macro roughness by convolving the smooth surface with a roughness response. From Applied Physics Laboratory (1994)[4], the surface roughness power spectrum w_2 is related to the rms rough height (h) over 1 m long track by $w_2 = 0.00207h^2$ in cm^2 . The lab experiment of APL-UW showed that there is a considerable spread in the observed scattering strength for given sediment. Most of this spread was ascribed to the w_2 and σ_2 , therefore these two parameters are allowed to vary. The roughness parameter controls the width and rise time of the signal peak. The limit, which is recommended was suggested by a combination of numerical and physics consideration. One should pay attention that the extreme values are unlikely to be encountered in practice and may yield suspecting results. The limit is as follows:

$$0.0 \leq w_2 \leq 1.0$$

According to [12], the spectral exponent (γ) values signify the topographic correlation parameter within the same overall variance, whereas the spectral strength (w_2) parameter quantifies amplitude.

c) Volume scatters

Volume scatter is very important for fine sediments; its influence can clearly be seen in the time domain signal as it affects the energy levels in the tail of the signal. In general, the grain size parameter controls the simulated echo's peak amplitude, whereas the volume parameter controls the energy in signals tail. For fine sediments, it dominates the overall energy, while its contribution decreases with coarser sediments. The recommended limit for the volume backscatter by [4] is:

$$0.0 \leq \sigma_2 \leq 1.0$$

Chapter 5

Analysis of the low frequency echoes

Introduction

In the previous chapter, the time dependent backscatter model was used to simulate a vertically oriented, uncalibrated echo-sounder operating at 100 kHz. With such signal, the received echo energy can be successfully predicted. This is not the case with a transmitted signal operating at lower frequencies. Seeding the SBES model with a low frequency as an input can predict only the first part of the received echo ‘water sediment interface’ as shown in figure (49).

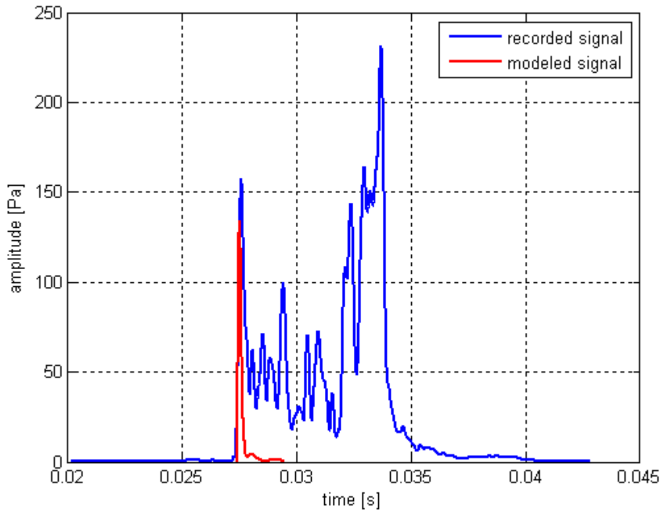

Figure 49: Comparison between modeled and measured echo envelope received from a transmitted pulse of 15 kHz.

Therefore, in this section, an attempt is made to investigate the feasibility of two alternative physics based models that account for further sub layer interactions. The models predict the reflection coefficients at each layer and inverted afterwards to the corresponding mean grain size.

The building blocks of the first model are based on the recent work of D.Simons [11]. This method basically infers the mean grain size of the water sediment interface, by inverting the SBES echo energies via empirical relationships between sediment properties and the acoustic reflection coefficient. To predict the sub layers mean grain sizes, the model had to be extended to account for layer absorptions, reflections and transmissions coefficients to compute the received energy as seen by the sensor. By computing the amount of energy received from a time window, the reflection coefficient can be estimated and correlated with Hamilton and Bachman's (1972) sediment reflection coefficients. Since the reflection coefficient is a function of sediment impedance, the results can then be inverted to the corresponding mean grain size.

The second model is based on the same concept, where the mean grain size is inferred from the reflection coefficient at each layer. The major difference between the two methods is how the reflection coefficient is computed. In the first method the reflection coefficient is expressed as the ratio of the received energy to the attenuated transmitted energy. In this case the energy losses are applied on a calibrated transmitted energy, and the attenuation process is theoretically applied on the nominal transmitted frequency. In the second model, the reflection coefficient is reversely computed. Theoretically, this can be achieved by expressing the reflection coefficient as the ratio of the compensated received energy for losses to the transmitted energy. In this case the transmitted energy is assumed to be equal to the total compensated received energy. In order to compensate the received energy for losses, the transmission losses are applied on the spectrum of the received energy which means that the transmission loss is a function of frequency at each layer.

Data description

The low frequency measurements were illustrated earlier in figure (29) chapter 4. The SBP reading shows very low penetration at 'area3 and area4' which indicates the presence of hard seabed surface. At greater depths 'area 1 and 2' the penetration depth reaches approximately 8 meters below the water-sediment interface, where high reflections are observed at 4m depth. This implies that the signal penetrated soft sediment first and suddenly encountered hard sediment causing high reflections due to the presence of high impedance contrast.

5.1 Signal processing

For, the low frequency signals, the receiving half power beam width was much wider than during transmission. This configuration was adjusted specially for this project in order to receive the complete transmitted energy, which consequently picked up more noise (i.e. low SNR).

SNR is a measure used to quantify how much a signal has been corrupted by noise. This can be achieved by comparing the amount of signal with the amount of background noise in a particular signal, such that a higher SNR indicates the background noise is less noticeable. This can roughly be estimated by getting the ratio of (signal + noise) 'e.g. mean signal energy around the strongest reflector' to the mean signal energy of the water column as noise which usually gives a fairly good estimation of SNR.

The SNR depends on the received noise energy and the received signal energy. The received signal energy mainly depends on the transmitted signal energy, reflection and attenuation process at the seafloor. Noise may come from different sources and contributes in different ways to the total SNR. Generally the noise is frequency dependent; low frequency signals are subjected to high noise components. This can be seen at the bottom plots of figures (50, 51), which compare the SNR of area1 and area4 at 15 and 5 kHz before and after filtering. The different SNR results from the frequency dependent noise level: the lower the center frequency, the lower the source level but the higher the noise level. In figure (51), although the SNR of the unfiltered dataset at 5 kHz was higher than the 15 KHz, the band pass filter increased the 15 kHz SNR more than the 5 kHz.

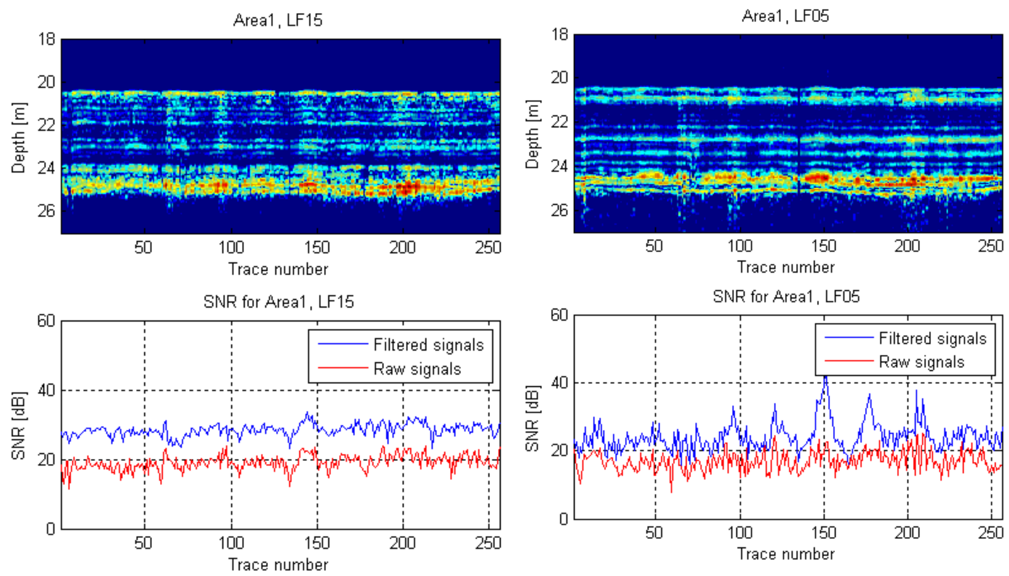

(a) (b)

Figure 50: The top plots in figures (a,b) show the observed data of area1 at 15 and 5 kHz respectively. The bottom plots show their corresponding SNR before filtering (red) and after filtering. At the 15 kHz figure(a) the mean SNR was improved from 19.0406dB to 28.3975 dB, while at the 5 kHz figure(b) the mean SNR was improved from 16.9577to 24.1038dB.

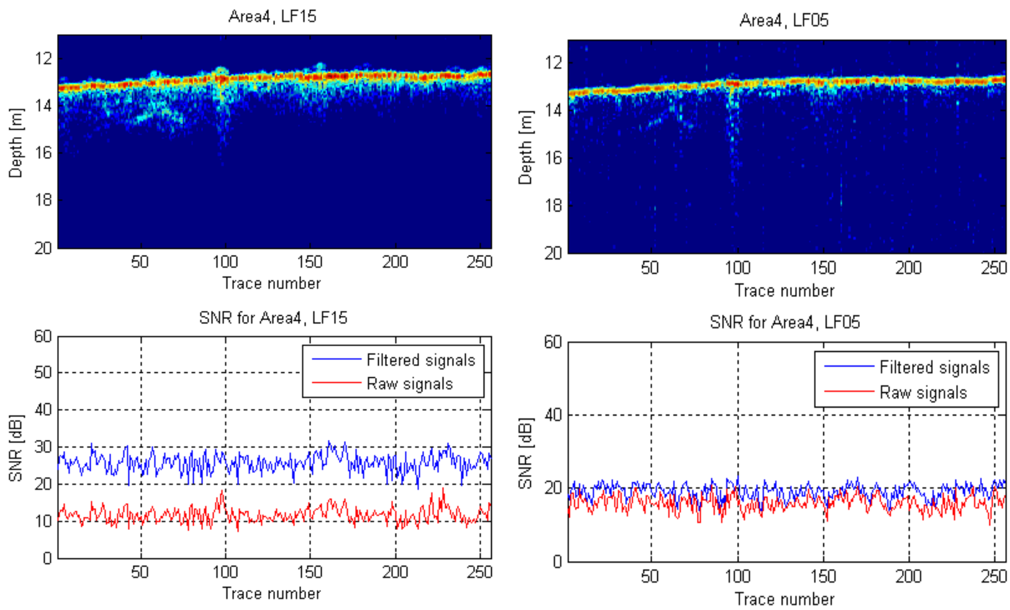

(a) (b)

Figure 51: The top plots in figures (a, b) show the observed data of area4 at 15 and 5 kHz respectively. The bottom plots show their corresponding SNR before filtering (red) and after filtering. At the 15 kHz ‘figure-a’ the mean SNR was improved from 11.6786dB to 25.74 dB, while at the 5 kHz ‘figure-b’ the mean SNR was improved from 15.84 to 19.10dB.

In order to remove undesired noises from the received signal, a band pass filter was used with specific bandwidth in order to increase the SNR. This was achieved by employing a similar approach as was used in chapter4, through computing the intersection threshold between the signal and signal noise spectral components. The resulted bandwidth was about 6 kHz, which didn't differ much from the theoretical one. With a known pulse length $200\mu s$, the corresponding bandwidth is about 5 kHz (bandwidth =1/pulse length)

Noise filtering was excited on the entire dataset. The observed maximum power spectrum was chosen as centre frequency of the design band pass filter. Alternatively, nominal centre frequency was chosen if the observed maximum power spectrum had a large offset from the design centre frequency. Figure (56) shows the filtered dataset and their corresponding power spectra are shown in figure (57). As the figure shows, the frequency band of the filtered data is now more focused around the desired centre frequency, and the large difference between main and next side lobe is obtained.

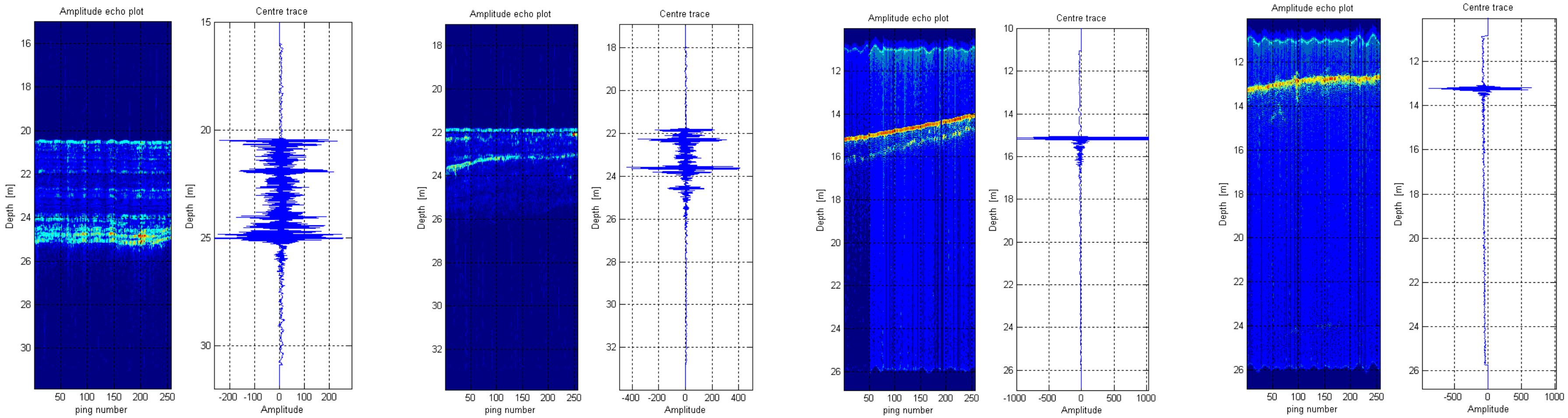

Figure 52: From left to right area (1, 2, 3 and 4), 15 kHz, unfiltered data

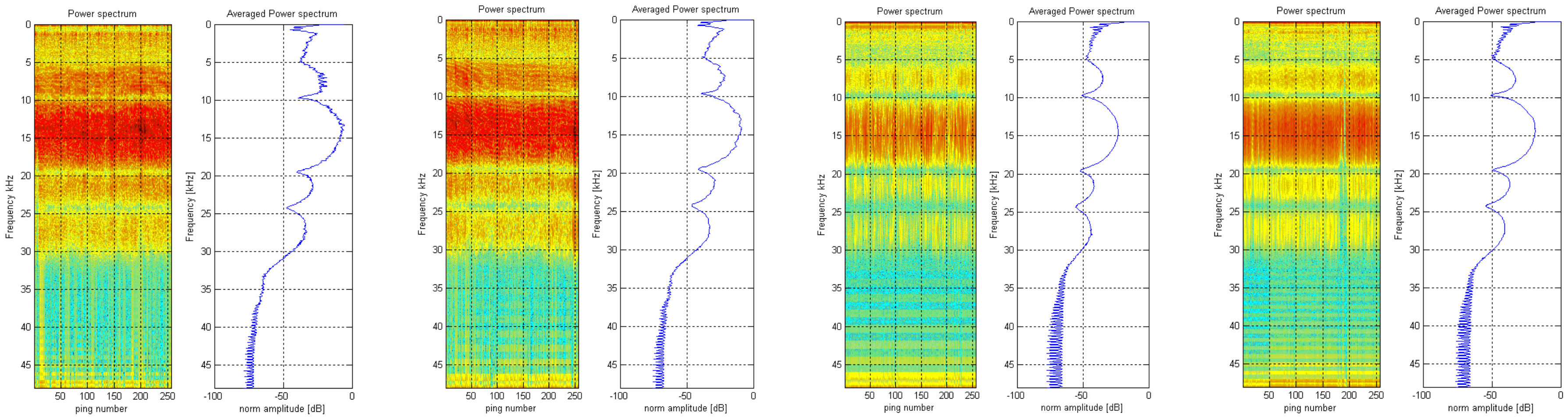

Figure 53: The power spectrum of the four areas (left) and their average (right) of 15 kHz, unfiltered data.

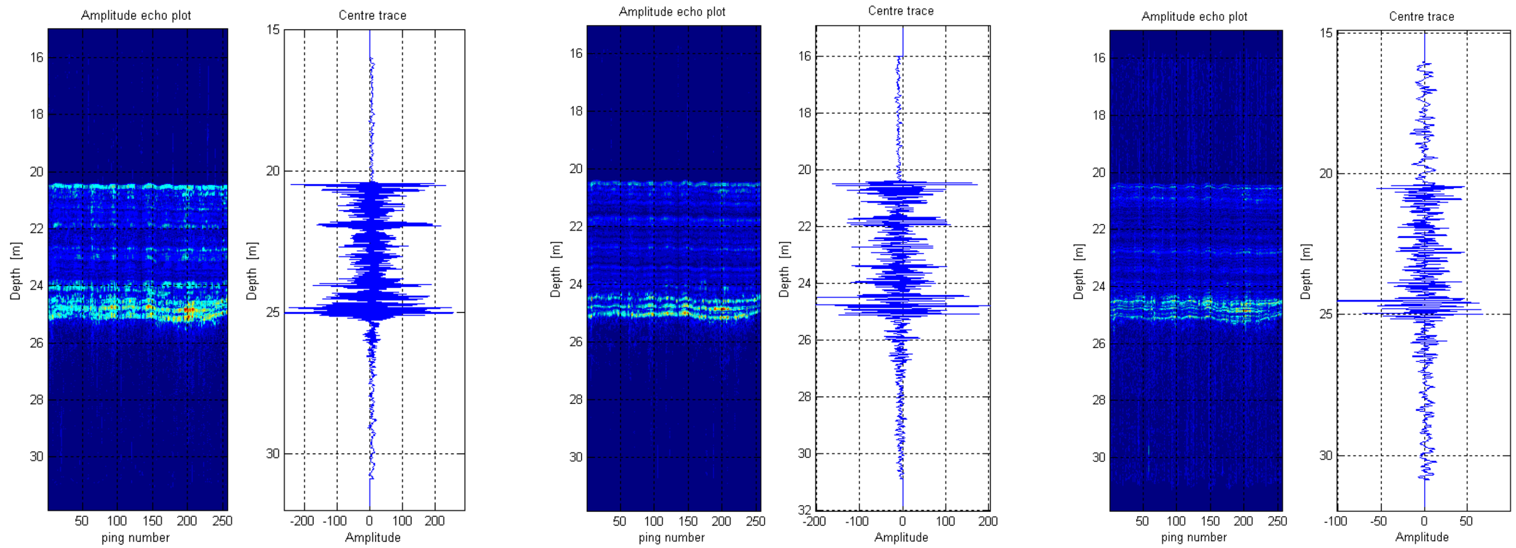

Figure 54: From left to right, frequencies (15, 10, and 5 kHz) unfiltered data of area 1

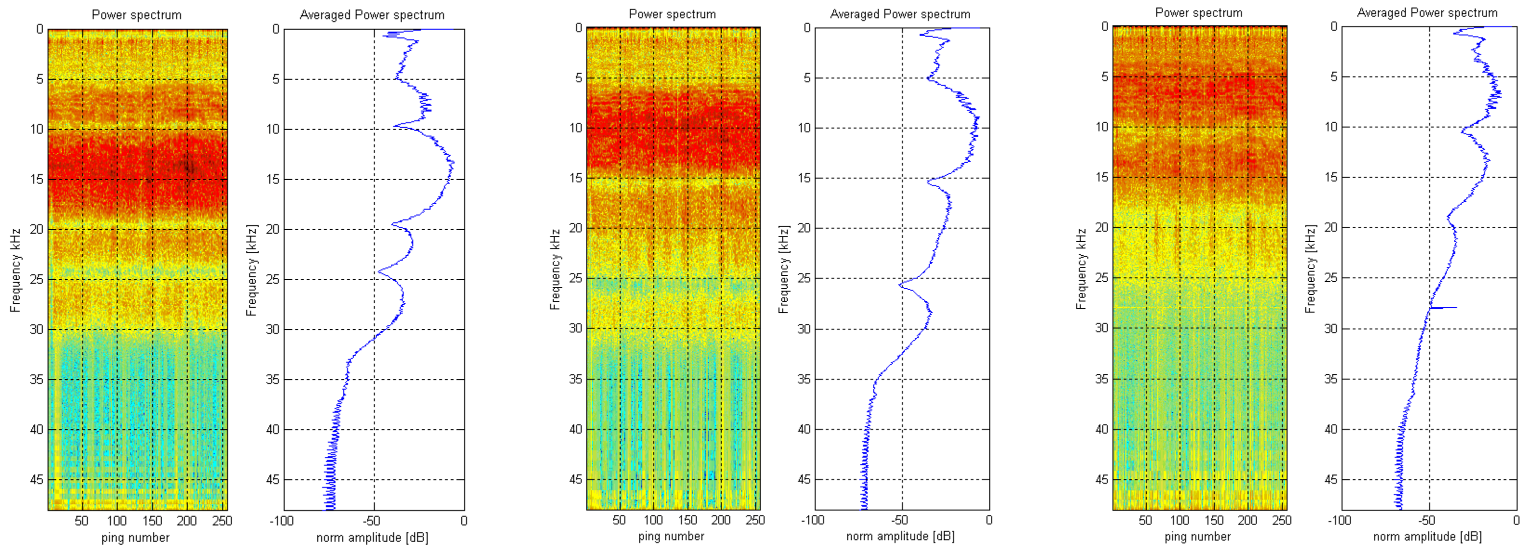

Figure 55: From left to right, frequencies (15, 10 and 5 kHz), power spectrum of unfiltered data of area 1

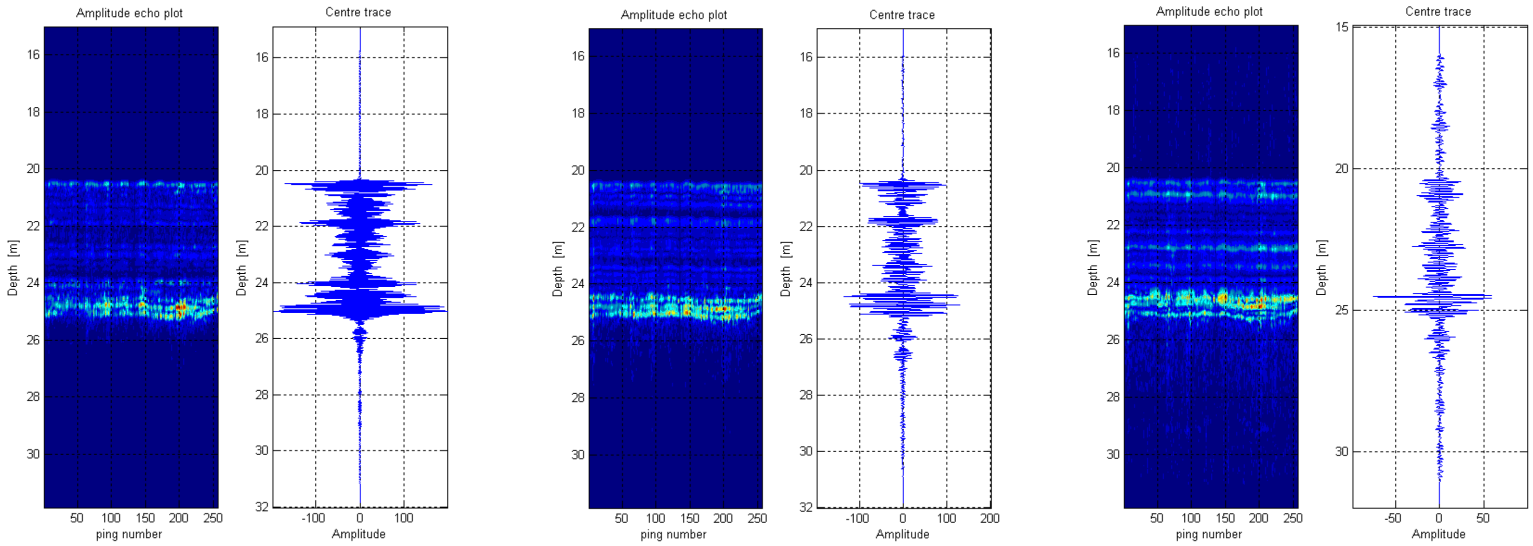

Figure 56: Filtered dataset of area 1, from left to right (15, 10, and 5 kHz)

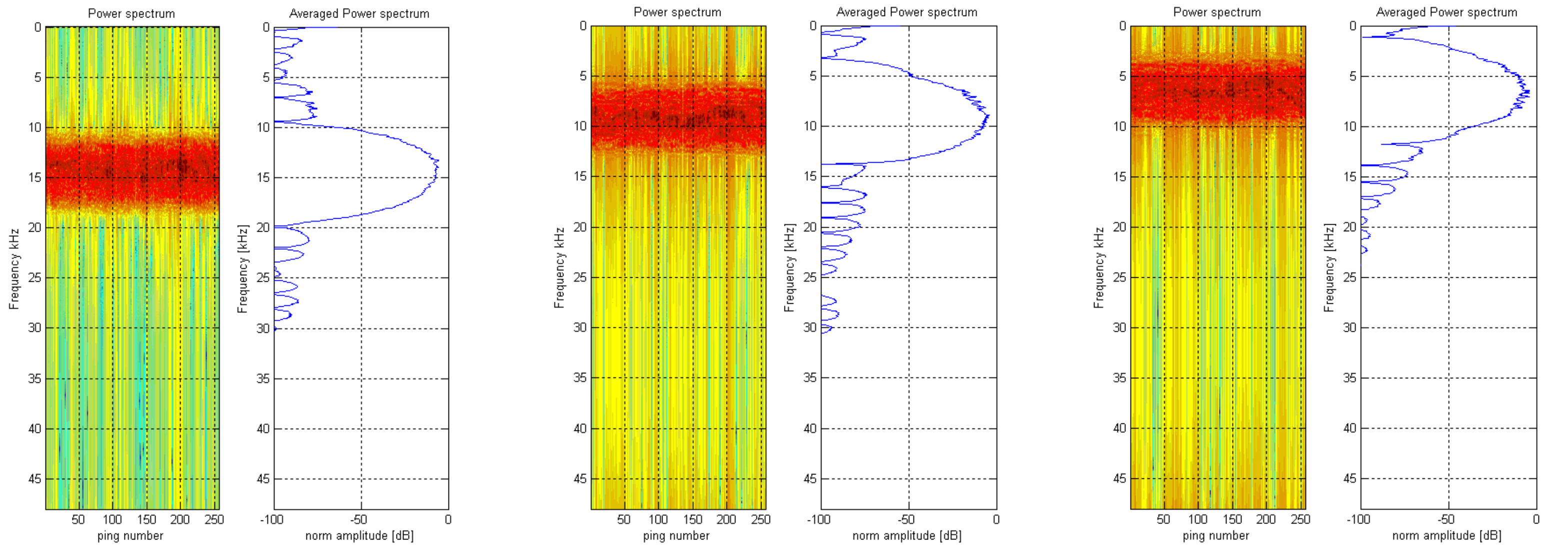

Figure 57:Power spectrum of the filtered dataset

5.2 Seabed surface classification using the energy model

As the transmitted acoustic signal travels downwards through the water column with a relative large beam width such as in the case of SBES, the received energy will be a composite of reflections and backscatters from the seabed surface. On the contrary, SBP operates with narrow beam width, where the received echo from a sub bottom profiler is dominated by reflections at sediment layers.

The observed signal amplitudes are a function of impedance contrast rather than interface micro roughness. This stems from the geometric measurement configuration; *'SBP sees only echoes that comes perpendicular from the sea bed with very narrow beam width'* [6], and also from the used low frequency band: '*the seabed amplitudes are much smaller than the transmitted wavelength'* [6]. As a result the backscatter is negligible compared to the coherent echo, since the microscale topography amplitude is much smaller compared to the signal wave length.

This distinct behavior is essential when modeling and interpreting data from the sub bottom profiler. With this concept the physics based model should pay attention to the energy transfer, losses, and reflections within sediment layers. The aim here is to infer the sediment type from its reflection coefficient by comparing it to the modeled reflection coefficient. The reflection coefficient of measurements starts by extracting the signals from recordings. Then their envelopes are squared and integrated to yield echo energies. The received echo energy E_{RX} at a given direction 'receiver interface' and pulse duration is related to the transmitted pulse E_{TX} through:

$$E_{RX} = \frac{e^{(-4\alpha H)}}{4H^2} R^2 E_{TX} \qquad (21)$$

where *H* denotes the distance between the echo sounder and the seafloor determined from the echo return time and the sound speed, and R is the reflection coefficient of the smooth surface. To discriminate between the energy loss due to transmission into the medium and attenuation associated with the traveled distance 2*H*, the energies are corrected for the spherical spreading factor $1/4H^2$ and the water absorption $e^{-4\alpha H}$ .Water absorption $e^{-4\alpha H}$ is the exponential form that computes the absorption rate proportional to water depth, where α is the water absorption coefficient estimated from Francois and Garrison formulas and converted to 1/m. From equation (21) the expression can now be inverted and the corresponding reflection coefficient of measurements can easily be estimated.

The next step is to estimate the modeled reflection coefficients that correspond to the assumed sediment types (-1ϕ till 9ϕ). The modeled reflection coefficient can be described via the classic Rayleigh reflection law which is a function of the impedance ratio between two mediums through equation 4.

Acoustic impedance Z is defined as the product of the sound speed and the density of a material. It basically represents the influence of a medium's characteristics on reflected and transmitted waves. Many geotechnical properties such as porosity, density, mean grain size, etc., exhibit excellent correlation with the impedance. Therefore, it is possible to predict the mean grain size from normal reflectivity data through the calculations of the sediment acoustic impedance.

Water impedance $Z_1(\rho_w c_w)$ can be roughly estimated by guessing the water sound velocity and density of water which might have different values from the true water column values. In the proposed model the sediment impedance is inferred from assumed sediment type 'i.e. impedance is a function mean grain size $Z_2(M_z)$ '. The mean grain size can be substituted by its geoacoustic properties described via Bachman's and Hamilton regression equations that relate the sediment velocity and density to the mean grain size through:

$$C_S = 1952 - 86.3 M_Z + 4.14 M_Z^2 \qquad (22)$$

$$\rho_S = 2380 - 172.5 M_Z + 6.89 M_Z^2 \qquad (23)$$

By combing equation (22) and (23), sediment impedance $Z_2(\rho_s c_s)$ can easily be estimated. One should note that although sediment impedance is uniquely identified as a function of the mean grain size, mean grain size as function of impedance $Mz(Z)$ gives various solutions.

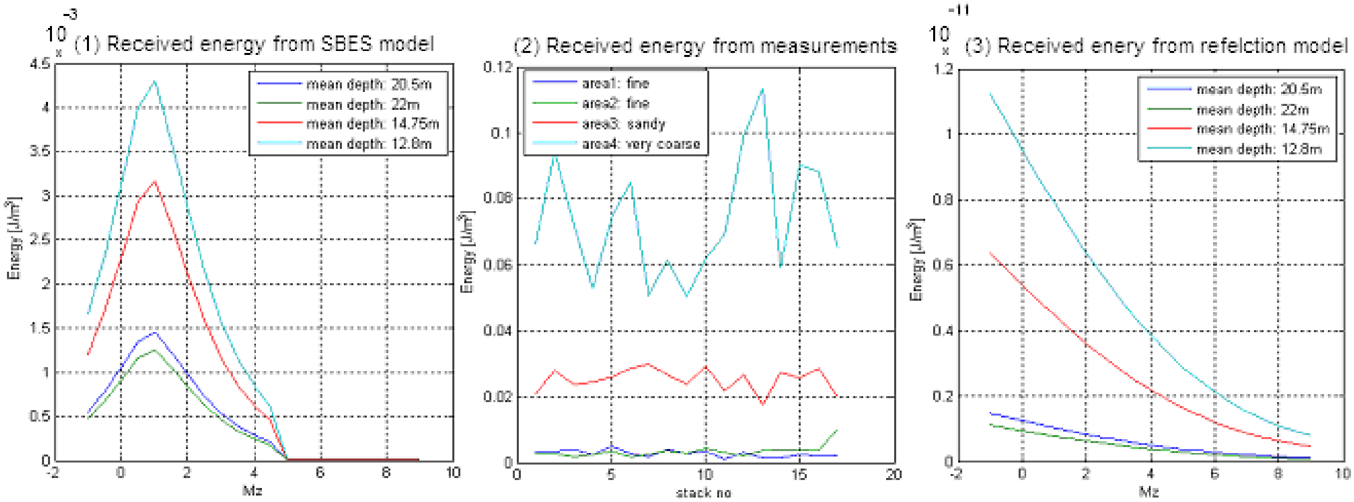

Figure 58: Echo energies observed and modeled

Prior to the reflection estimation, energy plots were compared first. The three plots of figure (58) represent the energy of the received echoes at four locations, with their corresponding depths estimated by its mean water columns (colored lines). The first plot illustrates the numerical integrated values of the echo envelopes at 100 kHz using the SBES time domain model. At the four areas, the energy curves increases gradually at -1<Mz<1 ‘rough sediments’. At 1<Mz<5 ‘sandy sediments’ the energy decreases almost with the same rate, while at Mz > 5 ‘fines sediments’ the decrement rate becomes much less. The decrement rate of fine sediments appears constant due to scale of the plot. The low energy decrement indicates that the modeled envelopes of the fine sediments have very similar characteristics. As a result, the plot is capable to distinguish between the predicted energies that correspond to the distinct sediment types ‘rough, medium and fine sediments’.

This distinct energy trend tends from the fact that reflections from rough sediments are dominated by surface reflections and very low contribution from the volume scatter. Reflection from coarse sediment i.e. 1<Mz<5, is a composite of both surficial and volume scatter. For fine sediments, the most dominating factor is volume scatter.

The second plot shows the energy of the recorded measurements at 100 kHz that belongs to the envelope of surface reflection ‘approximately two times the transmitted signal’. The plot shows a stable energy trend at the first three areas ‘area1, area2 and area3’ and less stability at ‘area4’. The fluctuating energy profile of ‘area4’ could be caused by surface inhomogeneities, or random roughness profile such as pebble and rocks. The third plot represents the predicted energy using equation (21).

By comparing plot (1) to plot (3), the distinct energy trend of plot (1) does not tend only from the different reflection process, but also from the transducer characteristics. Generally, if the receiving aperture angle was set to maximum, the transducer would be capable to record most of reflected energies (i.e. reflections backscattered energies) at larger grazing angles, and less information would be lost. Consequently, the energy profile of plot (1) would be closer to the energy profile of plot (3).

The energy of plot (3) drops monotonically from rough to fine sediments with much less energy values. This tends from that the equation (21) accounts only for surficial reflections without roughness or volume scattering consideration.

By comparing the colored lines of the second plot 'measurements' with the first plot 'SBES model', the four areas shows a clear correlation between the mean grain size and their corresponding energies. The comparison between the second plot and third plot 'predicted energy' shows a feasible correlation for the fines and sandy areas, whereas less correlation is observed for the pebble area. The low correlation is likely to occur due to the absence of the surface roughness parameter in equation (21) which might contribute greatly in echoes from rough sediments.

The comparison also shows that the vertical axes are different in scale due to realization of absolute values of the reflected energies. Thus, values of the reflection coefficient should be derived with the help of a few selected bottom grabs that serve to calibrate the energies for the entire data set. Since the true source levels are not available, the theoretical source level E_{TX} has to be scaled by an arbitrary value in order to estimate the absolute reflection coefficient.

Scale factor

Practically, determining the scale factor depends on prior knowledge of the sediment type using grab samples and a calibrated transducer where the exact transmitted energy in the water is well known. Since this information was not available, the scale factor determination will be derived from general description of the survey area which was moderately confirmed by the results of chapter 4. Stacking and trace alignment in chapter 4 resulted in 17 ensembles. A reasonable number of sub-ensembles were chosen from each area; basically 5 random ensembles per area resulting in four different calibration factors for each area. Each calibration factor will be used to the corresponding dataset to ensure proper reflection coefficients.

The numerical computation of the scale factor starts by assuming that the transmitted energy is subjected to an arbitrary scale factor C. Therefore, equation (21) can be rewritten as follows:

$$R = \frac{2CH}{e^{(-2\alpha H)}}\sqrt{E_{RX}} \qquad (24)$$

Where

$C = 1 / \sqrt{E_{TX}}$.

With the prior knowledge of the general description of each area, the corresponding Rayleigh reflection coefficient at water-sediment surface can be determined using Hamilton and Bachman's equations (22 and 23). The N calibration samples are associated with averaged Mz that corresponds to its zones typically Mz = 9phi for fines (area 1), Mz = 8phi for (area 2), Mz = 3 phi for coarse (area3), and Mz = -0.5 phi for very coarse (area4).

The number of calibration factors C_i per area can now be computed by matching the acoustic reflection coefficient of equation (24) to the expected Rayleigh reflection coefficient equation (4). By taking the root mean square of the C_i of each area we end up with four calibration factors. The calibration factors of area1, 2 and 3 were very similar and slightly different at area4 which could be due the high stochastic behavior of rough surface. Nevertheless, the four calibration factor were averaged and used for the entire dataset.

Classification result

By exploiting the calibration factor, the reflection coefficients for the rest of the dataset can now easily be estimated as shown in figure (59). The figure shows the estimated reflection coefficient 'solid lines' overlapped with the theoretical reflection coefficient from Hamilton and Bachman's table. The reflection coefficient is deduced from the theoretical relationship between sediment impedances and soil interpretation 'i.e. clay, silts, sand, etc' description. The black dots show the random calibration samples that were chosen during the estimation process. In general, there is good consistency but not for area4, which might be due to the fact that the roughness is too high to be neglected and due to the averaged scale factor that has been used. In [41], high resolution seismic reflection the reflection coefficient can be affected significantly by scattering due to boundary surface roughness and proposed solution on how to account for surface backscatter.

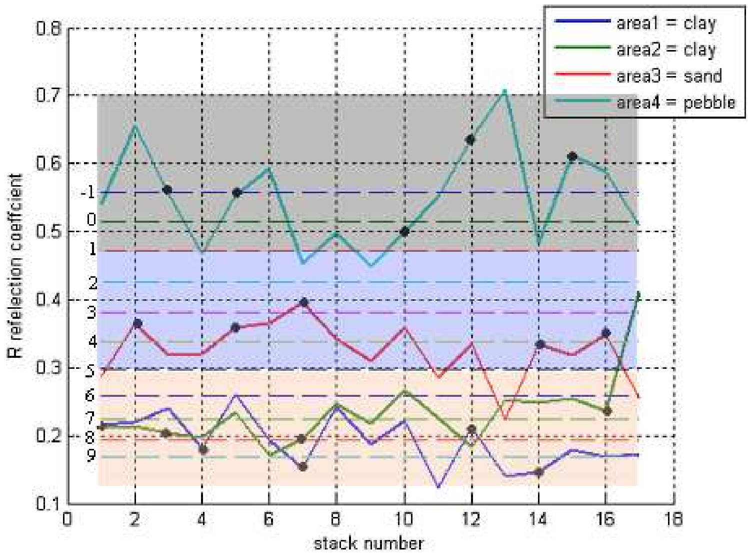

Figure 59: Reflection coefficient results using the 100 kHz dataset at the four areas. Horizontal dashed lines are the theoretical limits of the reflection coefficient which correspond to -1<Mz<9 phi.

Figure (60) depicts the equivalent sediment classification result 'Mz' in black solid lines overlaid with the classification results of chapter four 'solid cyan'. The figure shows the four areas in a sequential order for clearance. From the figure, both methods show similar results, with lower variations in the reflection based approach. However, to judge the quality of the results, larger dataset is needed to apply sufficient statistical evaluations.

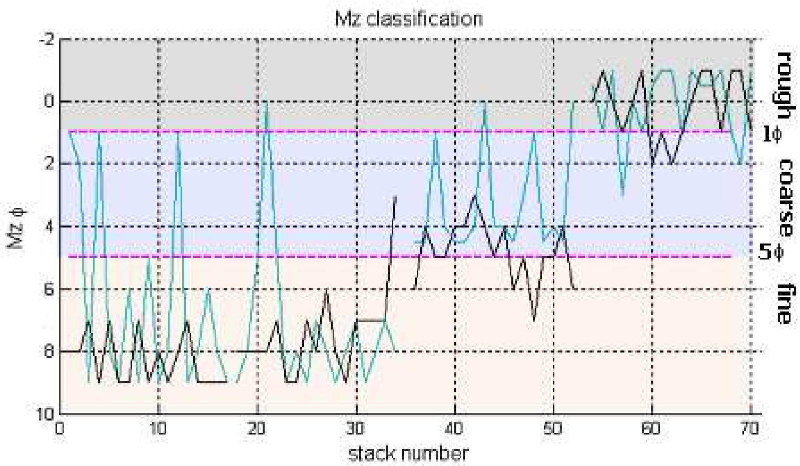

Figure 60: The high frequency classification results are displayed in black solid lines. The classification results of the SBES model are displayed in cyan solid lines. The sediment boundary limits between fine, coarse and rough sediments 'magenta dashed'. The four areas are presented in a sequential order from left to right, where area1 = stack (1-17), area2 = stack (18-35), area1 = stack (36-53), area1 = stack (54-72).

5.3. Sub bottom classification using energy model

In this section the low frequency echoes will be analyzed to infer the description of the sub bottom layers. Equation (21) does not account for layering interaction and describes only the received energy flux density as a result from seafloor surface reflection. With the low frequency, the received energies are reflected from the layered sediments giving more information about sediment layers structure and type. To model the received energy for such condition, expression (21) has to be extended to account for the additional physics processes by including layering absorptions, transmissions and reflections.

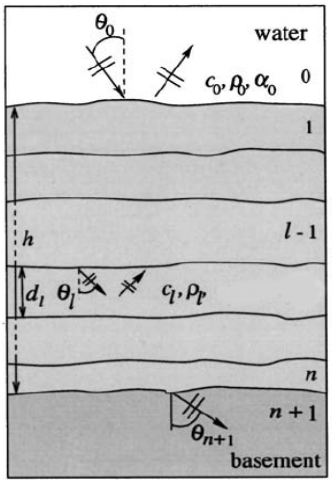

Figure 61: Theoretical sediment layer structure [28]

Consider a transmitted low frequency pulse emitted perpendicular towards a fluid dissipative sedimentary layer of thickness *h* and split into *n* elementary layers as in figure (61). Each layer *l* is characterized by its sound speed c_l , density ρ_l , attenuation coefficient α_l , and thickness d_l. The signal encounters an initial reflection at water-sediment interface that is influenced by losses due to spherical spread and absorption in the water column. The remaining energy will penetrate inside the sediment layer with a transmission coefficient of T_{ws_1} . The transmitted sound will be subjected to a secondary spherical loss limited to the layer thickness d_1 and its corresponding sediment absorption. The absorption coefficient of the upper layer can be inferred from table (6); the estimated reflection coefficient of the first step is used to search for the equivalent sediment type in table (6). Now as the sediment type is known, its corresponding absorption coefficient can be used for the computation of the next layer.

The absorption coefficient sound wave in marine sediments in table (6) is described through:

$$\alpha = kf^n \qquad (25)$$

Where:

k = constant that depends on sediment type

f = transmitted frequency

n = exponent of frequency dependence

Most authors support linear frequency dependent attenuation which is also followed in this literature by using Hamilton and Bachman's absorption values shown in table (6). There is a variety of sediment absorption units that are commonly used in the underwater acoustics and marine seismology communities. Most common is the decibel per unit meter, or decibel per wave length depending on the used propagation model. In table (6) the acoustic attenuation α_l is expressed in decibel per wavelength so it can be used with any frequency. In the used model, the attenuation coefficient was converted to dB/m to agree with the units of the extended equation.

Table 6: Sediment absorption coefficients after Hamilton & Bachman et al [6].

Sediment type	Mz (ϕ)	ρ (kg/m^3)	c (m/s)	α (dB/λ)
Clay	9	1.200	1.470	0.08
Silty clay	8	1.300	1.485	0.10
Clayey silt	7	1.500	1.515	0.15
Sand-silt-clay	6	1.600	1.560	0.20
Sand-silt	5	1.700	1.605	1.00
Silty sand	4	1.800	1.650	1.10
Very fine sand	3	1.900	1.680	1.00
Fine sand	2	1.950	1.725	0.80
Coarse sand	1	2.000	1.800	0.90

The mentioned attenuation process will continue until the signal encounters the second layer, where high impedance contrast exists. On the traveling way back to the receiver, the reflected energy is subjected to the same attenuation process during the transmission mechanism. The penetrated energy into the second layer will encounter the same physical processes until the energy vanish or is completely reflected by a rocky layer. The mathematical description of the mentioned process for one layer (i.e. second medium interface) is described through:

$$E_{RX} = E_{TX}\left(\frac{e^{(-4\propto_w H)}}{4H^2}\right)T_{ws1}^2\left(\frac{e^{(-4\propto_{s1} d_1)}}{4{d_1}^2}\right)R_{s1s2}^2 T_{sw1}^2 \qquad (26)$$

Where α_{s_1} the acoustic attenuation due to sediment absorption at the first is layer, d_1 is the thickness of the first layer, and $T_{ws1} = 1 + R_{ws1}$ is the transmitted energy coefficient from the water-sediment interface. The reflection coefficient at the boundary of the first and second layer is denoted by R_{s1s2} , and $T_{s1w} = T_{ws1}$ is the transmitted energy coefficient at sediment-water interface. The number of required parameters in the general expression depends on the number of layers (N). Table (7) shows the required number of parameters in order to compute the reflection coefficient at the corresponding layer.

Table 7: Required variables to be estimated for nth layer

Parameter	Number of required parameters
E_{TX}	1
Attenuation	N+1
Transmission coefficient	2N

Although, the incident wave can potentially excite both pressure and shear waves. The shear wave is neglected because we have almost vertical incidence and no solids. No solids mean that the seabed is modeled as fluid which means that it supports only compression waves. Shear waves should be taken into account when a reasonably solid bottom exists such as in ocean basement or situation where no soft sediments overlie the basement. When the reflecting medium is solid, the seabed should be treated as an elastic medium that provides a restoring force to recover from shearing. In this case, the incident wave will potentially be decomposed into pressure and shear waves.

Another external process that was neglected in this model is signal interference. Signal interference is the process in which two or more coherent waves combine to form a resultant wave in which the displacement at any point is the vector sum of the displacements of the individual waves. This might occur when a reflected signal is trapped between two layers 'i.e. delayed' and added to reflections that are encountered from deeper layers 'i.e. synchronized in time'. In this process, the received echo will be a component of amplitudes 'i.e. destructive and constructive' which will not represent the true sediment layer and consequently will degrade the reflection coefficient results.

Scale factor

In section (5.2), the scale factor was determined from the high frequency dataset. In theory, the source level of the high and low frequencies should be the same. This means that the estimated scale factor can be applied for the low frequency dataset. Practically, the source level of the low frequencies was not the same as the source level of the high frequency. Therefore, new calibration factor had to be estimated. The determination method is basically the same as introduced earlier in section (5.2). Contrary to the high frequency signals, the low frequency signal is much longer and contain reflections from sediment layers which means that the single trace is described by various sediments 'i.e. different grain size'. Therefore, the first received reflection encountered from the water-sediment interface was only used to determine the scale factor. This can be defined by selecting the envelope length equal to twice the transmitted pulse length starting from the water depth as shown in figure (62).

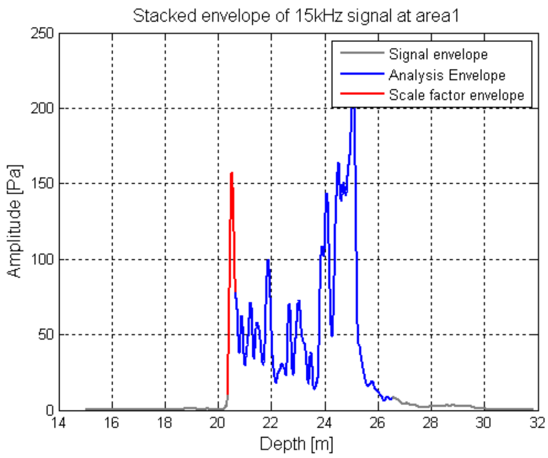

Figure 62: Envelope equal to twice transmitted pulse (red), selected to determine the scale factor

Figure (63) shows a comparison between the scale factor values and their corresponding distributions for each area. Five samples were selected located at the same position of the high frequency analysis that was shown earlier in figure (59). The figure shows that the scale factor of the first three areas are very similar, consistent and does not contain major errors such as observed with the scale factor of area4. The scale factor of area 4 implies that the selected five samples are highly variable due to non homogeneous pebble surface, or due to the additional backscatter area caused by the high surface roughness.

With the goal to find one scaling factor that works for the complete range of mean grain sizes and depths, one can basically use an average scale factor for the four areas. However, the averaged scale factor degraded the analysis results. Therefore, the first three scale factors were averaged resulting with a single scale factor used for the analysis of the first three areas. The scale factor of area4 was excluded and used only for its own area.

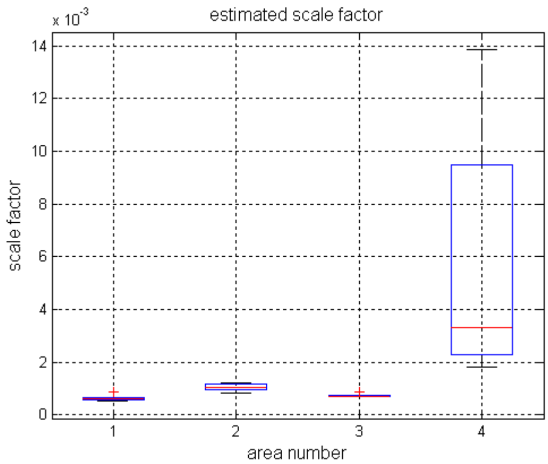

Figure 63: Contrary to the scale factors of the first three areas, significant variation can be seen in the scale factors of area 4. The upper and lower edge of the blue boxes shows the upper and lower quartile respectively. The red line is the mean.

Reflection calculation versus time

Figure (64) illustrates typical wave forms from a shallow sub-bottom record. With water depth travel time t_W and sampling window dt to calculate the acoustic reflection versus travel time are shown. The size of the sampling window is very crucial for the estimation of the local reflection coefficient. Basically too short sample window will not capture the correct energy that represent the desired local layer, while too large sample window will overestimate the reflection coefficient as it will overlap with the energy of the next layer. The principle of choosing the correct sample window will be investigated in the next section. For now, the size of the sample window is chosen to be once or twice the transmitted pulse length, which also agrees with the selection of the size in the following sections.

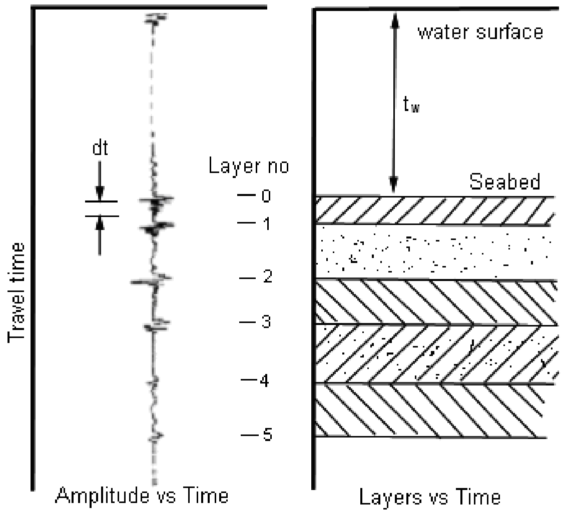

Figure 64: Physical reflection model [27]

As in deep seismic, all calculations can be done with respect to travel time. After sediment layers are defined and their corresponding velocities are known, the predictions can be corrected to reflections versus depth. Referring all procedures to travel time where the bottom echo starts after duration of t_w, the sequential data are derived into N subsections, $S(dt_1), S(dt_2), \ldots S(dt_n)$. The signal integration to each subsection of the sequential data can be calculated through:

$$E(t_n) = \sum_{t=t_1}^{t_2} (S(t))^2 . dt_i \qquad (27)$$

Where:

$$t_1 = t_w + \sum_{i=1}^{n-1} dt_n$$

$$t_2 = t_1 + dt_n$$

t_w = water depth travel time.

dt_n = sample window of nth subsection.

Sample window size

Calculating reflections coefficient versus depth is only valid when secondary reflections of the transmitted pulses are not located within the sampling window of the first arrival pulse. In order to evaluate this, a spectrum analysis method was applied on two sequential sample windows. The method is basically inferred from the broadly used approach 'spectral ratio method' to estimate sediment absorption coefficients within homogeneous layer [26], which is based on the analysis of the frequency content of propagated acoustic waves.

For a particular trace the spectra is calculated over a default window size of 200 μs , which corresponds to a 5 kHz bandwidth. A number of spectrum analyses have been performed on N times the sample size. The performed analysis is shown in figures (65, 66). The figures show the power spectrum of two sequential sample windows with different sizes 1, 2, and 4 times the pulse width. The hypothesis here is that if the spectrum of the second sample window is the same or less than the power spectrum of the first sample window then we are at the same sediment layer. In fact, the low power resulting from the second window is the sediment absorption influence on the transmitted signal within a homogeneous layer. On the other hand if the power spectrum of the second sample window is greater than the first one, this means that secondary reflection is encountered, which implies a presence of a secondary layer.

To avoid the presence of secondary reflections in the first sample window, one can choose a very short time window 'one time the pulse width'. However, a very short sample window in the time domain reduces the spectral resolution, and comparison becomes very difficult as shown in figure (66-A).

In the second plot figure (66-B) the sample window was set to two times the pulse width, which increased the spectral resolution and individual reflections were still separated. The difference between the maximum power spectrums is also larger which shows the influence of the absorption within the sediment layer.

Figure (66-C) shows the power spectrum of a sample window four times the pulse width. The figure shows that the individual sediment layer can no more be captured with the presence of secondary reflection within the single sample window. The power spectrum of the second sample window has larger amplitude over the entire frequency band, and no clear separation or difference can be observed at the maximum power spectrum as shown earlier in figure (66-b).

From the previous analysis, the best size of the sample window would be twice the pulse width and at least one time the pulse width for the minimum sample size as shown in figure (66-A). The figure shows a slight difference between the maximum power spectrums which is obvious as no major difference between the signal amplitude was yet encountered.

The influence of the sample size selection on the reflection coefficients versus depth is illustrated in figure (65). In figure (65-a), for a sample size equal to one time the band width, the reflection coefficients are consistent with the trend of the received signal. This behavior cannot be captured when the sample window was set to 4 times the band width as shown in figure (65-b).

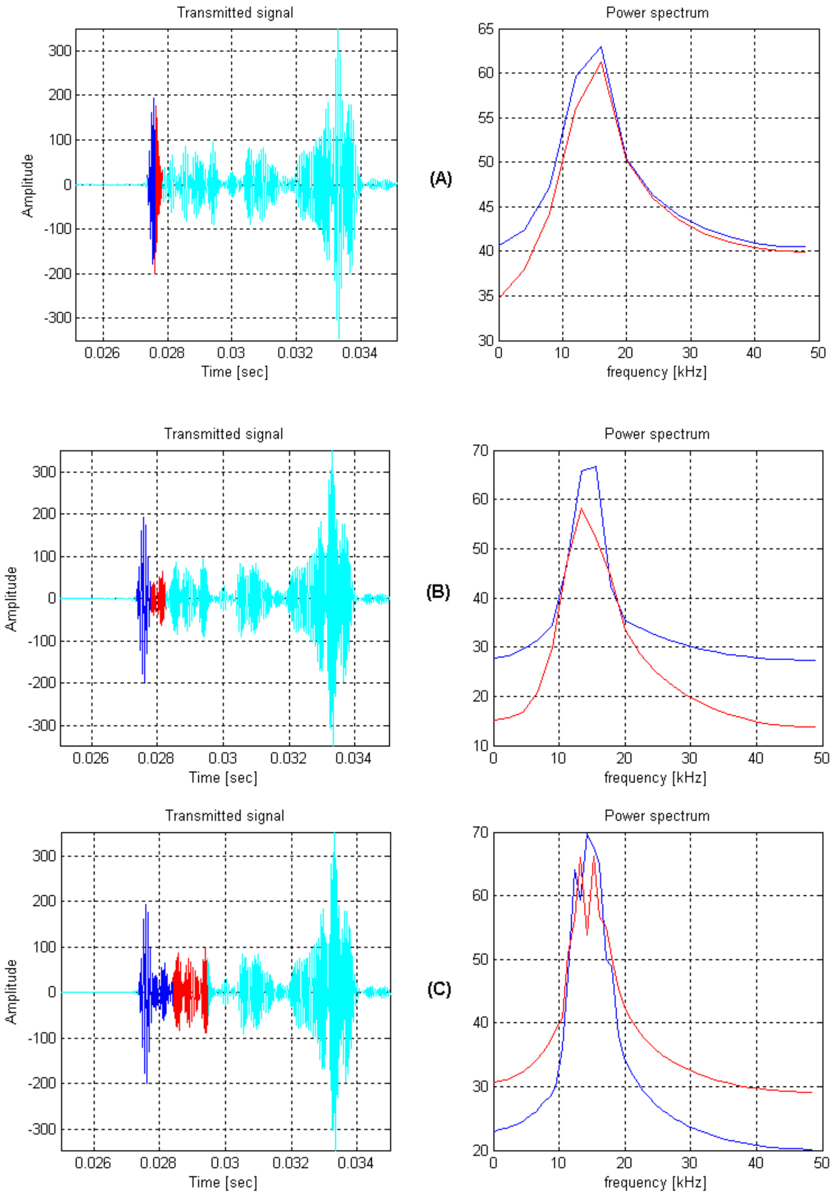

Figure 66: From top to bottom, sample size = 1 pulse width, 2 pulse width, and 4 times the pulse width. The blue and red lines correspond to the first and second sample.

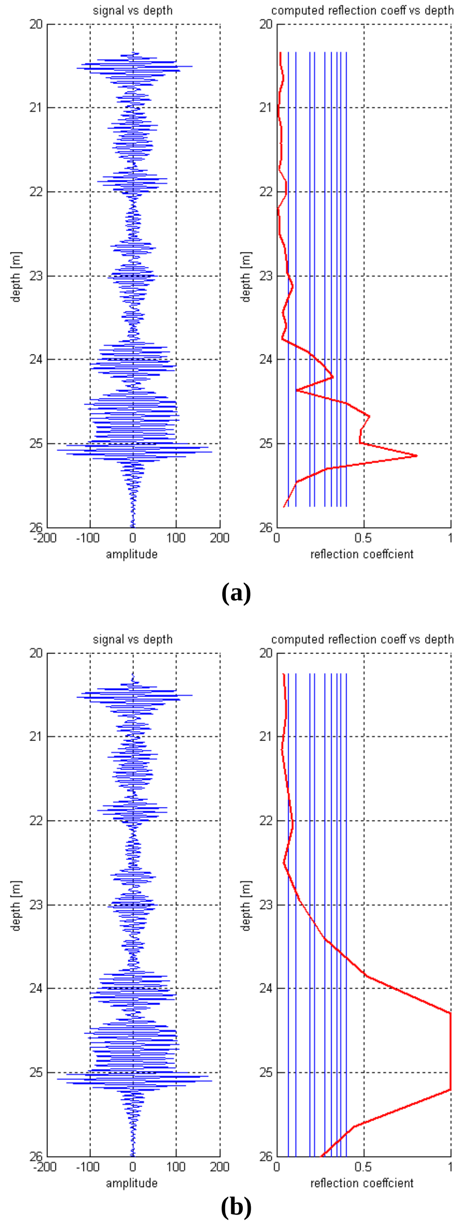

Figure 65: Comparison between sample size influences on the reflection coefficient estimates. (a) Sample window equal to one time the pulse width.(b) equal to 4 times the pulse width. The Left plot is the received signal (area1-15kHz). Right plot is the estimated reflection coefficient.

Classification result

The classification results started by a proper prediction of the sediment grain size at water-sediment interface that also agreed with the high frequency classification. However, the reflection results was acceptable for the first three or four iterations, but at deeper layers the predictions degraded drastically and unrealistic reflections were observed 'e.g. reflections >1' which cannot occur in the real physical process. This implies that there is an error that propagates and increases by increasing the number of iterations.

Theoretically, the reflection coefficient of sample window (n) depends on the geoacoustic properties of the sample window (n-1). If the reflection coefficient of (n-1) is wrongly estimated, the corresponding attenuations will be under or over estimated which will unbalance the energy ratios of (n). In our scenario, this can occur if the sample window covers several layers, in this case the reflection coefficient will be a rough estimate for the selected layers. In order to reduce the propagation error, the reflection coefficient has to be estimated at each layer boundary, by insuring that the layer boundary will fully fall into one sample window.

Figure (67) shows the echo envelope of a15 kHz signal. The envelope trace has various peaks and widths that correspond to the impedance contrast between two subsequent layers. Section (5.3) showed that sample window equal to twice the bandwidth is a feasible size to isolate the reflections between two subsequent layers. This can also be seen in the time domain of figure (67) where the first sample window sufficiently overlaps the first reflection from at water-sediment interface. On the other hand, sample windows 2, 3, 6 and 7 are poorly located, and do not represent a distinctive sediment layer. Consequently, the estimated reflections will not be accurate and misplaced.

For example, the reflection coefficient at the first sample window 'i.e. first layer' is well estimated and its corresponding absorption coefficient as well. In the following sample window, the window is too large and misses to estimate the reflection coefficient of a thin layer at point (c). In this case, the energy level is over estimated, and consequently the sediment attenuation as well. This will lead to unbalance the model and the corresponding reflection coefficient will be inaccurate. Consequently, the misclassification error will propagate within the model leading to unstable reflection profile. This will lead to decrease the size of the sample window to capture the missing thin layer, but unfortunately, this is not a practical solution for larger envelopes.

In order to compromise between the two requirements, the reflection coefficient will be estimated using the same sample window 'twice the transmitted pulse width' but with shorter intervals 'e.g. overlap 75%' to minimize the chance of missing intermediate layers. The red striped rectangles in figure (67) show the concept of overlapping windows.

The algorithm starts by a sample window width equal to twice the transmitted pulse duration. In figure (67), the first sample window intersects with the envelope at point (a). In the second iteration, the sample windows will shift 25% of the sample window and intersects with the signal envelope at point (b). The algorithm continues with the same shifting mechanism for N iterations, where the third, fourth and fifth iteration intersects with the signal envelope at point (c), (d) and (e) respectively.

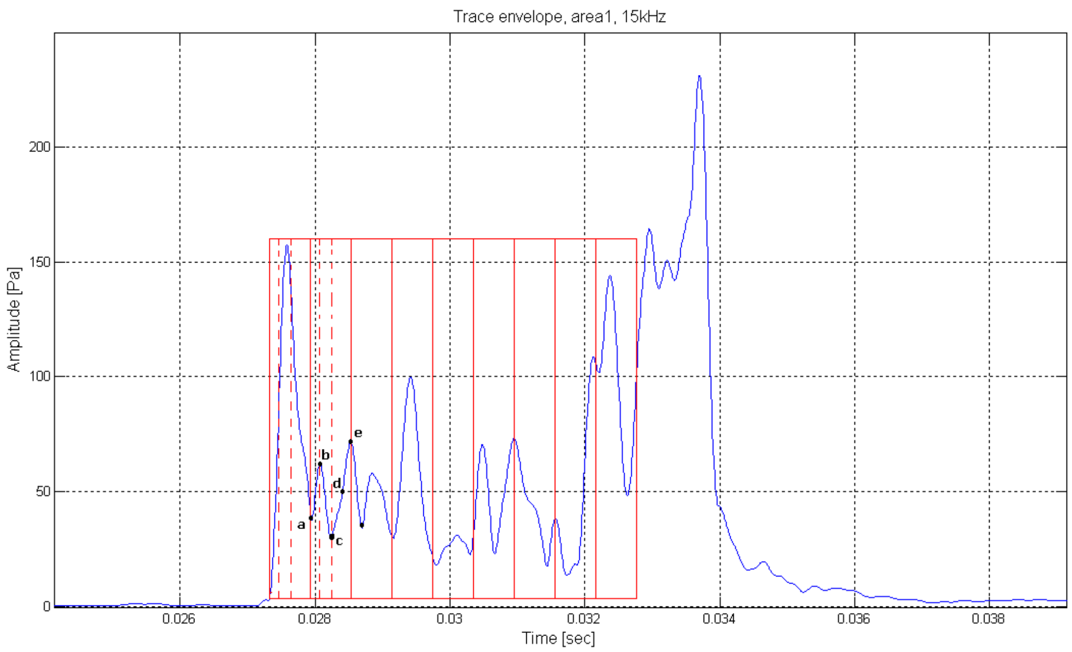

Figure 67: A descriptive plot that shows the sampling window techniques '0% & 75% overlap' plotted in red solid and dashed lines respectively. The blue solid presents the received echo envelope from a 15 kHz signal at area1.

Visually, one can observe that the first sample window covers a complete reflection envelope which was reflected from the water-sediment interface. Consequently, the estimated coefficient at point (a) is estimated with high confidence. In the second iteration, the sample window is shifted till point (b) which covers a large part of the envelope that was reflected from the water sediment interface and a part of the second envelope. In this step, the estimated reflection coefficient is estimated with less accuracy as the sample window does not fully cover the second envelope. This artifact might degrade the reflection estimates at point (b). The difference between the estimated reflection coefficient at point (b) and the true reflection coefficient is an error factor that will propagate within the model. However since we are using short intervals, the error magnitude is relatively small comparing to errors encountered by the algorithm with 0% overlap.

In the third step, the sample window covers the full reflection envelope at point (c), this is a major advantage as the algorithm ensures to cover intermediate layers which will be missed with the traditional 0% overlap window.

To illustrate the influence of the overlapping technique, a number of analyses were performed on different overlapping values 0%, 50% and 75% as shown in figure (68). The red lines presents 0% overlap ‘i.e. illogic results’, blue line represents 50% overlap, magenta (75% overlap) with significant improvement. One should note that too short intervals will degrade the results again by underestimating the reflection coefficients; sample window will not capture the full envelope of the second layer.

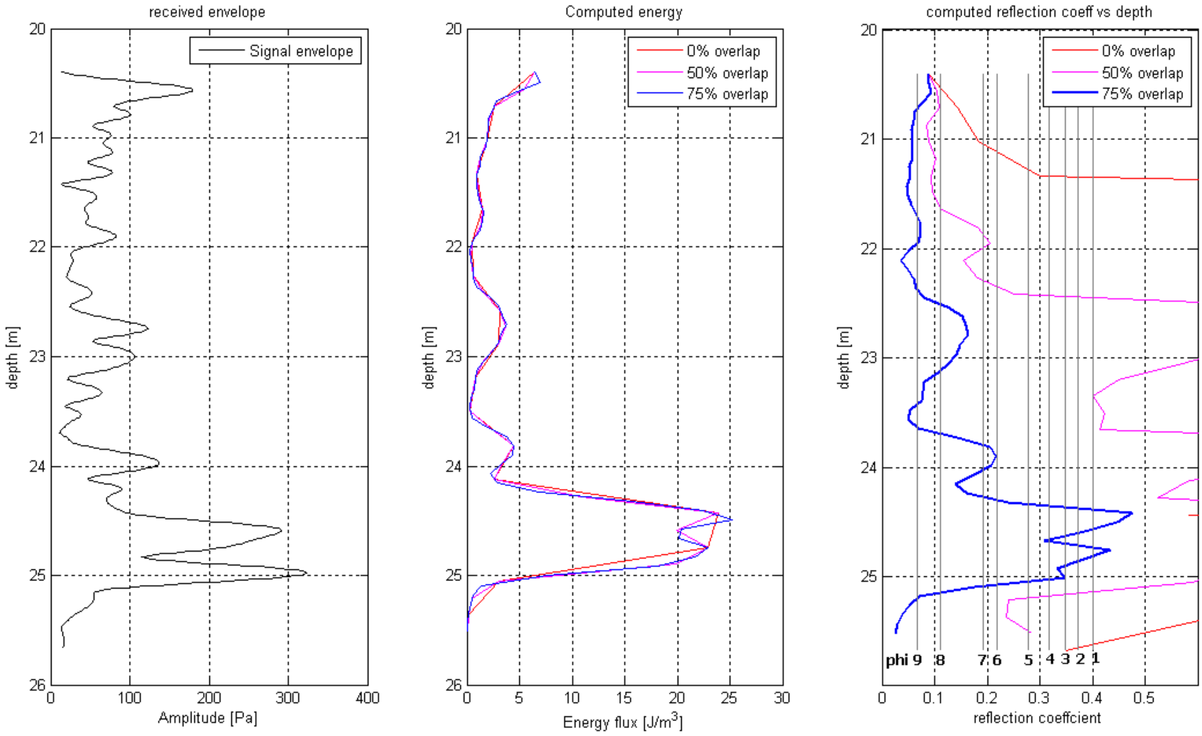

Figure 68: The estimated reflection coefficient trend with respect to travel time converted into depth. The left plot shows the received signal envelope from stacked dataset. The right plot shows the corresponding estimated reflection coefficients. The blue vertical lines represents from left to right, the theoretical reflection coefficients of mean grain sizes from 9 ϕ till (-1 ϕ).

5.4 Sub-bottom classification using Energy model (frequency domain)

In this method, the identification of the sub-layer bottom is achieved by following the work of [27]. The approach can be considered as a reverse algorithm of the previous method. In particular, the model compensates for the propagation and absorption losses in each layer as function of frequency. The total transmitted energy can then be estimated via the total sum of the compensated received energy. The reflection coefficients estimates at each sample window are consequently inferred by removing the losses in the layers above the desired one, so that the desired layer can be analyzed as if it were a surficial reflector. This concept is applied to each subsequent layer until recorded energy vanishes.

Reflection calculations versus depth

With the aim to compare the reflection coefficient estimates of the two methods, the sampling window was set the same as with the first method, which equal to the transmitted pulse width. The sampling windows are referred to the travel time where the bottom echo starts t_w as illustrated earlier in figure (64). Fourier transform is then applied on each sample window of the sequential data as shown in equation (28):

$$F(\omega_m, t_n) = \sum_{t=t_1}^{t_2} S(t) e^{-i\omega_m t} \qquad (28)$$

Where:

$t_1 = t_w + \sum_{i=1}^{n-1} dt_n$

$t_2 = t_1 + dt_n$

$S(t)$ = The sequential pressure envelope within sample window t

ω_m = The mth spectrum component

t_w = Water depth travel time

dt_n = Sample window of nth subsection

This operation will yield a sequential spectrum for each subsection presented in a matrix, which represents the spectrum components at each sample window. The energy matrix is then obtained numerically by integrating the squared spectrum components shown in equation (29).

$$E(\omega_m, dt_n) = \int [F(\omega_m, dt_n)]^2 \qquad (29)$$

The two dimensional Energy matrix is described through:

$$E = \begin{bmatrix} E(\omega_1, dt_1) & E(\omega_1, dt_2) & \ldots\ldots. & E(\omega_1, dt_n) \\ E(\omega_2, dt_1) & & & \vdots \\ \vdots & & & \vdots \\ E(\omega_m, dt_1) & \ldots\ldots & \ldots\ldots. & E(\omega_m, dt_n) \end{bmatrix} \qquad (30)$$

Yielding energy versus travel time dt_n and ω_n is nth spectrum components.

Losses

The compensation process for various losses is basically described by the same parameters as with the first approach, only the fact is that the losses are added in place of subtracted. The losses elements are summarized by:

- Geometrical spread to the desired layer

$$N_{spcorr} = 20\ \text{Log}(H) + 20\text{Log}(D_n) \qquad (31)$$

Where:

H = water depth
D_n = range from seabed surface to layer of interest

- Water attenuation

$$e^{(-4\alpha_w H)} \qquad (32)$$

Where:

α_w = water absorption coefficient

- Sediment attenuation

$$e^{\frac{\rho\omega_m}{BC}.D_n} \qquad (33)$$

Where:

C = Average Sound speed in sediment layer
ρ = Average density
B = 161.8 Dimensional constant viscosity.

The compensation procedure is computed in two steps. First the model accounts for the geometrical losses N_{spcorr} on the entire matrix elements as shown in the following equation:

$$E_{spcorr}(\omega_m, dt_n) = 10\log(E(\omega_m, dt_n)) + N_{specorr} \qquad (34)$$

After the geometrical loss correction, the absorption correction for water and sediment has to be applied for each frequency in the energy matrix as shown in equation (35):

$$E_{cor}(\omega_m, dt_n) = E_{spcorr}.e^{(-4\alpha_w H)}.e^{\frac{\rho\omega_m}{BC}.D_n} \qquad (35)$$

After the corrections have been applied per frequency, the total energy per sample window $E(dt_n)$ can be described by the summation of the total number of frequency samples as shown in equation (36):

$$E(dt_n) = \sum_{m=1}^{M} E(\omega_m, dt_n) \qquad (36)$$

Finally, the transmitted incident energy on the seabed is equal to the summation of energies at each layer plus energy losses which are energies that were attenuated, or penetrated and never returned back to the transducer. This can be described mathematically through equation (37):

$$E_{total} = k\sum_{n=1}^{N} E(dt_n) \qquad (37)$$

where the incident energy is the sum of the reflected energies times a constant k which represents the energy lost by reflection downward into the earth. k was numerically estimated earlier in the first method denoted by C in equation (24). As now the energy per layer and total energy incident is known, the reflection coefficient of the first layer is the ratio of the reflected energy 1st 'sample window' divided by the total energy of the signal trace:

$$R_1 = \sqrt{\frac{E(dt_1)}{E_{total}}} \qquad (38)$$

Reflection coefficients for deeper layers will be equal to the ratio of the energy from that layer divided by the total energy, minus the energy reflected from the previous layers:

$$R_n = \sqrt{\frac{E(dt_n)}{E_{total} - \sum_{m=1}^{n-1} E(dt_m)}} \qquad (39)$$

Classification result

Using the proposed method, figure (69) shows the estimated energy profile and the corresponding reflections for a particular trace. Contrary to the initial results of the first method 'energy model', the initial results 'i.e. 0% overlaps' of the second method 'energy model frequency domain' showed acceptable results. This is because the second method is not based on an iterative loop which is an advantage. For the sake of comparison, the overlap concept was applied. Consequently, the quality of reflection profile was improved by increasing the computation resolution ‘i.e. 75% overlapped sample window’.

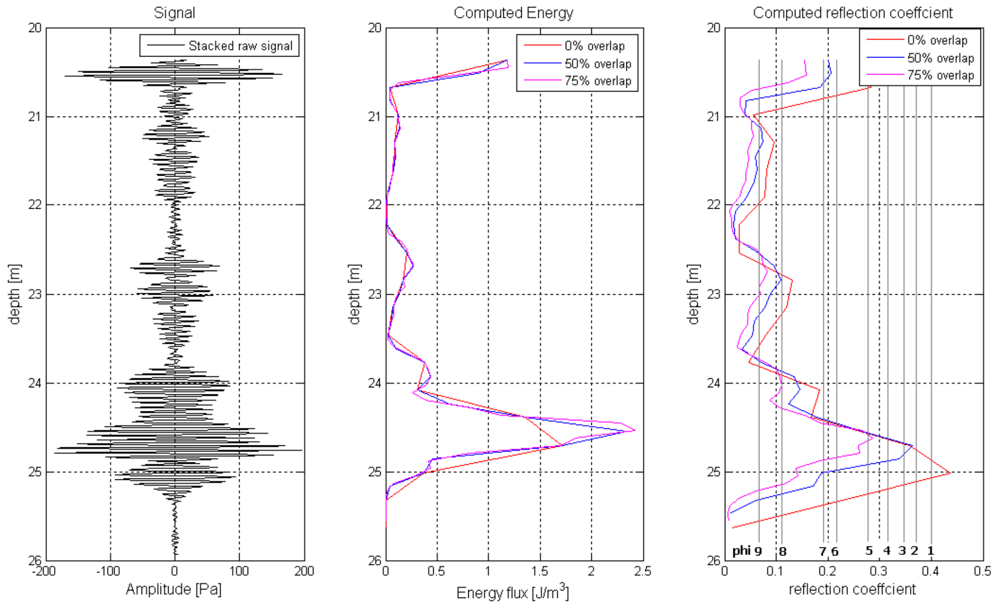

Figure 69: Comparison between overlapping concept using the second model. The left plot shows the stacked raw signal, middle plot illustrates the estimated energy for various overlapping interval, right plot illustrates the corresponding reflections.

5.5 Preliminary discussion of both methods

Figures (70-73) represent three arbitrary traces for each area. For each trace, three plots are presented; staking, energy and reflection comparison between the proposed methods. In general, the results of both methods agree with the general description of the four areas. Their reflection profiles are similar to a certain degree this basically depends on the model variables, errors, and propagation of error.

Since both methods infer the reflection coefficients via the energy ratios, their results are based on the corresponding energy profile. The energy profile depends mainly on the numerical integration of the stacked envelopes. Since each method had different procedure in estimating the required envelope, their energy profiles were slightly different. In this section we discuss the issues that concern the energy results and the corresponding reflectivity profiles:

- **Energy profile**

  In the first method the energy profile is estimated numerically by integrating the stacked envelopes of the raw signals in the time domain. Energies of the second method are estimated from the frequency domain where the staking process had to be applied on the raw signals rather than their envelopes. The stacking result of both methods is shown in the signal plots (70-73).

  Based on the principle of energy conservation, Parseval's Theorem states that the total energy computed in the time domain must equal the total energy computed in the frequency domain. This was not completely achievable due to errors in the stacking process of the second method. In order to achieve similar energies, the summation of the raw signals has to take the phases into account. This drawback shows that the energies estimated from the first method are more accurate since its stacking process is simpler and more robust. Additionally, difference in the energy computation can also be observed if the power spectrum has low resolution. In this case the numerical integration will give approximated values.

- Reflectivity profile

By investigating the reflection coefficient plots in figures (70-73), the blue lines 'reflection of second method' is slightly overestimated at the sediment surface and under estimated at deeper layer'. This trend implies as if it is an average estimate of the black line 'reflections from first method'. This behavior was theoretically expected since the attenuation in the second method is estimated via averaged sediment density and celerity, while in the first method the absorption is estimated sequentially for each sample window.

The raster plots of figure (74-77) shows a closer image of the raw reflected energies of the four areas which were shown earlier in figure (29). The reflection results of the two discussed approaches are plotted beside the raw measurements to compare the reflection contrast. The result of the first method shows the distinctive layers with better reflection contrast than those of the second method. This is because as mentioned earlier, that the reflection coefficient of the second method is an average estimate at the distinctive layers.

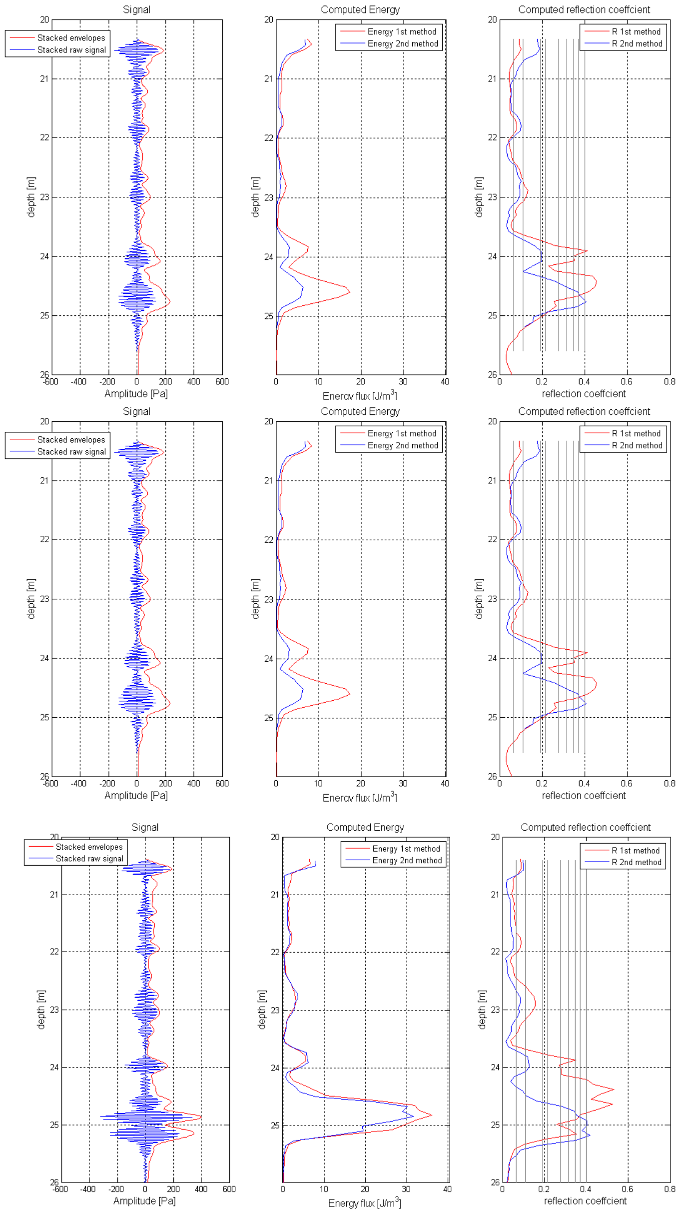

Figure 71: Estimated reflection coefficient for three arbitrary traces at area1, 15 kHz. Red lines are estimated reflection coefficient and energy using first method. Blue lines present the results from the second method

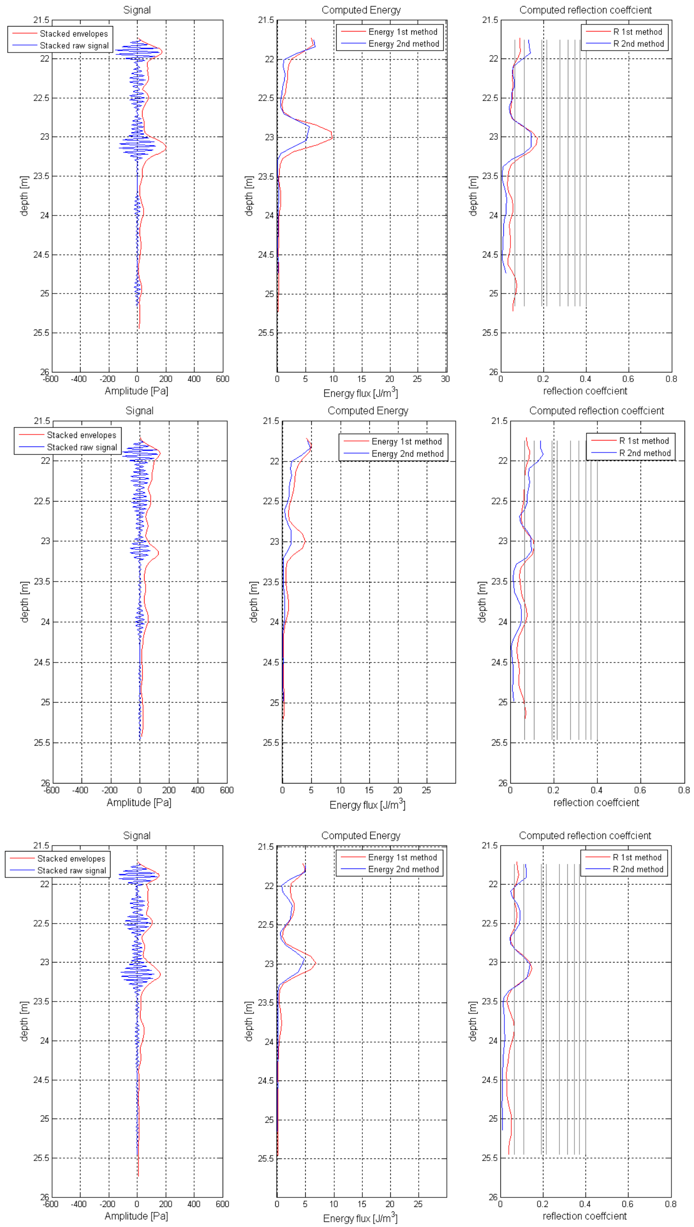

Figure 70: Estimated reflection coefficient for three arbitrary traces at area2, 15 kHz. Red lines are estimated reflection coefficient and energy using first method. Blue lines present the results from the second method

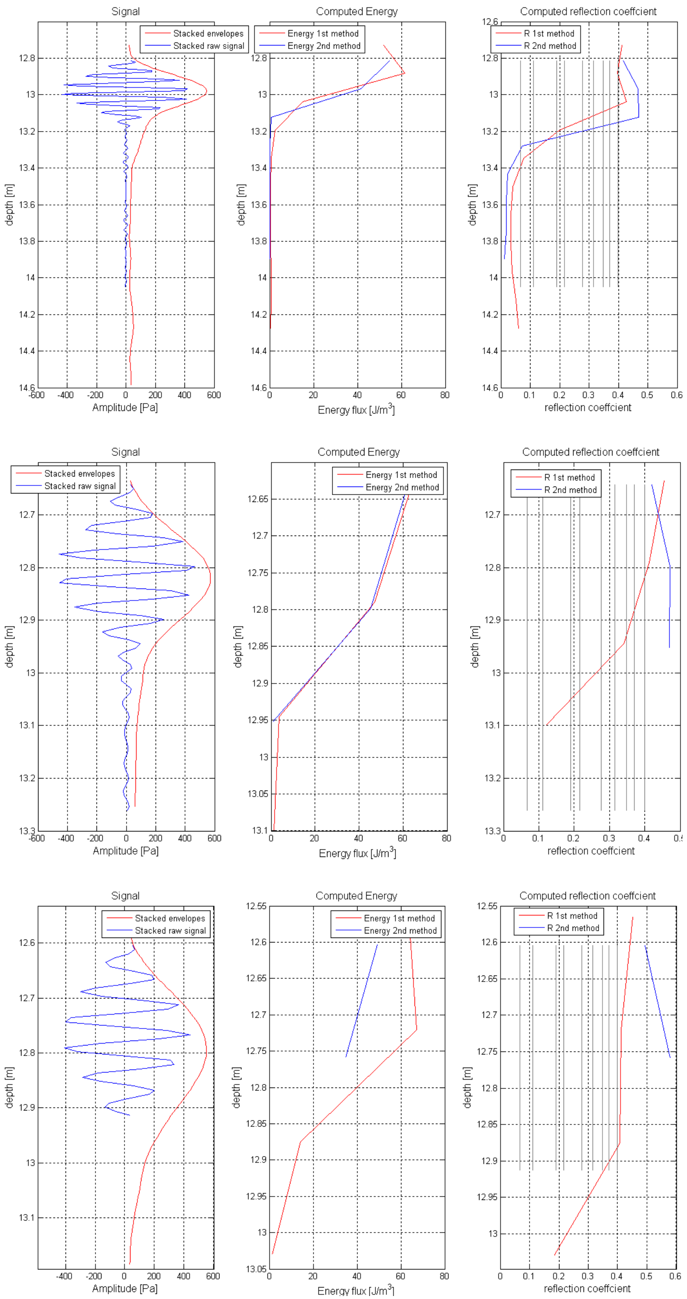

Figure 73: Estimated reflection coefficient for three arbitrary traces at area3, 15 kHz. Red lines are estimated reflection coefficient and energy using first method Blue lines present the results from the second method.

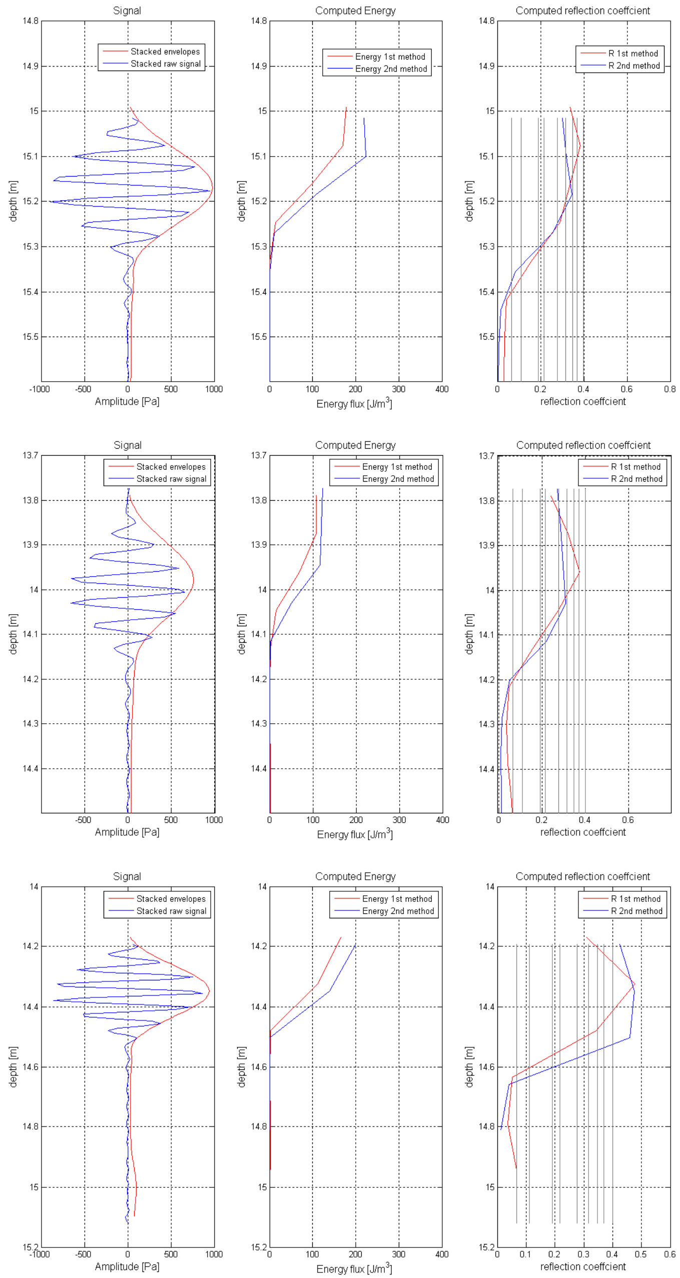

Figure 72**:** Estimated reflection coefficient for three arbitrary traces at area4, 15 kHz. Red lines are estimated reflection coefficient and energy using first method. Blue lines present the results from the second method.

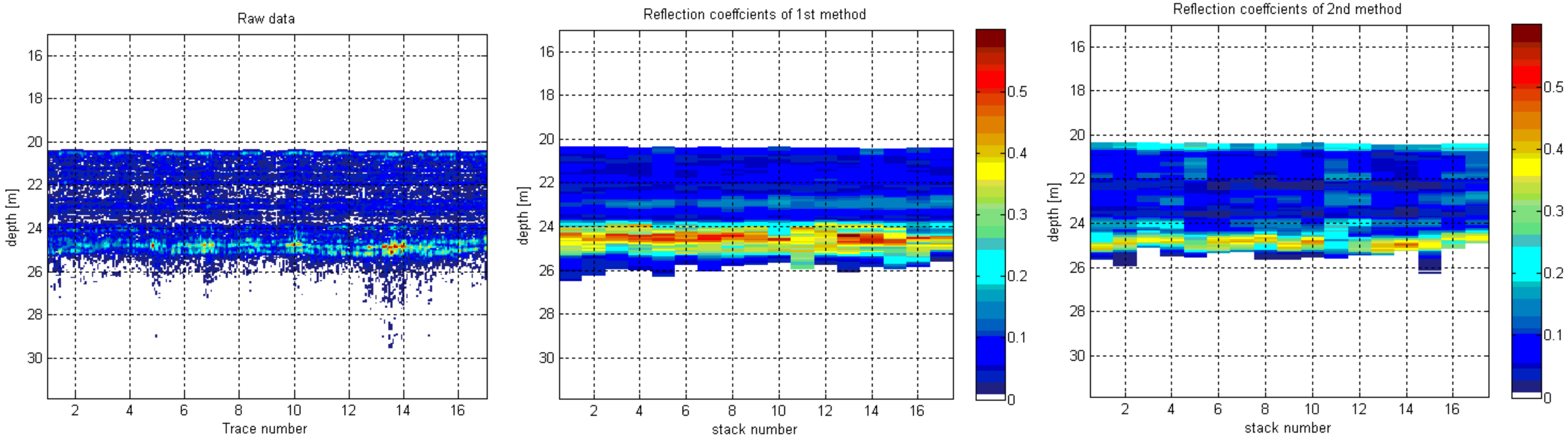

Figure (74): Raster plot of the predicted reflection coefficients of area 1 at 15 kHz

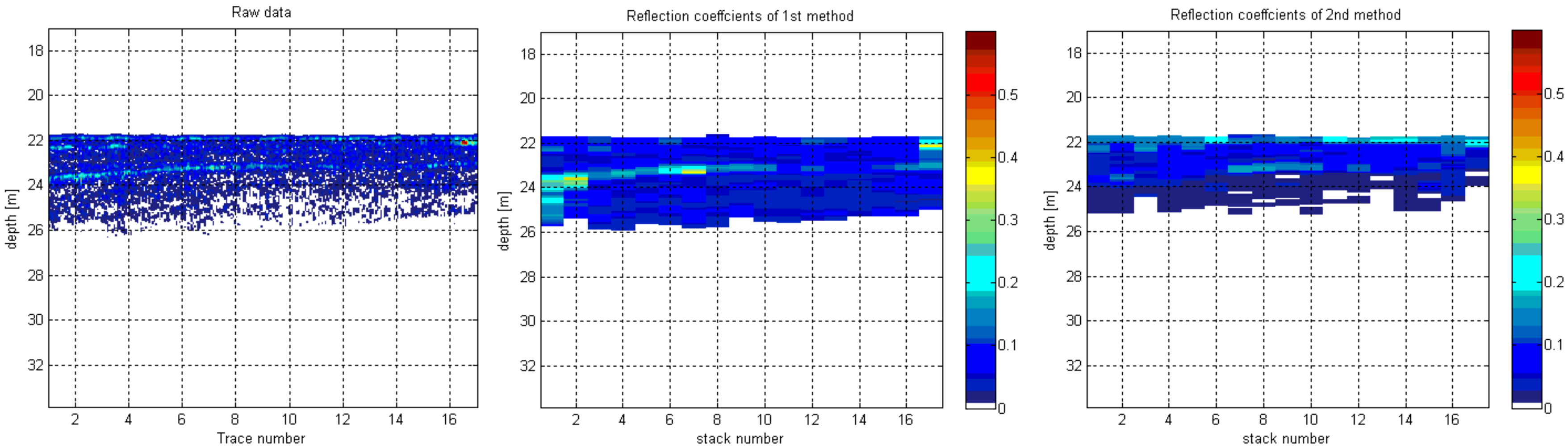

Figure (75): Raster plot of the predicted reflection coefficients of area 2 at 15 kHz

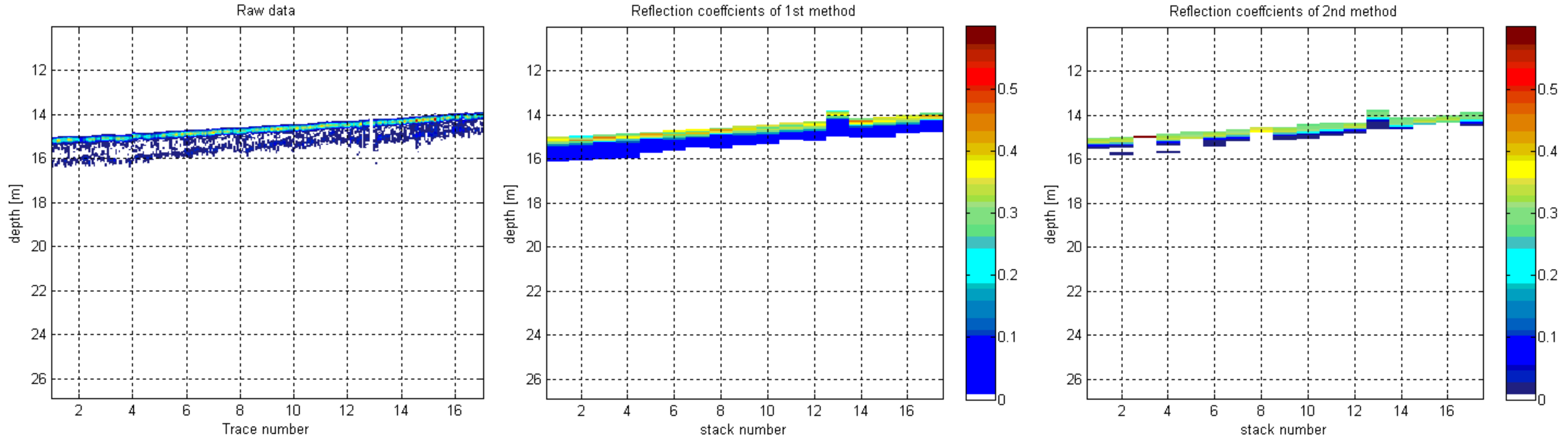

Figure (76): Raster plot of the predicted reflection coefficients of area 3 at 15 kHz

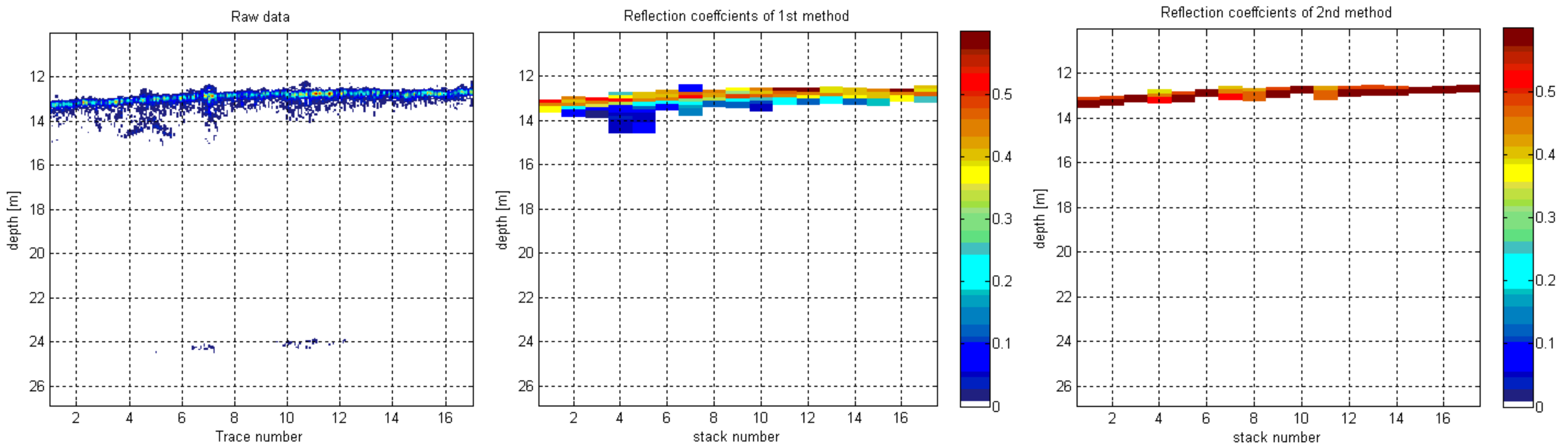

Figure (77): Raster plot of the predicted reflection coefficients of area 4 at 15 kHz

5.6 Preliminary discussion on the impact of biases on the reflection estimates

As mentioned earlier, one drawback of the first method is that the reflection is computed sequentially and the model parameters increase for every iteration. This means that the penetrated signal is subjected to higher component of attenuations. Figure (78) shows the model predictions of the received energies E_{rx} for various sediment types using Hamilton absorption coefficients. From the figure one can observe that water sediment layer the predicted energies have large thresholds, while at deeper layers the threshold becomes very narrow and becomes difficult to distinguish between the sediment types.

Another drawback was also the error component of over or underestimating the reflection coefficient or other phenomena such as 'interference and backscatters'. Although the error was greatly improved by the overlapping window technique some still remained. This error component is acceptable at layers near the surface and not at deeper layers and will have large influence on the prediction stability.

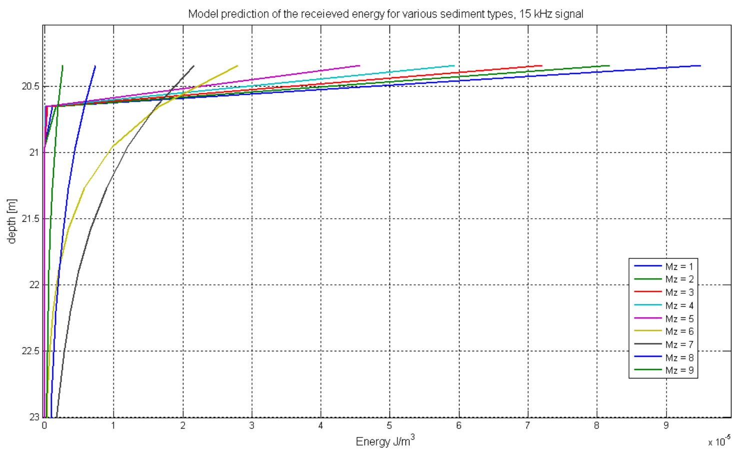

Figure 78: The figure shows the model predictions of the received energies E_{rx} for various sediment types using Hamilton absorption coefficients. For the rough and coarse sediments 1<Mz<5 the energies that are reflected from water sediment interface has larger magnitude than softer sediments. This is because the reflection coeffcient of coarse sediments are larger than soft sediments. At deeper layers , the received energies of the coearse sediments decrease drastically due to the high atenuation coeffcients.

Absorption coefficients

The initial absorption coefficient values of table (6) were no applicable at deep layers. Therefore, a temporary modification was applied on the absorption coefficients of the coarse sediments by values shown in figure (79). This solution increases the threshold limits between the different sediment types, and decreases the influence of errors on the reflection prediction. This solution was acceptable for area1 where the fine sediments overlaid coarse sediments. For area4 the water-sediment interface is composed of coarse sediments, which means that the modified absorption coefficients had to be rest back to their initial values.

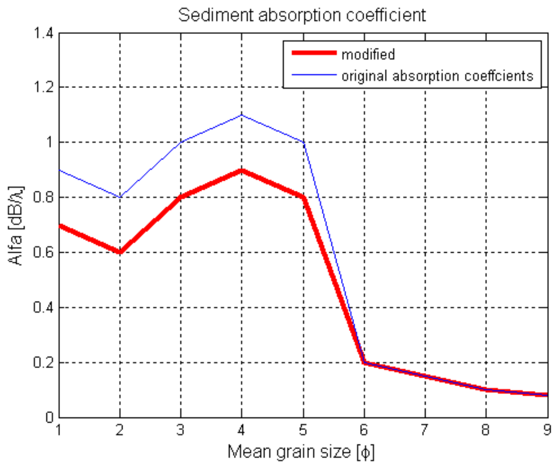

Figure 79: Modified absorption coefficients.

Interference

The SES-2000 parametric system has the capability of mapping the intrabed layers with high resolution. However, if the intrabed is composed of large number layers, the corresponding intrabed reflectors may generate interferences in the signal [43] causing attenuation losses [44] and may degrade the absorption coefficient estimates in both methods. Thus, to decrease the error component, signal interference must be utilized in the algorithm to evaluate the effect of intrabed reflections on the absorption estimates.

Chapter 6

Conclusions and future work

In this thesis, methods were presented for sediment classification using a high resolution sub bottom profiler. The classification was devoted to surficial and sub layers classification using high and low frequency dataset. This chapter gives the final conclusion and recommendations concerning the presented work.

6.1 Summary and Conclusions

A number of physics based models were implemented and tested to find out the capability of sediment classification using a parametric sub bottom profiler.

- High frequency observations

For the high frequency dataset, two physics based models were tested based on the signal shape 'SBES time domain model' and signal strength 'Reflectivity model'. The time dependent SBES model was basically implemented for an SBES transducer and modified to operate with signals from a parametric SBP 'SES-2000' system. Although, SBPs are technically designed for mapping sub layers structures, where the received echo contains little information about the sediment backscatter characteristics, the model classification results showed acceptable agreement with the general description of the surveyed area. However, these results are difficult to achieve and need human supervision as the raw data requires a considerable amount of signal processing before the classification procedure. Two signal processing aspects are crucial to achieve these results:

- The raw signal contains information about sediment characteristics but masked by noises such as reverberations, and ambient noise, etc. To alleviate the noise effect, the raw data has to pass through a band pass filter. To eliminate the noise effects as much as possible without changing the received echo shape, the band pass threshold can theoretically be set to the transmitted signal characteristics or analytically by determining the noise spectral cutoff limits.

- For a particular survey line, the received echoes vary in shape and amplitude. Their stochastic variation is relative to the sediment type 'e.g. soft sediments have low variation, and hard sediments have high variation'. Therefore, stacking and alignment techniques are essential to eliminate these variations. The analysis of chapter 4 showed that minimum threshold alignments are more practical with echoes that have low variations 'i.e. soft sediments', and peak or half peak thresholds are more practical with echoes that have a high degree of variation 'i.e. hard sediments'. Due to the system narrow beam width, the analysis of chapter 4, and supported by conclusion of [8], showed that deviation from these threshold values may drastically degrade the classification results.

The second model infers the sediment types by predicting the reflection coefficients of the received echoes. Reflectivity models are based on signal strength in place of shapes. The results showed good agreement without the complications of alignment techniques of the first model. However, the results of area 4 'rough surface' didn't have the same consistency and contained major fluctuations, which implies that 100Hz will not fulfill the assumption to neglect backscatter. In high resolution seismic reflection the reflection coefficient can be affected significantly by scattering due to boundary surface roughness [41]. One important aspect has to be considered to achieve these results:

- Since the source level is not known, a scale factor is needed to carry out the information of the received echo. The scaling was successfully done once for the first three areas. The forth scale factor 'i.e. area4' was excluded due its high variation.

- Low frequency observations

The low frequency signal ‘15, 10 and 5 kHz’ is much more complicated than the 100 kHz signal and cannot be predicted by the SBES model. The received echo can be described by a series of reflections at sub layer interfaces. Two energy based model was implemented that accounts for sound propagation into sediment layers. The first model infers the reflection coefficients sequentially from the time domain. The second model infers the reflection coefficients as if they were surficial sediments by compensating for absorption and other losses in each layer as function of frequency. In general, although no core samples were available to evaluate the results, the predicted reflections of the first model shows the distinctive layer boundaries similar to the original plots of the original dataset. The second model didn’t show distinct improvement which is likely due to the narrow bandwidth of the transmitted signal. The quality of the first model stems from the fact that the reflection coefficients are computed sequentially after estimating the geoacoustic parameters of the previous layer, while in the second method, the reflection coefficients are estimated from one assumed input; average geoacoustic parameters expected at the classification area.

The conclusions that can be drawn from the low frequency analysis are:

- The algorithm of the first reflection model is very sensitive to the presence of errors. The errors might appear from absorption factors that are deviated from the true value, or even misclassified layers. These errors are acceptable at the first couple of layers, and increases drastically by increasing the layer index. This issue is not a problem in the second model since reflection computations are not executed in a sequential order.

- Resolution is a crucial issue for the first model. If low resolution is used ‘i.e. large sample window’, the reflection predictions will be inaccurate, by missing intermediate layers. This inaccuracy will behave as an error which will propagate within the second iteration and will influence the reflection predictions of the following sample windows. Therefore, a proper sample window has to be chosen to capture the full reflected energy from the desired layer and without overlapping with secondary reflections.

- Overlapping sample window is an attractive approach to compromise between the required window size and desired resolution. The technique effectively enhanced the reflection results and the rate of the propagated errors.

- Theoretically, the first model cannot be used for deep layers, due to its attenuation extremes that increase by increasing the number of iterations. Basically, the amount of energy reflected from different sediment types at deep layers becomes very small, and cannot be distinguished.

- The assumption of [27] that the total energy 'i.e. received energy' equals the received energy is not correct. This is because some of the energy will penetrate and never return back to the transducer. Therefore the scale factor is important for the implemented method as well.

6.2 Recommendations

SBES model (High frequency)

It can be concluded that energy models (i.e. models that estimates the sediment type via energy ratios) using high frequency signals are simpler than SBES models (i.e. models that estimates the sediment type via matching the modeled and measured envelopes). The difficulties of using the SBES model, tends from transducer narrow opening angle, which means that a large part of information (i.e. reflections and backscatters) are lost. Consequently, the envelope shapes that correspond to the various sediment types will not be distinctive enough to distinguish between their types.

However the SBES model can be improved in three ways:

- The modeled signal assumes that the transmitted signal is a Gaussian shape which is considered a rough estimate of the true nonlinear pulse shape. The true pulse shape in this case is the nonlinear pulse that interacts at water sediment interface. Implementing the true signal shape will influence the energy distribution of the received echo, and better matches can be achieved.

- Second, the true source level can be included in the model to eliminate the need of scale factor. This can be achieved by calibrating the transducer in order to gain information about the true source level for each frequency during the survey operation. This aspect is also important for the energy model as well.

- In cases where the shape matching is difficult, one could test to match signal features in place of signal shapes such as signal amplitudes, signal duration, etc. These parameters will be less affected by the external noises and might be more efficient in the matching procedure.

Energy model (High frequency)

The energy model showed acceptable results for surficial classification except for area 4. Theoretically, the reflected energies from the seabed are a composite of reflections and scattering processes. Their influence contributes to the total received energy and cannot be separated practically. The energy models that were implemented in chapter 5 did not account for the backscatter process, which means, that their prediction will be sufficient only at areas where sediment types are dominated by reflections (e.g. mud, clay, sand) rather than backscatters such as with area 1,2 and 3. In order to achieve better results at area 4, it is recommended to include the influence of the backscatter process, so the received energies can be correctly compensated.

Energy model (Low frequency)

The result of the low frequency analysis leads to the awareness that the used models are not perfect. From the theoretical and practical investigations of this project, the sub-bottom reflectivity model can be significantly improved in the following areas:

- Reflectivity model: the results in chapter 5 showed that the iterative algorithm was highly influenced by the appearance of errors and their propagation. These errors can be described by the transducer accuracy and physical processes that were not accounted within the model. Therefore, the implemented model needs to be completed in the area of errors in practical situations and additional physical processes such as signal interferences and backscatters.

- Reflectivity algorithms: In order to eliminate the error propagation of the first model, the algorithm has to insure to limit its iteration to a specific error ratio.

- Conversions to mean grain size have to be done iteratively because both methods give the reflection coefficient between two subsequent sediment layers.

Bibliography

[1] Schlaginweit, G., **‘Real time acoustic bottom classification for Hydrography: a field evaluation of RoxAnn’**. Proc.Oceans ’93,vol3,pp,214-219,1993.

[2]. **Modeling acoustic backscatter from near-normal incidence echo sounders- sensitivity analysis of the Jackson model** P.J.Mulhearn.

[3]. **Acoustic seabed classification of marine physical and biological landscapes** ICES. 2007 ISBN 87-7482-058-3 ISSN 1017-6195.

[4]. **University of Washington APL model**

[5]. “**High-frequency sonar equation models for bottom backscatter and forward loss”, (1989), iEEE Oceans.** P. D. Mourad and D. R. Jackson,

[6] **An introduction to underwater acoustics**. Xvier Lurton

[7] William T. Collins and Karl P. **Rhynas ‘Acoustic Seabed Classification using Echo Sounders: Operational Considerations and Strategies’.**

[8]. **Time-dependent seafloor acoustic backscatter (10-100 kHz),** STERNLICHT Daniel D. ; DE MOUSTIER Christian P.

[9]. **Modeling acoustic backscatter from near-normal incidence echo sounders- sensitivity analysis of the Jackson model** P.J.Mulhearn.

[10]. **Fundamental of acoustical oceanography**. Herman Medwin and Clarence S.Clay

[11**] Mean grain size mapping with single-beam echo sounders** van Walree, Paul A.; Ainslie, Michael A.; Simons, Dick G.The Journal of the Acoustical Society of America, vol. 120, issue 5, p. 2555

[12]. **Sediment Classification Based on Repetitive Multibeam Bathymetry Surveys of an Offshore Disposal Site.** Preston, J.M., Parrott, D.R. and Collins, W.T. **2003-4**

[13]. “**Wave reflection from a transitional layer between the seawater and the bottom**”, R. Carbo, J.Acoust.Soc.Am., 101, 227–232, 1997

[14]. **Acoustical Identification of Sea-Mines (A Coherent Very High Frequency Sonar Model).** Gorm Wendelboe.

[15]. **Acoustic sensing techniques for the shallow water environment. Inversion methods and experiments (pp. 265-279).**

[16] C. de Moustier and D Alexandrou**."Angular dependence of 12 kHz seafloor acoustic backscatter,"**, *J Acoust Soc. Amer* , vol 90, pp 533-541,1991.

[17] Bishwajit Chakraborty and Vijay Kodagali, **“Characterizing biogenous sediments using multibeam echo sounder backscatter data – estimating power law parameter utilizing various models”.**

[18] H. Medwin. and C.S. Clay, **Fundamentals of Acoustical Oceanography**, New York, USA :*Academic Press. 1998.*

[19] K.B. Briggs, A.P. Lyons, E. Pouliquen, L.A. Mayer, and M.D. Richardson**, "Seafloor roughness, sediment grain size and temporal variability, in *Underwater Acoustic Measurements: technologies and results*"**, Heraklion, Crete, Greece, pp. 29-37, 2005.

[20] C. G. Fox and D. E. Hayes, **Quantitative methods for analyzing the roughness of the seafloor**, *Reviews of Geophysics,* 23(1), pp. 1-48, 1985.

[21] G. R. Cutter, Jr, and R. J. Diaz," **Biological alteration of physically structured flood deposits on the Eel margin, northern California"**, *Contin. ShelfRes.,* 20(3), pp.235-253, 2000.

[22] C.k.Wnetworth , **"A scale of grade and class for elastic sediments "** J.Geology, vol. 30 .p3777,1922.

[23]. JENSERUD Trond , FFIBM, NO, SIMONS Dick, TNO-FEL, NL ,CRISTOL Xavier **''FFI rapport rumble project scattering index models''**

[24] K.V. Mackenzie. Bottom reverberation for 530 and 1030 cps sound in deep water. *Journal of the Acoustical Society of America,* 33:1498–1504, November 1961.

[25] **High-resolution sub-bottom profiling using parametric acoustics,** J. Wunderlich, G. Wendt and S. Müller.

[26]**. High-Resolution Geoacoustic Characterization of the Seafloor Using a Subbottom Profiler in the Gulf of Lion**. *G. Theuillon, Y. Stéphan, and A. Pacault*

[27]. **Prediction of shallow sub-bottom sediment acoustic impedance while estimating absorption and other losses**. *Journal of the Canadian society of exploration geophysics. D.D.Caulfield and Yung-Chang Yim.*

[28]. **Backscattering from buried sediment layers: The equivalent input backscattering strength model**
Guillon, Laurent; Lurton, Xavier The Journal of the Acoustical Society of America, Volume 109, Issue 1, January 2001, pp.122-132

[29]. The Oxford science study dictionary, Oxford University Press, 1999

[30]. Guenther, G.C., Cunningham, A.G., LaRocque, P.E., & Reid, D.J. (2000). **Meeting the accuracychallenge in airborne Lidar bathymetry**. Proceedings of EARSeL-SIG-Workshop LIDAR, No. 1.Dresden, Germany.

[31]. Courtney, R., Anderson, J.T., Lang, C., & Fader, G. (2005). **Comparative seabed classification using sidescan and normal incidence sonar data at selected study sites on the Scotian shelf, Canada**. Proceedings of the International Conference "Underwater Acoustic Measurements:Technologies & Results". Crete, Greece.

[32]. Anderson, J.T., Van Holliday, D., Kloser, R., Reid, D.G., Simard, Y. (2008). **Acoustic seabed classification: current practice and future directions**. ICES Journal of Marine Science, 65, 1004-1011.

[33]. McQuillin, R., Bacon, M., and Barclay, W. (1984). **An introduction to seismic interpretation: reflection seismics in petroleum exploration**, 2 nd Ed. Graham & Trotman Ltd., London

[34]. Claerbout, J. F., 1976. **Fundamentals of Geophysical Processing**. New York: McGrawHill.

[35]Stoker, M.S., Pheasant, J.B., Josenhans, H. (1997). "**Seismic methods and interpretation**." In T.A. Davies, T. Bell, A.K. Cooper, H. Josenhans, L. Polyak, A. Solheim, M.S. Stoker, J.A. Stravers (Eds.), *Glaciated Continental Margins: An Atlas of Acoustic Images*. Chapman and Hall, London, 1997. 315 pp.

[36] D.Simons, M.Snellen Lecture notes TUDelft **introduction to acoustic remote sensing**.

[37] Legendre, P., and L. Legendre, 1998. Numerical Ecology. Elsevier: Amsterdam, 853 p.

[38] Legendre, P., Ellingsen, K.E., Bjornbom, E., and Casgrain, P. 2002. **Acoustic seabed classification: improved statistical method**. Can. J. Fish. Aquat. Sci. 59: 1085–1089.

[39]Johannesson, K.A., and Mitson, R.B. 1983. Fisheries **acoustics. A practical manual for aquatic biomass estimation**. FAO Fisheries Technical Paper 240.

[40] Valente, Michael; Holly Hosford-Dunn, Ross J. Roeser (2008). **Audiology. Thieme**. pp. 425–426. ISBN 9781588905208.]

[41]Urick, R.J., 1982, **Sound Propagation in the Sea**. Peninsula Publishing, Los Altos, California, 212 pp.

[42] J. H. Stockhausen, "**Scattering from the volume of an inhomogeneous half-space**," Naval Research Establishment, Canada, Rep. 63/9, 1963.

[43]. S. G. Schock, "**A method for estimating the physical and acoustic properties of the seabed using chirp sonar data**," IEEE J. Oceanic Eng., vol. 29, pp. 1200–1217, Oct. 2004.

[44] Schoenberger, M. **Apparent Attenuation due to Intrabed Multiples II Geophysics**, vol. 43, NO. 4 PP. 730-737, 1978

[45]. Lecture notes "introduction to shallow depth geophysics"